2020

Applications of Drones in Atmospheric Chemistry

Travis J. Schuyler
University of Kentucky, tjschuyler1@gmail.com
Author ORCID Identifier:
https://orcid.org/0000-0003-1599-8005
Digital Object Identifier: https://doi.org/10.13023/etd.2020.235

STUDENT AGREEMENT:

I represent that my thesis or dissertation and abstract are my original work. Proper attribution has been given to all outside sources. I understand that I am solely responsible for obtaining any needed copyright permissions. I have obtained needed written permission statement(s) from the owner(s) of each third-party copyrighted matter to be included in my work, allowing electronic distribution (if such use is not permitted by the fair use doctrine) which will be submitted to UKnowledge as Additional File.

I hereby grant to The University of Kentucky and its agents the irrevocable, non-exclusive, and royalty-free license to archive and make accessible my work in whole or in part in all forms of media, now or hereafter known. I agree that the document mentioned above may be made available immediately for worldwide access unless an embargo applies.

I retain all other ownership rights to the copyright of my work. I also retain the right to use in future works (such as articles or books) all or part of my work. I understand that I am free to register the copyright to my work.

REVIEW, APPROVAL AND ACCEPTANCE

The document mentioned above has been reviewed and accepted by the student's advisor, on behalf of the advisory committee, and by the Director of Graduate Studies (DGS), on behalf of the program; we verify that this is the final, approved version of the student's thesis including all changes required by the advisory committee. The undersigned agree to abide by the statements above.

Travis J. Schuyler, Student

Dr. Marcelo I. Guzman, Major Professor

Dr. Yinan Wei, Director of Graduate Studies

Applications of Drones in Atmospheric Chemistry

DISSERTATION

A dissertation submitted in partial fulfillment of the
requirements for the degree of Doctor of Philosophy in the
College of Arts and Sciences
at the University of Kentucky

By
Travis J. Schuyler
Lexington, Kentucky
Director: Dr. Marcelo I. Guzman, Associate Professor of Chemistry
Lexington, Kentucky
2020

https://orcid.org/0000-0003-1599-8005

ABSTRACT OF DISSERTATION

Applications of Drones in Atmospheric Chemistry

The emission of greenhouse gases (GHGs) has changed the composition of the atmosphere during the Anthropocene. A major technical and scientific challenge is quantifying the resulting fugitive trace gas fluxes under variable meteorological conditions. Accurately documenting the sources and magnitude of GHGs emission is an important undertaking for discriminating contributions of different processes to radiative forcing. Therefore, the adverse environmental and health effects of undetected gas leaks motivates new methods of detecting, characterizing, and quantifying plumes of fugitive trace gases. Currently, there is no mobile platform able to quantify trace gases at altitudes <100 m above ground level that can achieve spatiotemporal resolution on the order of meters and seconds. Unmanned aerial systems (UASs), or drones, can be deployed on-site in minutes and can support the payloads necessary to quantify trace gases. Thus, the research herein has contributed to the advancement of atmospheric, environmental, and analytical chemistry through the development, calibration, validation, and application of small unmanned aerial systems (sUAS). The quantification of atmospheric gases with sUAS is expanding the ability to safely perform environmental monitoring tasks and quickly evaluate the impact of technologies. The experimental findings have developed the sUAS as a platform for atmospheric measurements and demonstrated applications of meteorological and trace gas measurements. The research ultimately enabled novel studies that quantified and modeled the atmospheric transport of trace gases to better understand their impact on environmental and atmospheric chemistry.

KEYWORDS: atmospheric chemistry, analytical chemistry, unmanned aerial systems, trace gases, emission, sensors

Travis J. Schuyler

(Name of Student)

03/23/2020

Date

Applications of Drones in Atmospheric Chemistry

By
Travis J. Schuyler

Dr. Marcelo I. Guzman
Director of Dissertation

Dr. Yinan Wei
Director of Graduate Studies

03/23/2020
Date

ACKNOWLEDGMENTS

The following dissertation represents my passionate research dedication during the last four years, which highly benefited from the insights and direction of several people at the University of Kentucky. First, my Dissertation Chair, Dr. Marcelo I. Guzman, exemplifies the high-quality scholarship to which I aspire. In addition, Dr. Guzman provided timely and instructive guidance at every stage of the dissertation process, allowing me to complete this project on schedule. Next, I wish to thank the complete Dissertation Committee, and outside reader, respectively: Dr. Bert Lynn, Dr. Chris Richards, Dr. Sean Bailey, and Dr. Jason Unrine. Each individual provided insights that guided and challenged my thinking, substantially improving the finished product.

I would also like to thank the National Aeronautics and Space Administration (NASA), the NASA Kentucky Space Consortium, and the U.S. National Science Foundation (NSF). This research was supported by the NSF under RII Track-2 FEC award No: 1539070, the NASA Ky Space Grant Graduate Fellowship Award No: NNX15AR69H, and the NASA R3 EPSCoR award No: 80NSSC19M0032.

In addition to the assistance above, I received equally important assistance from family, friends, and colleagues in the unmanned aerial vehicle (UAV) lab. My fiancé, Morgan Wall, provided on-going support throughout the dissertation process, as well as editorial assistance critical for completing the project in a timely manner. Finally, I wish to thank Ryan Nolin and Zack Lippay, whose piloting and technical assistance facilitated safe and professional UAV flight operations.

TABLE OF CONTENTS

LIST OF TABLES

LIST OF FIGURES

CHAPTER 1. UNMANNED AERIAL SYSTEMS FOR MONITORING TRACE TROPOSPHERIC GASES

Reproduced with Permission from:

Travis J. Schuyler and Marcelo I. Guzman. Unmanned Aerial Systems for Monitoring Trace Tropospheric Gases

Atmosphere. **2017**, 8(10), 206.

DOI: 10.3390/atmos8100206

1.1 Background.

The atmosphere is a mixture of numerous gases dominated by volume ratios of 78.1% N_2(g), 20.9% O_2(g), and 0.934% of the noble gas argon.[1] The remaining 0.066% trace gases includes several greenhouse gases (GHGs) of natural and/or anthropogenic origin such as carbon dioxide (CO_2), methane (CH_4), ozone (O_3), nitrous oxide (N_2O), and chlorofluorocarbons (CFCs).[1] Trace gases play a major role in maintaining a stable climate on Earth by absorbing infrared radiation during their lifetimes on a direct proportion to their concentration.[1] These trace gases are emitted from a variety of anthropogenic sources including vehicles (.i.e. trucks, cars, airplanes, buses, etc.), industrial sources (i.e. biomass burning power production, water treatment, natural gas transport, etc.), and from modern farming techniques (i.e. fertilizing, prescribed burns, livestock, etc.). Further biogenic climate perturbations have been linked to volcanic eruptions quickly injecting large quantities of CO_2, sulfur dioxide (SO_2), hydrogen sulfide (H_2S), nitrogen oxide(s) (N_2O, NO and NO_2), etc. into the atmosphere.[2-4] In addition, trace gases can also introduce new

catalytic cycles that initiate atmospheric reactions that never occurred before.[5] The fugitive methane gas in the troposphere can react with hydroxyl radicals to form hydroperoxyl radicals. These hydroperoxyl radicals can react to oxidize nitric oxide to from nitrogen dioxide for further atmospheric aging affecting aerosol-cloud chemistry. Evidence of such undesired catalytic cycles has also been observed over Antarctica, where halogen radical species (e.g., Cl, Br, ClO_2, ClO, BrO) from anthropogenic sources have led to a hole in the ozone layer.[6, 7]

The fast rate of burning fossil fuels; changes in land use caused by deforestation, domestication of cattle, oil mining; and the emission of industrial pollution have impacted the chemical composition of the atmosphere[1, 2] raising numerous health concerns.[8, 9] The growing emission of GHGs has been associated to a disrupting effect on radiative balance with long term consequences.[1] Thus, instruments mounted on satellites,[10] which cannot provide altitude–resolved data, manned aircraft,[11, 12] atmospheric balloons[13] and tall towers[14] have been deployed to measure the changing concentrations of GHGs. However, as global emissions continue to rise, there is an increased need for technology that could allow accurate detection of trace gases near sources, and particularly in the lower troposphere. Remarkably, this atmospheric boundary region remains poorly characterized due to the lack of existing methods for monitoring trace gases. Therefore, UASs are an attractive alternative to traditional experimental techniques because they can collect air quality information in this underrepresented atmospheric region (0-100 meters above ground level). UASs can be deployed within minutes at the source, have excellent horizontal and vertical maneuverability, and can sample pre-determined locations without the intervention of a remote pilot to ensure systematic sampling. The implementation of

UASs as a platform to detect trace gases results in spatiotemporal data on the order of meters and seconds. Manned aircraft cannot achieve this level of resolution and entail more complex operations for deployment that are not as cost or time effective. Balloons can be deployed near the source but can be cumbersome and impractical when compared to the low-cost and ease of use that UASs offer.

Moreover, UASs can also be used to gather information about how the emission of industrial gases affects the particle size, composition, and concentration of aerosols in the lower troposphere. For example, UASs have been a useful platform for data collection of: 1) concentration and size gradients of aerosol particles in the boundary layer over a coastal area,[15] 2) the size and nature of atmospheric particles due to local pollution sources,[16, 17] and 3) the dispersion of aerosols and gases in a plume.[18] The remarkable power of UASs to enable characterizing the composition of the lower atmosphere is also accompanied by progress in methods that attempt weather modification. For instance, cloud-seeding technology that has been discussed for decades could now be advanced with promising experiments employing UAS technologies.[19]

UASs originated in the early 1900s, but their usefulness was not demonstrated until the Vietnam War in the 1960s and 1970s, during reconnaissance missions that were too dangerous for a piloted aircraft.[20] The diversification of UASs over the next few decades included capabilities for engaging in battlefield warfare and cameras able to achieve centimeter-scale resolution.[20] Soon the advantages of remote imaging UASs were noticed by the public and introduced to the civilian market.[20] Although a 98% of the production of UASs was for military use in 2004,[20] a significant increment for the production of civilian UASs has taken place recently to satisfy the demand from the general public. In fact, the

sale of civilian UASs, often referred to as “drones”, has increased by 224% from April 2015 to April 2016.[21] Drones have undeniably increased in popularity among the general public, and thus have become a focal point of research and development. Although the forefront of civilian uses resides in aerial photography, delivery of goods and entertainment, many environmental applications of UASs can be envisioned to help solve current limitations faced by atmospheric chemistry technology.[20, 22]

The early development of UASs has faced many challenges, including the need for legislation that has shown to be controversial in the United States.[23] The engineering problems that must be addressed include the flight range and endurance of the UASs. This is generally a consequence of aircraft size, energy storage, payload weight, and whether it is a fixed-wing or rotary-wing aircraft. UASs are currently limited by propulsion technologies,[24] but research using solar energy has shown promise to extend power storage for extended operation.[25] On the other hand, the scientific challenge for monitoring trace gases is the development of sensors that are lightweight, inexpensive, and accurate enough for daily data collection and analysis. In contrast, current detectors employed in manned aircrafts are general heavy, expensive and complex techniques such as mass spectrometry, which are neither size nor cost suitable to scale down for deployment with small UASs.[24-26] Indeed, state of the art detection methods must be developed based on the principle of keeping simplicity, low-costs, portability, and capacity for in-situ detection. This perspective presents the current knowledge for recent developments with UASs and sensors technologies and provides guidance to apply this information to boundary layer problems such as the detection of trace gases.

1.2 Classification of UASs.

It is convenient to introduce first the five broad categories of UASs resulting from their military origin the United Sates.[27] The transition of a UAS from one category to the next occurs if anyone of the limits to payload, altitude, or speed is surpassed. The first group has a maximum payload of less than 9.1 kg, an operating altitude of less than 366 m, and an airspeed of less than 185 km h^{-1}. The second group has a payload between 9.2 and 25 kg, an operating altitude of less than 1067 m, and an airspeed of less than 463 km h^{-1}. The remaining three categories have takeoff loads greater than 25 kg and a maximum of 599 kg. Their altitudes can reach up to 5.5 km (and above), with no limits to the airspeed. The applications that can be carried out with a UAS are linked to the category it belongs. Large UASs can perform advanced tasks, flying long distances and carrying heavy payloads. However, these large UASs (for payloads $\geq$ 25 kg) are not practical for atmospheric sampling at low altitudes. While the performance of small vehicles is relatively more limited than for large UASs, the great availability of these inexpensive models makes them especially attractive for research applications. The fact that UASs from the first two categories (with payloads $\leq$ 25 kg) are battery operated (and combustion free) makes them the preferred choice for trace gas detection.

Aside from the previous classification, there is a more recent and specific one that breaks down UASs into seven groups: 1) micro UAS (MUAS), 2) vertical take-off and landing (VTOL), 3) low-altitude short endurance (LASE), 4) LASE close, 5) low-altitude long endurance (LALE), 6) medium-altitude long endurance (MALE), and 7) high altitude long endurance (HALE).[25] The UASs classified as LASE close, LALE, MALE, and HALE (groups 4 through 7) can reach altitudes up to 1.5 km and all require substantial runways for take-off and landing. Because there are no battery-operated UASs capable of such

tasks, these classes of UASs appear to be of low relevance for trace gas detection.[25] The first three categories (MUAS, VTOL, and LASE) are all viable options for trace gas monitoring. MUAS are defined by their miniature size (~15-20 cm) and ultra-light weight, with payloads of less than 50 g and flight times of 8-10 min.[25]

In addition, UASs are also divided into fixed-wing and rotary-wing aircrafts, which respectively look like traditional airplanes and helicopters. Although fixed-wing aircrafts do not have the maneuverability and take off/landing convenience of rotary aircraft, they are more stable in severe weather conditions and tend to have more space for payload configurations.[24, 26] Both fixed-wing and rotary-wing UASs can be used for trace gas monitoring if they are not propelled by internal combustion engines. Examples of fixed-wing UASs included in Figure 1.1 are the Bormatec Maja and Explorer, the CyberEye II, and the Skywalker X8.

Figure 1.1 Examples of fixed-wing UAS platforms for trace gas monitoring.

Both Bormatec UASs (Maja and Explorer) are closely related but differ by having single and dual engine setups, respectively. The CyberEye II represents the style of a conventional fixed-wing UAS that can be adapted for low-cost trace gas detection. The Skywalker X8 is a practical alternative that provides useful payload capacity for small,

light-weight trace gas sensors at a fraction of the cost of the other three UASs in Figure 1.1.

From the large variety of rotary-wing UASs available in the market, a few examples included in Figure 1.2 are the T-REX 700E helicopter, the DJI Matrice 600, the AirRobot AR100B, and the AscTec Falcon 8. The T-REX 700E represents the traditional helicopter with one central rotor, and a secondary rotor on the tail of the aircraft. The DJI Matrice 600 is a lightweight hexacopter, with its rotors distributed in a circular pattern. The AirRobot AR100B is a quadcopter, also with its rotors in a circular array. The AscTec Falcon 8 is an octocopter with an alternative linear array of rotors. Because the upward force of the UAS is proportional to the diameter and number of rotors, the primary reason for adding extra rotors to the aircraft is to provide a greater lift. [26]

Figure 1.2 Examples of rotary-wing UAS platforms for trace gas monitoring.

However, it must be noted that adding rotors increases battery consumption and results in shorter flight times. Thus, a primary consideration for maximizing flight duration for a given payload is to optimize the number of rotors needed.

VTOLs are typically rotary-wing UASs that have the obvious advantage of near-instant deployment. Thus, VTOLs are versatile for field operations where runways are not an option. Given that the flight time for this class is limited from 20 to 60 min, a VTOL is an ideal platform to deploy sensors as close to the source as possible.[25] The maneuverability of VTOLs is also one of its strengths; the ability to hover in one location and reverse is advantageous. However, there are numerous types of VTOLs (e.g. helicopter, quadcopter, hexacopter, octocopter), each of which creates a unique downwash that can make gas detection and quantification complex.[25]

LASEs are the most diverse class of UASs and are characterized by simplicity and ease of use. The wingspans are limited to 3 m and offer payloads from 2-5 kg. These UASs can be hand-launched or catapult-launched, and offer flight times from 45 to 120 min. This class of UASs can also be fit with autopilot features that offer the advantage of pre-planned flight patterns to ensure systematic sampling.

In summary, selecting the most appropriate UAS for sampling in the lower atmosphere requires consideration of the mission objectives, environmental conditions, and budget. The frame of the selected UAS model requires alteration for carrying the trace gas detection system to be deployed. Different sensor technologies for trace gas detection are discussed below.

1.3 Sensors for Trace Gases.

There are many different types of sensors that can be mounted into a UAS for detecting trace gases in the lower atmosphere. The most common methods are electrochemical, photoionization, infrared (IR) laser-absorption, semiconductor, and catalytic detection. Although each method is fundamentally different, all sensor types must

be able to detect background atmospheric concentration levels and have a dynamic range that spans the range of gas concentrations expected to experience in field. The U.S. Environmental Protection Agency (EPA) has made available the useful detection limits and expect mixing ratio ranges for several trace atmospheric gases of interest, information that is presented in Table 1.1.[28]

Table 1.1 Detection Limits and Expected Mixing Ratios (in parts per billion, ppb) of Selected Trace Atmospheric Gases.

Air Pollutant of Interest	Useful Detection Limit	Range to Expect
Ozone	10 ppb	0-150 ppb
Carbon monoxide	100 ppb	0-300 ppb
Carbon dioxide	100 ppm	350-600 ppm
Nitrogen dioxide	10 ppb	0-50 ppb
Sulfur dioxide	10 ppb	0-100 ppb
Methane	500 ppb	1500-2000 ppb

A bias and precision of ±30% is reasonable for hotspot identification and characterization purposes; for supplementary network monitoring, a bias and precision of <20% is necessary for further investigation.[28] Another aspect to consider with trace gas sensors is the response to rotor turbulence. The impact of rotor turbulence with respect to detecting trace gas concentrations with sensors on board UASs is relatively unexplored. A handful of publications present some computational fluid dynamic (CFD) analysis in a general context of mapping quadrotor downwash,[29-31] but there are limited publications including a CFD analysis for sensor placement.[32] Furthermore, the computational resources are not currently available to run detailed simulations that include the effect on local gas concentrations, thus the analysis of how gas concentrations are affected by UAS rotor turbulence is still something that needs to be studied. Even though the scope of these simulations are limited, they all show general consensus on the location of the maximum

and minimum airflows around the aircraft so some useful conclusions can be drawn from them. There are a few options when considering sensor placement. The first is to place the sensors outside the range of the rotor turbulence entirely, but at the cost of adding significant complexity, weight, and affecting the center of gravity. The second option is to minimize the airflow around the sensor on the UAS. The center of the fuselage above and below the aircraft appears to be the optimal placement to minimize air disturbances around the sensor, and thus are ideal locations for sensor placement. If the sensors are not used to gather luminosity measurements and/or are highly sensitive to UV light/temperature, locating them under the fuselage of the aircraft appears to be an ideal solution. A third possible solution is to isolate the sensor from rotor downwash entirely and pump the air in with a sample inlet clear of the turbulence. The solution to be employed depends on the payload capacity of the UAS and the dependence of the instrument on air turbulence.

Electrochemical type sensors are commonly used for the detection of toxic gases as they pass through a semi-permeable membrane and undergo a redox reaction at the working electrode.[33] The resulting electrical current between the working and reference electrodes can be calibrated to provide the concentration of the desired gas. A typical problem associated to the use of electrochemical sensors is its cross sensitivity to other gases if the choice of membrane has not been carefully considered. Although, new and promising calibration methods are currently being developed to correct for sensor dependences on variable environmental conditions (i.e. temperature and relative humidity).[34] Photoionization detectors commonly incorporate a durable 10.6 eV UV lamp to ionize volatile organic compounds (VOCs).[35] The ejected electrons resulting from the photoionization of VOCs produce an electrical current that is directly proportional to

concentration of the volatile species. While the sensitivity of this technique extents to low ppbv mixing ratios, the signal corresponds to the sum of all gases with an ionization potential that lies below the threshold set by the lamp's photon energy.

The principle of operation for IR laser-absorption sensors is not different from a bench-top spectrometer.[36, 37] As the laser beam passes through the atmosphere, a detector measures the loss in radiation intensity as a function of wavenumber. The loss of radiation intensity relative to the reference beam (or the same beam at a different wavelength) can provide the concentration of gases, while the wavelength of light absorbed provides the identity of the gas. The advantage of this technique is to sample large volumes for analysis because the sensor does not need to come in contact with the gas.

Semiconductor type sensors commonly use a tin or tungsten oxide film, which is saturated with adsorbed oxygen species (O_2^-, O^-, O^{2-}) in clean air.[38] The presence of oxygen on the film creates a high potential between the sensor and air. However, the presence of reducing gases results in the desorption of $O_2(g)$, which lowers the potential and allows current to flow through the sensor. This change in resistivity within the sensor is the principle that can be used to measure the concentration of a gas. Lastly, catalytic sensors operate using two parts known as beads, which are connected in a Wheatstone bridge circuit.[39] One bead has a catalytic material that is reactive to combustible gases and the other bead is not reactive because it is made of an inert material. The heat produced as combustible gases react with the catalyst causes an increase in resistivity of the catalytic bead. The circuit is designed to produce a voltage output (from the relative change in resistivity), which can be measured and is proportional to the concentration of the gas of interest.

1.4 Implementation of Sensor Technology Onboard UASs.

Several different categories and models of UASs have been introduced above and the significant factors for selecting between them are size, range, payload, and whether it is a fixed-wing or rotary-wing vehicle. These UASs can be modified to include sensors for monitoring trace tropospheric gases at low altitudes, as demonstrated in recent experimental efforts that have successfully employed three different sensor technologies: 1) a portable IR laser-absorption spectrometer, 2) two semiconductor sensors, and 3) a catalytic type sensor.

The first technology implemented has used a robust optical setup for IR laser absorption spectrometry to quantify GHGs using a photodetector.[40, 41] This optical application includes the low-power vertical cavity surface emitting laser (VCSEL) displayed in Figure 1.3, which probes the near-infrared region to identify GHGs such as CO_2 and CH_4.[40, 41] However, this method suffers interference from absorption by water vapor (H_2O). Thus, wavelength modulation spectroscopy has been employed to further resolve the overlapping signals from different gases.[40] In addition, a cylindrical multi-pass cell with gold-coated mirrors has been used for increasing the optical path of the laser beam reaching the photodetector. This optical setup has been mounted into the T-REX 700E helicopter (Figure 1.2) for low altitude flights with a total payload < 0.5 kg that lasted 5 to 10 min for measuring CO_2 and CH_4 at 4,994.94 cm^{-1} and 4,996.12 cm^{-1}, respectively.[40]

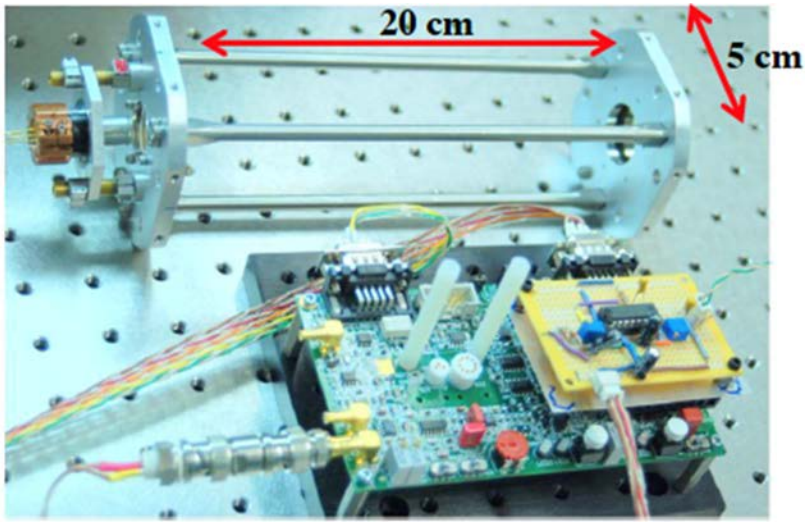

Figure 1.3 Low-power vertical cavity surface emitting laser with multi-pass cell and photodetector. Reproduced with permission from Khan, A. et al., Remote Sensing; published by MDPI, 2012 [40].

Measurements of CO_2 and CH_4 have been performed with the VSCEL technique using wavelength modulation onboard a T-REX 700E helicopter (a VTOL UAS) at an air speed of 15 m sec^{-1} that provides higher spatial resolution than possible by a conventional aircraft.[40] This temporal and spatial resolution data for CO_2 and CH_4 obtained at 2000-2003 and 1654 nm, respectively, is displayed in Figure 1.4.[40] The mixing ratio of CO_2 at very low altitude (< 5 m) has varied between 350 and 450 ppmv. For CH_4, mixing ratio measurements in the range 1700-1900 ppbv have been detected in the range 10-40 m altitude. Importantly, knowing the humidity during these measurements enabled the correction of field measurements after laboratory calibration that also included instrument stability and drift. The laboratory precision of the VSCEL sensor has been demonstrated to be ±0.06 ppmv for CO_2 and ±0.9 ppbv for CH_4. In the field, the precision of measurements is within ±0.1 ppmv and ±2 ppbv for CO_2 and CH_4, respectively. Because many gases absorb in the infrared range, the application of this technique to quantify other trace gases could be expanded.

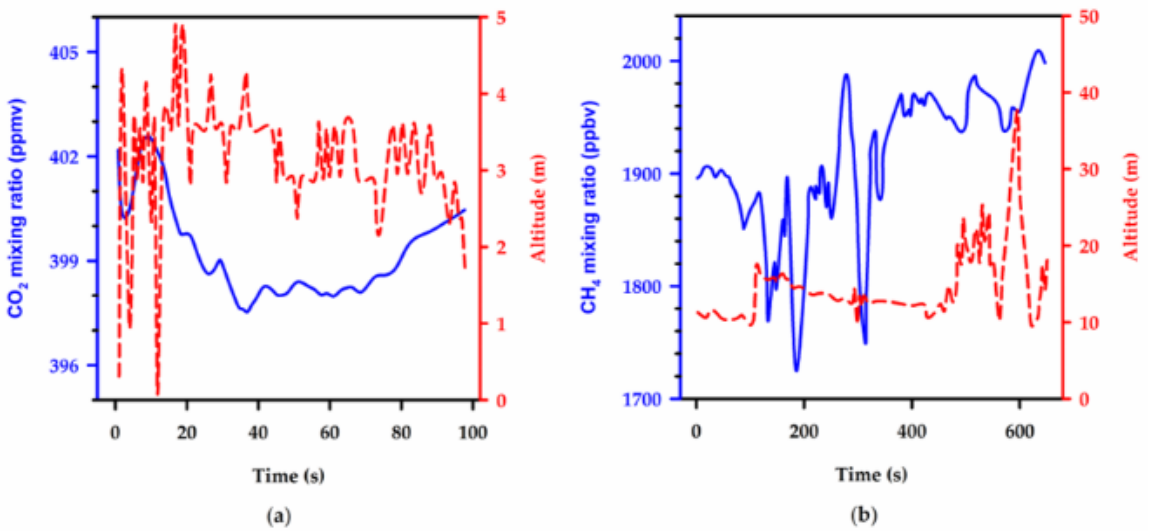

Figure 1.4 Time series for the mixing ratios of (a) CO_2 and (b) CH_4 vs. flying altitude obtained by laser-absorption spectroscopy.[40]

The second technology that has been tested employs semiconductor sensors to quantify the presence of GHGs and VOCs from changes in resistivity.[26] This technology has been demonstrated in a micro electro-mechanical system (MEMS) with metal oxide (MOX) gas sensors customized with micromachining techniques for UASs. The advantages of using MEMS with MOX, e.g., made of tungsten trioxide (WO_3) such as that displayed in Figure 1.5, comprise a reduction in the payload and power intake of the sensor, making it practical for mobile VOC detection. These sensor arrays can potentially allow simultaneous monitoring of several different compounds, including CO_2, NO_2, and SO_2.[26] For practical applications the sensor has been integrated into a microcontroller and mounted into a UAS[26] such as the DJI hexacopter in Figure 1.2 for carrying a payload of 0.3 kg during 15-min flights when powered by two parallel 9 V batteries.[26]

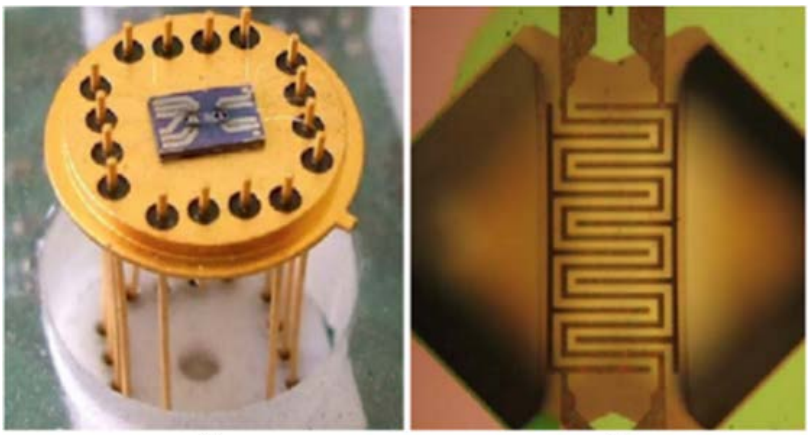

Figure 1.5 (a) Micro electro-mechanical system bonded to a WO_3 metal oxide sensor. (b) Detailed image of the nanoporous WO_3 layer. Reproduced with permission from Rossi, M. et al., IEEE Sensors 2014 Proceedings; published by IEEE, 2014.[26]

Among the trace gases that could be detected by the MEMS MOX sensors, a VTOL UAS has facilitated monitoring the release of the VOC isopropyl alcohol over an open field.[26] Preliminary results show VOCs have an impact in sensor response, and that GHGs can be detected in the turbulent flow of a VTOL UAS.[26] However, the registered change in the output of the sensor corresponds to an absolute response to all VOC present, and no selectivity for different gases has been demonstrated.[26] Indeed, the results suggest that further development and laboratory calibration would be needed to identify and quantify trace gases in the atmosphere with this type of sensors.

In addition, the highly selective MQ-4 semiconductor sensor for CH_4 detection (Figure 1.6)[42] is a good candidate for deployment with UASs. Although the MQ-4 sensor has been designed to monitor CH_4, a lower selectivity for detecting the gases propane and butane is possible.[42]

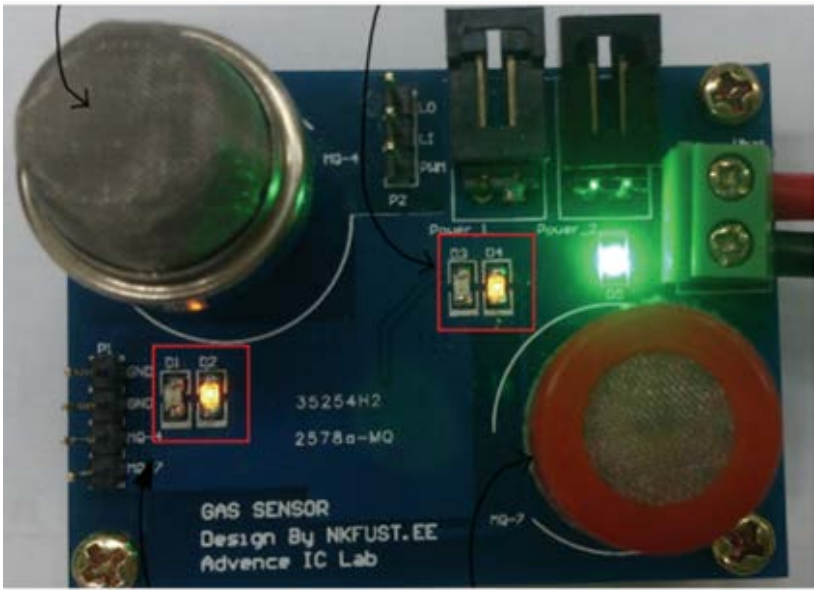

Figure 1.6 MQ-4 sensor (top left) with serial ports attached to a microcontroller. Reproduced with permission from Chen, M. et al., International Journal of Distributed Sensor Networks; published by SAGE, 2015.[42]

The cheap and commercially available MQ-4 sensor can be easily paired to a microcontroller mounted to either a fixed-wing or rotary-wing UAS. However, a challenge faced by this current technology is the need to perform accurate calibrations under variable temperature and relative humidity. MUASs devices appear to be an ideal platform for deploying the small and lightweight MQ-4 sensor. Employing multiple MUASs in a swarm can potentially provide real-time tridimensional (3D) spatial resolution of CH_4 concentrations in a cost-effective manner. This technique could be also be applied in a discrete manner in urban settings, but with limitations such as for short flight times or the inability to fly in strong winds.[25] In addition to CH_4, the MQ-4 sensor can also detect liquid propane gas (LPG), hydrogen gas (H_2), carbon monoxide (CO), ethanol, smoke, and air.

For calibration purposes, the measured resistivity of the MQ-4 sensor (R_s) is expressed relative to the reference signal for 1000 ppmv CH_4 in air (R_o).[43] Such information for the MQ-4 sensor is available, e.g., at 20 °C, for 65% relative humidity,

21% O_2 mixing ratio, and a load resistance of 2 × 104 Ω[43] and varies with humidity and temperature. Therefore, in order to obtain useful CH_4 mixing ratios with this sensor, calibrations across several temperature and humidity conditions are needed.[43] A general concern for employing this sensor in the presence of multiple gases is the lack of specificity to differentiate and quantify several gases simultaneously. However, the MQ-4 sensor can still provide useful information because of its much sharper response for CH_4 than for other gases that are certainly not in excess.

Interestingly, trace gas emissions of CH_4 from a landfill have been successfully studied following a racetrack pattern, which can be accomplished by flying the Skywalker X8 in Figure 1.1, a LASE UAS, perpendicular to the direction of the wind.[44] Thus, the quantification of CH_4 using this UAS should be attempted in the future with a Skywalker X8 equipped with both the MQ-4 sensor for CH_4 and the MEMS MOX sensor for the detection of other GHGs and VOCs. However, the Skywalker X8 is not robust enough for most laser absorption spectroscopy techniques, such as the VCSEL.

This section lastly covers a catalytic type sensor that has already been proved in commercially handheld gas detectors. Catalytic type gas sensors have long been available on gas monitoring devices developed for industry settings, where a small gas leak can be dangerous or even deadly. Existing devices have evolved to measure up to six gases simultaneously, but they need to be modified to fit the needs for onboard sensing with UASs. An example of such adaptation has been attempted with an AirRobot AR100B (Figure 1.2) capable of flying for 30 min with a payload of 0.2 kg to measure mixing ratios of CO_2 and SO_2 over a volcanic crater in the Canary Islands.[45] The method was laboratory validated only for CO_2 using a test chamber filled with clean air.[45] Importantly, the device

provides the option to exchange the catalytic sensors for toxic gases by electrochemical type sensors or even photoionization detectors (PIDs) for combustible gases.

There are further examples of sensors used for trace gas deployment that do not explicitly stick to one type of detection mechanism, several examples of UAS deployments for atmospheric monitoring can be found herein.[46-54]

1.5 Interface for Integration of Analytical Sensors into UASs and Initial Cost Considerations.

The miniaturization of sensor packages is enabled by printed circuit boards (PCBs). Software such as Fritzing allow for the design and printing of unique circuit boards that can integrate several gas sensors into a small, lightweight package.[55] These PCBs are generally battery powered, although the development of radio frequency identification (RFID) tags provides a promising future for wireless powering of these low-power consuming devices. These PCBs are programmed with microcontrollers or microcomputers on single integrated circuits. Typical microcomputers employed combine a processing core, RAM, and an operating system (e.g., Linux) to operate microcontrollers. Programing of the microcomputer is enabled with software using a keyboard and monitor connected to the device. Among the options for collecting data from the sensor package, there are two common reliable practices, 1) to store data on a SD card for later retrieval and analysis, and 2) to wirelessly transmit data in real time to an online database or back to the users' computer via Wi-Fi or Bluetooth.

The costs of UASs such as MAV, LASE, and VTOL can vary widely based on the airframe, the GPS navigation system to be added, the autopilot and telemetry system, and motor/battery combination chosen. Airframe costs can range from $250 to $5000

depending on the type and complexity of the aircraft. Although the GPS navigation system can be costly (e.g., ~ $4000) it is a significant component to determine the quality of flight. The autopilot systems can vary significantly due to the quality of the flight control with prices starting at $50 that for higher-end systems increases to $300. Batteries for UASs range from $65 to $200, but the number of batteries required for operation could range from 1 to 6 depending on the number of rotors. Additionally, spare batteries are required to keep the UAS in flight as much as possible, what impacts the total battery cost to range between $65 and $1200. In addition, battery chargers cost $60-200. For those airframes that do not come equipped with a motor, an additional investment of $30-120, depending on size and rating, is needed. Many users of UASs also find useful to have onboard digital-to-analog (DAC) converters that cost between $200 and $300. Thus, just for the total cost of a UAS a figure of $5000 to $12000 can be obtained.

The cost of sensor packages can also vary slightly based on the type of microcontroller/microcomputer used, the number and type of analytical sensors deployed, and how the device is powered. The microcontrollers/microcomputers cost $25-40 but may require multiple shields (or a PCB) to incorporate data transmission, as well as a memory card, which could cost an additional $35. Batteries are approximately $20 each, and at least 2 batteries are required per unit to run continuously all day. The price of analytical gas sensors certainly depends on the detection method chosen. Many electrochemical, photoionization, catalytic, and semiconductor type sensors are readily commercially available, but the price reflects the quality of the sensor. Many gas sensors are available for $5-10, however for the highest-quality gas sensors the price range can jump to $300-1000. There is a large variety of gas sensors priced in-between as well, but again the price

reflects the quality. It is recommended to verify the following information is available when purchasing sensors: calibration, lifetime, sensitivity, response time, and size/weight. Lastly, there are no commercially available IR laser-absorption instruments. This means that the instruments reviewed above were custom built for that UAS, making cost estimates difficult. However, given the costs of lasers, optical cables, gas chambers, and detectors, it is the most expensive method to deploy.

1.6 Restrictions and Regulations in the United States and European Countries.

According to the U.S. Federal Aviation Administration (FAA), any model aircraft under 55 lbs (25 kg) is considered a small unmanned aerial vehicle (sUAS) under the addition of Part 107 to Title 14 Code of Federal Regulations. Part 107 states that the pilot in command (PIC) must have a proper certification requirement if a sUAS is operated for non-hobby purposes. The FAA defines such operations as: agricultural monitoring/inspection, research and development, educational/academic uses, powerline/pipeline inspection in mountainous terrain, antenna inspections, bridge inspections, aiding search and rescue, wildlife nesting area and evaluations, and aerial photography [56]. Flying a sUAS for any of these objectives requires that the pilot obtains a "Remote Pilot of Small Unmanned Aircraft System" license, and that the unmanned aircraft be registered with the FAA. The license examination can be taken at any of the local certified testing stations listed on the FAA website[57] and the aircraft can be registered at the FAA website.[58] Upon obtaining the part 107 license, the individual may now legally conduct research operations. However, there are some considerations one must take to ensure that the provisions of part 107 are followed. When flying, there must always be at least one PIC per aircraft. This person may not be the individual at the controls of the

aircraft, but they are in charge and responsible for that operation. The PIC must maintain line of sight of their aircraft, unless a visual observer (VO) is used. The sole job of the VO is to watch the sUAS and report any potential dangers back to the PIC. The PIC, VO, and individual at the controls must be able to remain within eyesight and be able to communicate at all times. First person view (FPV) style optics do not meet the line of sight requirements but may be used in addition. Operations are to begin and end at civil twilights (30 min before sunrise and 30 min after sunset) and shall not exceed 121.9 m above ground level or 160.9 km h^{-1} groundspeed. Lastly, it is particularly important to ensure that external load operations are attached firmly and will not adversely affect the center of gravity or flight time in such a way that will jeopardize flight operations. It is possible to conduct operations outside of normal FAA guidelines through a Certificate of Waiver or Authorization (COA). For example, a COA would be necessary to fly in the dark before sunrise to obtain a baseline before atmospheric boundary layer inversion, or to fly above 121.9 m for vertical profiles. A COA is obtained by application to the FAA. The applicant must demonstrate that the operation can safely be conducted under the terms of the COA and will be allowed to operate outside normal FAA guidelines.

The European Aviation Safety Agency (EASA) is in the process of creating their own unified standard for UASs. As of April 5, 2017, the first official draft pertaining to UASs regulation has been published.[59] By the end of 2017 the proposal will be brought to the commission, it will be finalized by mid-2018, and implemented in 2019. The EASA categorizes operations based on the particular risk associated, and the type/size/performance of unmanned aircraft used. The regulations are dependent on both the class of the operation and the UAS.

There are three classes of operations defined by the EASA: open, specific, and certified. Open operations are defined as not needing prior approval of competent authority and have little to no risk. Open operation regulations are aimed towards the general public and apply to all member states of the European Union (EU). Regulations of open operations will not be explained in detail, but it is advised to become familiar with the different subclasses of open operations (flying over people, flying near people, and flying far from people) and classes of UASs (C0, C1, C2, C3, C4, and privately built).[59]

Specific operations, due to the risk involved, must obtain flight authorization from competent authorities. The EASA will issue standard scenarios for specific operations that the member states of the EU can choose to adopt or change. Either way, member states shall designate a governing body for specific operations (similar to the way the United States of America designates the FAA). Permission for specific operations can be granted from the competent authorities by submitting a risk-assessment analysis before each flight. However, the operator can authorize their own operations if they possess a Light UAS Operator Certificate (LUC). As mentioned above, regulations can vary between member states, so it is advised to go to your EU member state (if applicable) and enquire about their regulations for specific operations with the goal of obtaining a LUC to authorize your own operations, Table 1.2 summarizes the EU member state regulations for unmanned operations.[60]

Table 1.2 Summary of UASs Regulations for European Union (EU) Members

Member State of EU	Max Takeoff Mass Limit	Categories	License	Height Limit
AT	150 kg	5 kg; 25 kg	More risky categories with an increase of pilot qualification	150 m AGL

Table 1.2 (continued)

BE	150 kg	<1 kg recreational; <5 kg class 2; >5 kg class 1	Yes for Class 1 (including LAPL medical); Class 2: practical examination with certificate (no medical)	300 ft AGL
CH	150 kg	Open: <30 kg, 100m outside crowds VLOS; Specific: else	Pilot skills in the total hazard and risk assessment (GALLO)	No limit (with GALLO)
CZ	150 kg	0.91 kg; 7 kg; 20 kg	RPA for professional use needs authorization. Pilot passes practical and theoretical tests	300 m AGL; in CTR 100 m AGL
DK	>25 kg need authorization	1A: < 1.5 kg 1B: < 7 kg 2: 7-25 kg 3: BVLO	For commercial use in populated areas, permission is needed. Applicants need have an operations handbook and pass a practical test	100 m
FI	25 kg	7 kg over densely populated areas	No	150 m
FR	150 kg	Captive RPAS and RPAS < 2 kg, < 25 kg; and > 25 kg	RPAS > 25 kg need a remote-pilot license. For scenario S1, S2, and S3: theoretical certificate, and practical test. For scenario S4: theoretical certificate + manned aviation license.	150 m; (50 m in scenarios S2, RPAS >2 kg)
DE	25 kg	<25 kg; >25 kg	Theoretical and practical requirements above 5 kg.	100 m
IE	150 kg	1, 5, 7, and 20 kg	No, but theoretical and practical requirements	120 m for <20 kg
IT	As per basic regulation	0.3 kg; 2 kg; 25 kg	Yes, pilot certificate for VLOS and < 25 kg, otherwise license. Medical class LAPL/3.	150 m

Table 1.2 (continued)

LT	>25 kg need registration	1. <300 g; 2. >300-25 kg; 3. >25 kg	Yes, requirements set up in conditions for conducting commercial flights	400 ft
MT	150 kg	No	Medical Declaration	400 ft
NL	150 kg	No	Yes	120 m
PL	150 kg	25 kg	Certificate of qualification, including medical for commercial pilots	
PT	>25 kg need authorization ; toy <1 kg	Toy < 1 kg ; >25 kg with authorization	Case by case, >25 kg	120 m; toy 30 m outside controlled airspace
SI	150 kg	No	Yes	
ES	150 kg	<2 kg ; <25 kg; and >25 kg	< 25 kg theoretical knowledge + practical course on RPAS + LAPL; > 25 kg pilot license	120 m
SE	150 kg	1A: 0-1.5 kg / max 150 J / VLOS 1B: 1.5-7 kg / max 1000 J /VLOS 2: 7-150 kg /VLOS 3: BVLOS	Yes >7 kg	120 m
UK	150 kg	<20 kg; >20-150 kg	> 20 kg or BVLOS; < 20 kg VLOS: pilot competency assessment required if requesting permission.	400 ft (>7-20 kg); <7 kg VLOS

Lastly, certified operations are considered high risk and include large or complex UAS operating continuously over open assemblies of people or operating beyond visual line of sight in high density airspace. Certified operations also include UAS used to transport of dangerous good or people. These operations are more closely governed by the laws of manned aircraft and require the certification of the operator and the aircraft, as well as the licensing of the flight crew. Certified operations are outside the scope of this perspective and will not be discussed further.

There are too many countries to discuss the all the developing legislation in depth (i.e. China, Australia, Canada, etc.). If the information provided does not suffice, there are resources developed by the International Civil Aviation Organization (ICAO) that provides links to aviation authorities worldwide. Specifics on unmanned aircraft regulations can be found therein.[61, 62]

1.7 Summary of UASs for Air Sampling.

Monitoring trace tropospheric gases with UASs is a promising methodology for atmospheric chemistry applications. MAVEs, VTOL, and LASE aircrafts are the most practical UASs for trace gas monitoring. Specifically, those UASs with wingspans under 3 m for payloads < 5 kg are the best compromise between cost and convenience for deploying sensors. These UASs offer altitude capabilities of a few hundred meters with flight times ranging from 30 min to 2 h. Examples of how these UASs can carry lightweight, low-power, cheap trace gas sensors have been provided. However, further progress is needed to achieve the accurate quantification of a mixture of gases under variable environmental conditions. The most expensive part of integrating analytical sensors into UASs is also the most difficult to quantify, because time and investment for

research and development of these new analytical methods of gas detection are needed. Numerous hours, days, and months of innovation in the laboratory and application in the flying field will need to be invested, which is costly and nearly impossible to put a dollar amount for comparison to the cost of the individual components. Future progress in this area is possible through the integration, calibration, and validation of new instrumentation onboard UASs in environmentally relevant conditions.

1.8 Applications of UASs as Analytical Devices for Atmospheric Sampling.

The research herein aims to advance atmospheric science through the development, calibration, validation, and application of small unmanned aerial systems (sUAS). Establishing the sUAS as a legitimate scientific tool for atmospheric measurements was the first research objective. This process included the software and hardware development to record and log the sensor data, the CAD design and 3D printing of the parts to integrate the sensors into the UAV, and the calibration and validation of the sensors on-board the UAV in environmentally relevant conditions.

The second chapter describes initial sUAS development through the results of the 2017 CLOUDMAP campaign, where the first-generation sensor package was developed and successfully used to measure environmentally relevant mixing ratios of methane, carbon dioxide, and ammonia.

The second objective was to further the research by deploying the sUAS to quantify fugitive gases. The third chapter describes a continuation of the sUAS development, with key upgrades that enabled enhanced gas sensing capabilities and autonomous sampling. The sUAS was deployed to quantify fugitive ammonia in flue gas from the oxidative

degradation of monoethanolamine in a carbon capture system. The research uses a Gaussian plume model to estimate the concentration of ammonia before diffusion.

The final research objective was to use the calibrated and validated sUAS for measurements and dispersion modeling of fugitive trace gas fluxes. The fourth chapter expands on the previous chapters through coincident measurements of turbulent statistics and trace gases to determine fugitive gas fluxes. The result study aims validates the sensor package developed herein and enable future leak rate estimates of fugitive gases. Finally, Appendix 1 describes a methodology to collect used to collect biomass burning particulates during a controlled burn with sUAS for offline analysis.

Overall, the objectives of the research strive to enable analytical studies that quantify the emission and atmospheric transport of trace gases to better understand their impact on environmental and atmospheric chemistry.

CHAPTER 2. MONITORING TROPOSPHERIC GASES WITH SMALL UNMANNED AERIAL SYSTEMS (SUAS) DURING THE SECOND CLOUDMAP FLIGHT CAMPAIGN

Reproduced with Permission from:

Travis J. Schuyler, Sean C.C. Bailey, and Marcelo I. Guzman. Monitoring Trace Tropospheric Gases with Small Unmanned Aerial Systems (sUAS) during the Second CLOUDMAP Flight Campaign

Atmosphere. **2019**, 10(8), 434

DOI: 10.3390/atmos10080434

2.1 Introduction

A major problem in atmospheric chemistry research is accurately quantifying dynamic emissions in the proximity of pollution sources under wind turbulence.[63, 64] The large bandwidth of turbulent flow experienced at the surface of the Earth is a significant contributing factor that makes it difficult to take precise measurements with existing techniques.[65] In consequence, the current techniques for atmospheric sampling in the lowest few hundred meters of the atmospheric boundary layer (ABL) are associated to large uncertainties. The fugitive greenhouse gases (GHGs), i.e., CH_4, CO_2, N_2O, and hydrofluorocarbons (HFCs) from transportation, industry, and livestock are known to increase global radiative forcing and are a significant source of climate change.[66-69] Other pollutants such as CO, NH_3, SO_2, NO_x, and volatile organic compounds (VOCs) are a health risk in urban environments and a cause of respiratory diseases.[70-72] Reports from independently measured experimental values indicate that GHG emissions are

significantly higher than modeled from the same source, suggesting that emission estimates of GHG are incomplete and models are associated with large uncertainties.[73-75] Reducing the uncertainty of low-altitude (<100 m) trace gas emissions is critical to fully understanding emission processes and implementing sustainable industrial practices. The traditional use of manned aircraft, weather balloons, towers, or satellites does not provide the cost feasibility, ease-of-use, or spatiotemporal resolution (on the order of meters and seconds) necessary to sufficiently sample pollution at the source in a way that will constrain measurement uncertainties in a practical manner.[76]

The fast adoption of unmanned aerial vehicles (UAV) for aerial photography, video, and delivering goods has opened the door for new opportunities in atmospheric research. Indeed, the large power demand and heavy weight of established benchtop analytical instrumentation prevent their use for sampling with UAVs. Thus, the challenge for creating sampling platforms employing drones to detect trace gas emissions consists of developing analytical systems within the lightweight payload constraints.[76] For accomplishing the previous objective, the integration of sensor packages into commercially available small UAVs, creating small unmanned aerial systems (sUAS), has been proposed as a promising quantification method.[76] Gas sensing packages are advantageous due to their lightweight, low power consumption, and robust analytical behavior. However, the sensor output must have limited dependences on variable environmental conditions, possess a high selectivity for target analyte, and have a sufficiently fast response time to be adequate for field work.[76]

This work demonstrates the proof-of-concept of small unmanned aerial systems (sUAS) that are deployed to quantify trace gases in the lowest, most dynamic region of the atmosphere, contributing a tool to constrain existing mixing ratio uncertainties near

potential sources. In this research, two different sUAS capable of detecting the trace gases ammonia (NH_3), methane (CH_4), and carbon dioxide (CO_2) are introduced. The first sUAS is a DJI Phantom 3 (DJI P3) quadcopter used to fly vertical profiles, and the second sUAS is a fixed-wing Skywalker X8 used to fly horizontal profiles. The two sUAS are flown simultaneously to provide datasets with the mixing ratios needed to create a box model of trace gases within the flight area. These trace gas measurements are associated to measurements of temperature, relative humidity, pressure, and position (latitude, longitude, and altitude), which enables the evaluation of sensor performance under variable environmental conditions. The datasets presented summarize the results from 32 flights with each sUAS, which were collected between 26 and 29 June throughout the 2017 Collaboration Leading Operational Unmanned Aerial System Development for Meteorology and Atmospheric Physics (CLOUDMAP) [77] field campaign in Oklahoma.

2.2 Experimental Methods

2.2.1 Description of Campaign Site

All research flights were performed in accordance with the current regulations (Part 107) established by the United States of America Federal Aviation Authority (FAA) during 26–29 June 2017. The flights took place at the Unmanned Aircraft Flight Station of Oklahoma State University (317 m above sea-level), which is located ~20 km to the east of Stillwater in the state of Oklahoma (36°09′43″ N, −96°50′07″ W). Figure 2.1a shows a regional map covering the Oklahoma area, which includes a blue pin indicating the geographical location of the Unmanned Aircraft Flight Station used.[78] The site is 23.72 km from Station 89 (STIL) of the Mesonet network,[79] which is used for ground-based measurements and sensor validation. The average wind speed at 2 m above ground level

(AGL) registered on 27 June was 2.75 (±1.37) m s^{-1}, with the wind direction of 7° N.[79] On 28 June, the average wind speed at 2 m AGL was 4.04 (± 1.09) m s^{-1}, blowing 8° N.[79] Figure 2.1b shows the distance covered during the flights with the Skywalker X8 aircraft[78] and the actual flight path flown by this aircraft taken from the ground station software (Mission Planner) along with the location of the vertical profiles registered with the DJI P3.

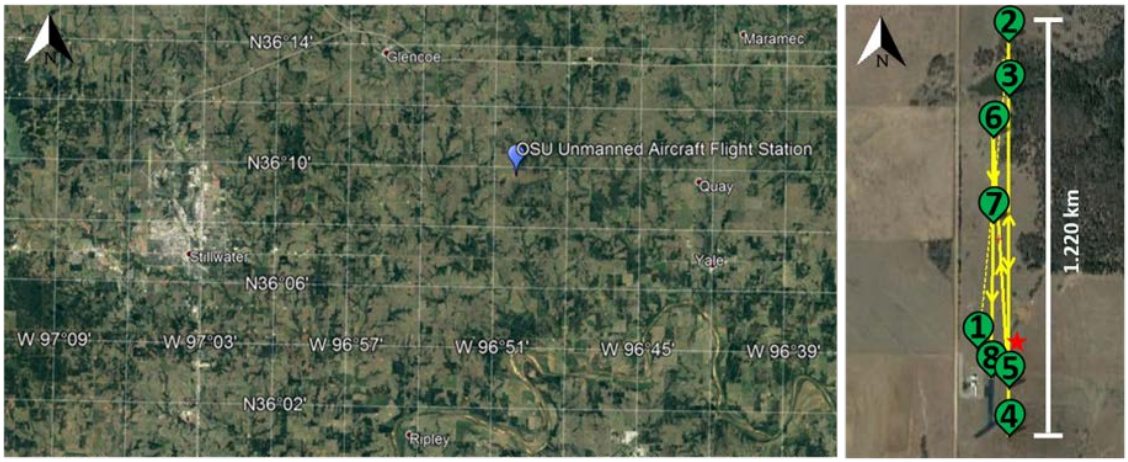

Figure 2.1 (a) A regional map indicating with a blue pin the flight campaign location. For reference, the grid lines defined by latitude and longitude have a length of ~4.5 km. (b) An aerial photo of the Unmanned Aircraft Flight Station with the distance flown by the Skywalker X8 aircraft. The green pins show the horizontal flight pattern connected by yellow arrowed lines following the progression of numbers covered by the Skywalker X8. The red star indicates the fixed coordinates for vertical profiles registered with the DJI Phantom 3 (DJI P3) quadcopter.

2.2.2 Description of Flight Patterns

Two different UAVs are flown simultaneously along different flight patterns to demonstrate a method capable of collecting data needed for box models describing the concentration of trace gases. A DJI P3 quadcopter was flown manually to register the vertical profiles, while a Skywalker X8 was flown on autopilot for the horizontal profiles. The vertical profiles data from 10 to 120 m AGL are reported for the ascent and descent

rates of 3.0 m s^{-1}. The continuous ascending and descending flight pattern is shown with a black trace in Figure 2.2a. The battery changes every 15 min were performed to extend the flying time to 1 h. The black line in Figure 2.2b indicates the fixed coordinates (no horizontal movement) for the global positioning system (GPS) of the DJI P3.

The horizontal profiles at a constant altitude are described by the blue line in Figure 2.2a. The data reported corresponds to straight trajectory flights (~1.220 km length and ~18 m s^{-1} airspeed) lasting for ~1 h after reaching 50 m altitude AGL. The data reported corresponds to continuous flying loops between waypoints 2 and 5 in Figure 2.1b). The GPS trajectories were registered with a VN-300 (VectorNav) during the flights controlled with a waypoint autopilot program on the ground station software (Mission Planner). Figure 2.2b illustrates the latitudinal changes registered with only minimal longitudinal variations from turning around the UAV. The time series for the flight path of the Skywalker X8 is color coded with a rainbow gradient starting with blue at time zero and shifting toward dark red for the end of the flight (1 h).

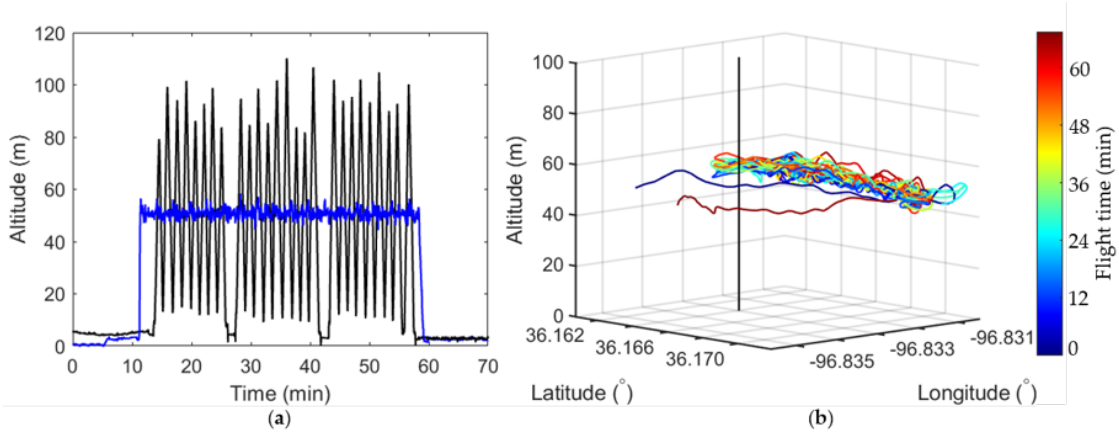

Figure 2.2 The flight patterns for data collection versus the altitude above ground level (AGL). (a) The horizontal profile for (blue) Skywalker X8 and (black) vertical profile for DJI P3 aircrafts. (b) The time series for the progression in the global positioning system (GPS) coordinates with altitude for (rainbow color gradient line) the horizontal and (monochromatic black line) vertical flight paths followed by the Skywalker X8 and DJI P3, respectively.

2.2.3 Gas Sensing Packages

Three portable gas sensing packages were developed to monitor the mixing ratio of NH_3, CH_4, and CO_2. A package with microelectromechanical semiconductor (MEMS) sensors allowed monitoring of the gas NH_3. Similarly, the second package measured CH_4. The third package quantified CO_2 levels with a nondispersive infrared detector (NDIR). The payload for the first, second, and third sensing packages were 227, 230, and 181 g, respectively.

A 10-bit microcontroller (Arduino UNO, Somerville, MA, USA) with a V2 Base Shield (SEEED Studio, Nanshan, China) and a Wireless SD Shield (Arduino) operating at 5.0 V were used to control the sensing packages. Up to 6 h of continuous operation was provided with a 1350 mA h battery (Thunder Power RC 2S, Las Vegas, NV, USA). The data collection set at a rate of 1 Hz was started and stopped with a push-button. The illumination of a light emitting diode (LED) was used to confirm successful data logging for the storage of files in comma separated values (CSV) format to a microSD card with 8

GB capacity (SanDisk Ultra Class 10, Milpitas, CA, USA). The temperature, pressure and percent relative humidity were measured with a BME280 sensor (Bosch, Stuttgart, Germany) with data transmitted via the I2C channel. The mixing ratios for NH_3 and CH_4 were measured with an I2C MiCS-6814, a 3-channel MEMS semiconducting sensor. For CO_2 monitoring, a digital MH-Z16 NDIR sensor was utilized. The calibration curves for the three gases are provided in Figures 2.12–2.14 (Section 2.6: Supplementary Information). The operation of the packages was enabled by writing customized codes for the listed sensors. The gas sensing elements were housed and protected in a 3D printed enclosure made of polylactic acid. A pictorial representation of the sensor packages employed and their position in each aircraft is presented in Figure 2.3. After powering on the sensing packages and re-uploading the code, a time stamp was created. The warm-up and equilibration of the sensors was allowed for at least 1 h before take-off. The results reported below correspond to the flights with identical gas sensing packages placed inside the Skywalker X8 and underneath the DJI P3, as illustrated in Figure 3. For data recovery, the devices were powered down before removing the SD cards.

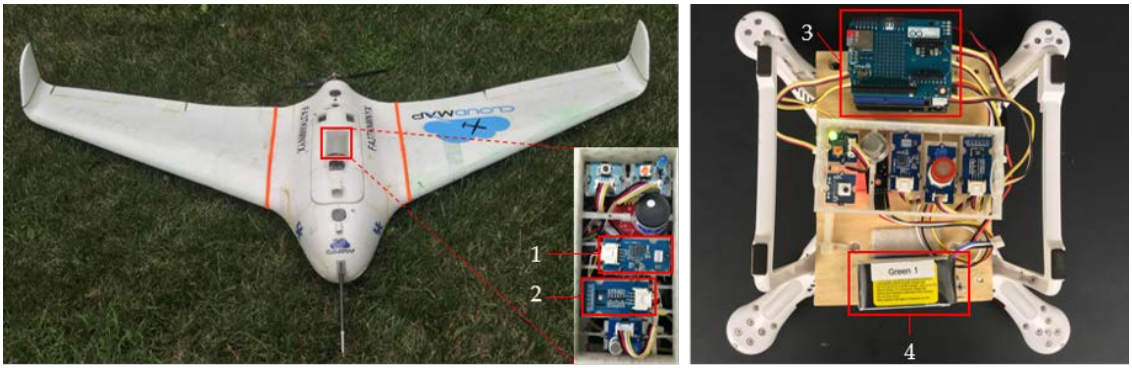

Figure 2.3 Unmanned aerial vehicles (UAV) carrying gas sensing packages. (a) Skywalker X8 with (1) MiCS-6814 and (2) BME280. (b) DJI P3 frame with (3) Arduino UNO Microcontroller with V2 Base Shield and Arduino Wireless SD Shield, and (4) battery.

2.2.4 Correction for Variable Air Speed and Solar Radiation

A series of control flights were used to demonstrate that the response of the factory calibrated sensor packages shielded underneath the DJI P3 quadcopter are in excellent agreement with readings at the ground station. The previous controls discarded any possible distortion on the reading of the sensors due to air speed (meaning the rate of motion of the UAV relative to air) or solar irradiation. Small temperature variations were demonstrated not to affect the readout of other sensor packages, which discarded the need for any dynamic in-situ temperature corrections due to temperature fluctuations within a flight. Thus, when the sensor packages were deployed as indicated in Figure 2.3b, they were shielded from solar radiation with proper aspiration and no further correction to the registered data onboard the DJI P3 quadcopter was required. To test the effect of prop-wash on the sensor package, an experiment was designed to enable simultaneous boundary layer profiles (10–120 m) with a sUAS and tethered weather balloon equipped with the sensor packages. Figures 2.15–2.19 (Section 2.6: Supplementary Information) compare the temperature, relative humidity, methane, carbon dioxide, and ammonia concentration data collected on board the sUAS (black line) and tethered balloon (red line). Figure 2.20 (Section 2.6: Supplementary Information) displays an example for a calibration curve correcting the effect of temperature at different relative humidities. The maximum deviations between the UAV and balloon measurements (Figures 2.15-2.19, Section 2.6: Supplementary Information) does not exceed the accuracy figures established in Tables 2.2 and 2.3 (Section 2.5: Appendix A). Therefore, it has been concluded from these experiments that the prop wash does not affect the meteorological and trace gas readings on the sensor package on board a quadcopter UAV. However, air speed and solar

irradiation introduced a small systematic deviation of the response of sensor packages in the Skywalker X8. The systematic testing demonstrated that the modified behavior onboard the Skywalker X8 was largely created by the air scoop generated over the UV radiation shield enclosing the sensor packages located on top of the aircraft, together with a minor contribution from solar irradiation.

A two-stage set of laboratory controls was designed to correct the response of the sensors for the variable air speed and solar irradiation conditions experienced by the sensor packages onboard the Skywalker X8 during the flights. During the first set of controls, the fuselage of the sUAS carrying the sensors was placed inside a 0.6 × 0.6 × 1.2 m wind tunnel (Model 404B, Engineering Laboratory Design Inc., Lake City, , MN, USA) and exposed to a range of wind speeds from 5 to 27 m s^{-1} to simulate and bracket the effects of airflow over the sensors experienced during data flights with the Skywalker X8. A partial correction factor for the sensor packages that deviated from zero air speeds was obtained.

In the second set of controls, a light source was used to correct for the effects of solar irradiation on the sensor packages protected by a polylactic acid enclosure. For this purpose, a collimated 1 kW high-pressure Hg (Xe) arc lamp was employed to provide actinic radiation in the solar window after removing (1) infrared radiation with a water filter and (2) UV C light with a cutoff filter for wavelength $\lambda \geq 280$ nm.[80] In addition, neutral density filters were employed to attenuate the light and simulate varying levels of sunlight irradiation[81] experienced by the sensor packages in the flight field. A spectral irradiance microspectrometer (Ocean Optics, Dunedin, FL, USA) was used to determine the effective light intensity employed under various attenuations. Thus, a second partial

correction factor accounting for the effect of solar irradiation was established for a range of sunlight intensities.

The effect of air speed and solar radiation is modeled and then corrected using MATLAB 2016B. The trace gas mixing ratios are measured systematically over a range of all expected air speeds and solar radiation. The data from these experiments was inputted into a MATLAB script and the effects were observed to determine the overall trends and the relative magnitudes each variable had on every trace gas mixing ratio measured. Next, an algorithm was developed to model all air speeds and solar radiation experienced. Once the effects were well understood mathematically, the deviations were corrected for the appropriate variable. The final overall correction factor combined the partial effects described above by correcting the data sets to an operational air speed of 18 m s^{-1} and varying the amount of sunlight irradiation.

2.2.5 Experiments for Data Collection

All data reported was collected between 26 and 29 June 2017. There were four experiments each day consisting of multiple flights. The temperature, percent relative humidity, and pressure were measured during every flight. A typical experiment lasted for approximately 1 h. For example, the first and second experiments on 28 June 2017 took place in the intervals 6:04–6:56 am (UTC–5 h) and 7:06–7:57 am (UTC–5 h) to measure NH_3 and CH_4 respectively. The third experiment only collected physical information and occurred from 8:11 to 9:05 am (UTC–5 h). The first quantification of CO_2 was registered during the fourth experiment, which took place in the interval 9:28–10:22 am (UTC–5 h).

2.2.6 Data Analysis

MATLAB R2016B was used for data processing and plotting. The vertical profile gas measurements up to 120 m altitude AGL were resolved by matching the ascent/descent rate with the data logging rate, creating 40 measurements each per ascent and descent. The reported values in the figures correspond to the average mixing ratio recorded every 3 m altitude [82], with error bars representing one standard deviation. The horizontal profiles were position resolved using the GPS measurements from the VN-300. The GPS data was block averaged to coincide with the 1 Hz logging rate of the trace gas measurements. The figures represent data points averaged every 18 m for latitude or 3 m for altitude depending on the flightpath. The averaged datapoints and variance of each averaged datapoint is illustrated in Figures 2.5, 2.7-2.10. This variance was reflective of real measurement deviation, and not attributed to measurement error. Further statistical analysis was achieved by calculating the standard error of the mean (SEM) for all averaged horizontal and vertical profiles. Specifically, the average measured value with a 95% confidence interval is reported for the profiles of temperature, relative humidity, methane, ammonia, and carbon dioxide.

2.3 Results and Discussion

This section reports data collected during 4 experiments on 28 June 2017. The physical measurements are presented first, showing the evolution of the temperature and relative humidity during a single flight, and over the course of the four flights. The measurements of the trace gases NH_3, CH_4, and CO_2 are shown later.

2.3.1 Physical Measurements

The measurements of the temperature, pressure, and percent relative humidity were taken onboard the Skywalker X8 and DJI P3 during each flight. These variables characterize the environment during the flights and facilitate the critical evaluation of sensor outputs that may be affected by varying environmental conditions. The evolution of temperature and relative humidity throughout a single flight, and throughout the early part of the day when major variability exist, is presented next.

2.3.1.1 Temperature Profiles

Figure 2.4 displays an example for a horizontal temperature profile at a constant 50 m altitude AGL during the course of an early morning flight that took off at 7:06 am (UTC–5 h) and landed at 7:57 am (UTC–5 h) on 28 June 2017. The progression of the flight time is illustrated using a color-bar, which shows blue at the beginning and consistently red-shifts until the conclusion of the flight. For reference, the sun was rising as the Skywalker X8 was completing its 51 min flight path and a continuous increase in the ambient air temperature from 23.3 to 24.8 °C due to increased solar irradiance from the beginning to the end of the flight was captured for this Oklahoma summer sunrise. This small temperature variation neither affected the output of other sensors nor the determination of mixing ratios for trace gases.

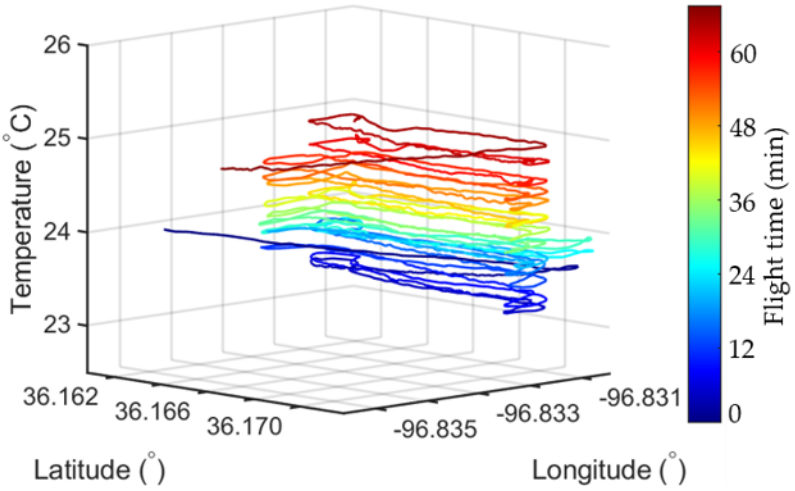

Figure 2.4 GPS-resolved temperature measurements along the Skywalker X8 flight path at 50 m AGL from 7:06 to 7:57 am (UTC–5 h) on 28 June, 2017. The color bar to the right-hand side represents the progression of time from blue in the beginning to red at the end of this latitudinal flight path.

Figure 2.5 shows the temperature profiles from consecutive flights performed throughout 28 June 2017, which captured the typical morning temperature inversion resulting from the diurnal cycle. Figure 2.5a depicts the constant temperature measurements along each horizontal flight path of the Skywalker X8. The four flights took place in the intervals 6:04–6:56 am, 7:06–7:57 am, 8:11–9:05 am, and 9:28–10:22 am (UTC–5 h) and are colored in green, blue, red, and black lines, respectively. From bottom to top in Figure 2.5a, the mean and SEM of the temperature profiles are 24.01 (± 0.02), 24.26 (± 0.05), 26.02 (± 0.06), and 27.36 (± 0.12) °C. The variance in the temperature measurements in Figure 2.5a increases as the day progresses, which reflects an increase in convective turbulent motions due to less stable boundary layer conditions formed as the sun rises and the ground begins to radiate heat. Figure 2.5b shows the vertical temperature profiles collected onboard the DJI P3 with mean and SEM values of (from left to right) 23.88 (± 0.05), 24.36 (± 0.07), 26.04 (± 0.08), and 27.38 (± 0.07) °C.

Figure 2.5b shows that the first three DJI P3 flights display a relatively stable atmosphere during each flight with practically no temperature change from 15 to 100 m AGL. The greatest temperature gap in the vertical profiles (Figure 2.5b) occurs between the second and third flights, indicating a warming rate of ~3.5 °C h^{-1}, which coincides with the temperature increment of solar irradiation warming the Earth's surface. The largest temperature variation and associated uncertainty for each vertical profile (Figure 2.5b) occurs close to the surface, as expected, due to a reduction in turbulent transport near the surface and reflecting a more inefficient heat exchange by conduction. Overall, reliable temperature readings were provided by both the Skywalker X8 aircraft and the DJI P3 quadcopter.

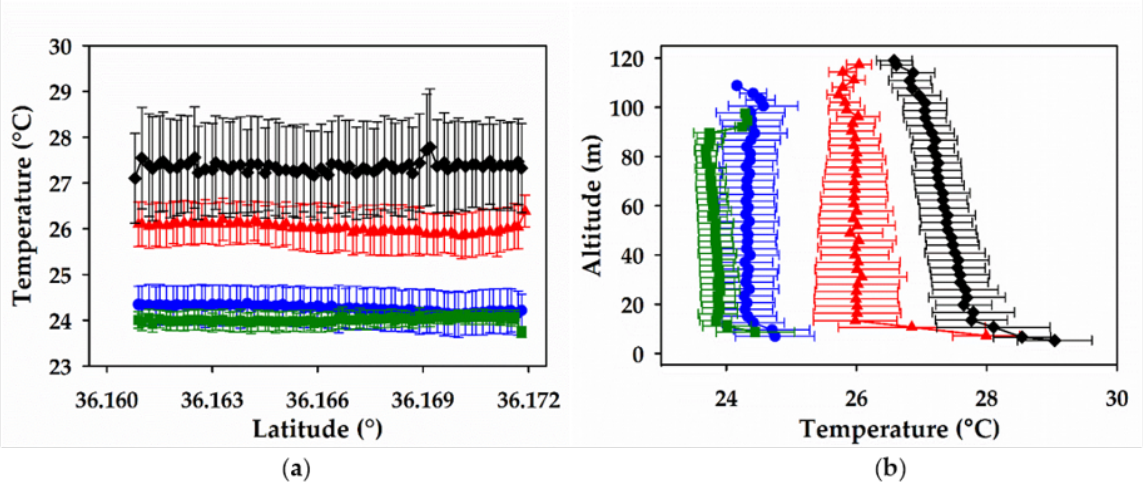

Figure 2.5 (a) The horizontal and (b) the vertical flight paths measuring temperature variations during the morning of 28 June, 2017 for the times (green square) 6:04–6:56 am (UTC–5 h), (blue circle) 7:06–7:57 am (UTC–5 h), (red triangle) 8:11–9:05 am (UTC–5 h), and (black diamond) 9:28–10:22 am (UTC–5 h).

2.3.1.2 Relative Humidity Profiles

Figure 2.6 presents an example of a relative humidity horizontal profile recorded simultaneously with the temperature for the same flight in Figure 2.4 at a constant 50 m altitude AGL. A decrease in relative humidity from 79 to 74% is depicted for the

Skywalker X8 flight over time, as shown by the progression from blue to red-shifting of the flight time in the color bar on the right of Figure 2.6. A direct comparison of Figures 2.4 and 2.6 for the 51 min flight indicates the 6.3% relative drop in relative humidity is accompanied by a 6.4% rise in temperature. Thus, a drop in relative humidity is expected with a rise in temperature given that the specific water content does not change.

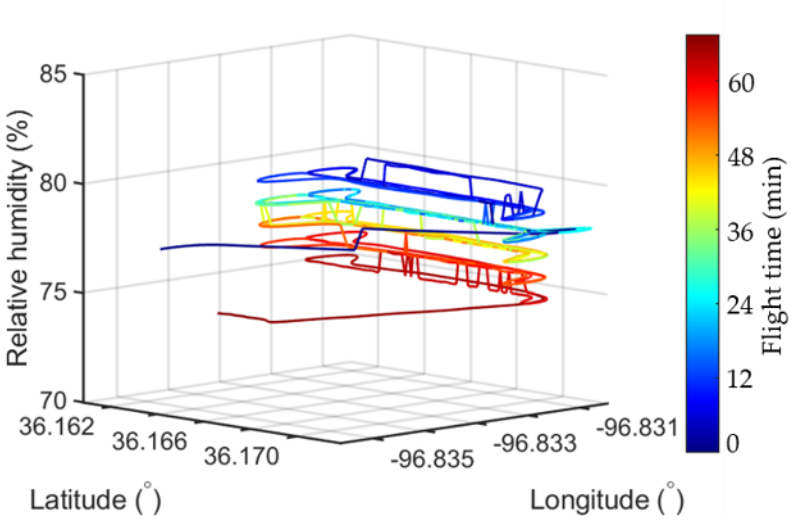

Figure 2.6 GPS-resolved relative humidity measurements along the horizontal flight path during the morning of 28 June, 2017, from 7:06 to 7:57 am (UTC–5 h). The color bar represents the progression of flight time from blue in the beginning to red at the end of the flight.

Figure 2.7 presents the relative humidity measurements for consecutive flights performed on 28 June 2017, which simultaneously recorded the temperature data shown in Figure 2.5. Figure 2.7a shows that the relative humidity remains practically constant within each horizontal flight, while Figure 2.7b reveals small vertical variations occur with altitude. The data in the horizontal and vertical profiles of Figure 2.7 clearly illustrates how the relative humidity drops from sunrise to late morning. It is apparent that relative humidity starts to decay near the ground and that as the Earth's surface begins to warm, the effect is accelerated. As expected, the greatest decrease in relative humidity coincides

with the largest increases in temperature. The largest drop of 10.3% in relative humidity is observed between the second and third flights. From top to bottom in Figure 2.7a, the vertical profiles show relative humidities with means and SEMs of 82.96 (± 0.28) %, 77.65 (± 0.25) %, 68.57 (± 0.32) %, and 59.98 (± 0.25) %, respectively. From right to left in Figure 2.7b, the horizontal profiles display relative humidities with means and SEMs of 82.75 (± 0.09) %, 77.51 (± 0.15) %, 68.57 (± 0.23) %, and 59.97 (± 0.39) %, respectively. Similar to the temperature measurements (Figure 2.5a), an increase in the variance of relative humidity is also evident in Figure 2.7a, which coincides with the mixing and destabilization of the planetary boundary layer. However, the similar variance of ~0.2% in relative humidity measurements of horizontal and vertical profiles indicates both sUAS employed are reliable platforms for studying this property. Overall, this work demonstrates that the BME280 sensor collects accurate measurements of temperature and relative humidity on board the DJI P3 and Skywalker X8 sUAS.

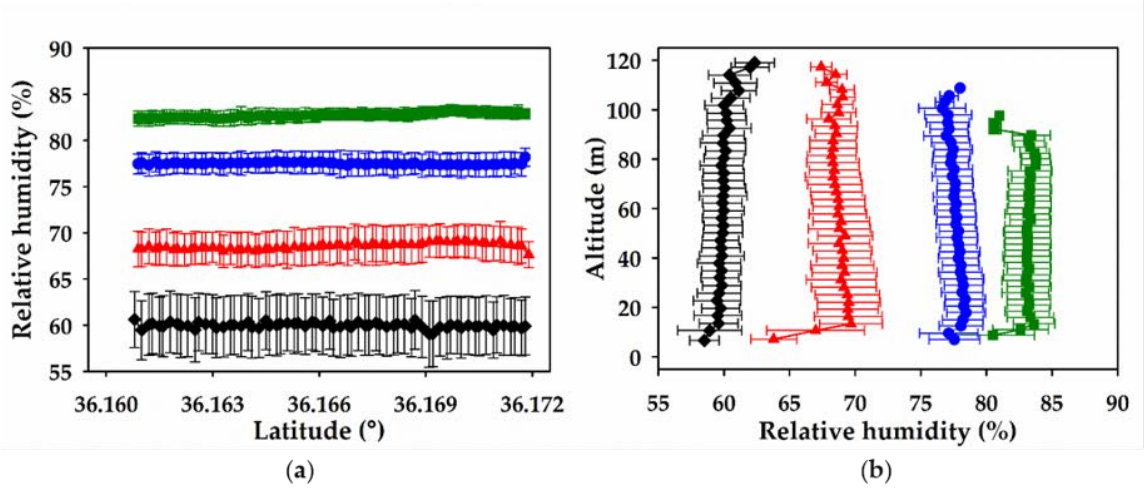

Figure 2.7 (a) The horizontal and (b) the vertical flight paths measuring relative humidity variations during the morning of 28 June, 2017 for the times (green square) 6:04–6:56 am (UTC–5 h), (blue circle) 7:06–7:57 am (UTC–5 h), (red triangle) 8:11–9:05 am (UTC–5 h), and (black diamond) 9:28–10:22 am (UTC–5 h).

2.3.2 Trace Gas Measurements

Trace gases were concurrently measured with physical properties onboard the Skywalker X8 and DJI P3. Three trace gases were quantified during this campaign: NH_3, CH_4, and CO_2. These gases were measured in several flights and gathered in three different groups for practical purposes. NH_3 was measured during one set of flights, a different set of flights measured CH_4, and a third set of flights measured CO_2.

2.3.2.1 Ammonia Profiles

Figure 2.8 shows an example of the data collected during flights measuring NH_3. In this example from the morning of 28 June 2017, the gases were measured from 6:04 to 6:56 am (UTC–5 h) using the Skywalker X8 for the horizontal profiles (Figure 2.8a), and the DJI P3 for the vertical profiles (Figure 2.8b). The mixing ratios measured during the fixed wing flight (Figure 2.8a) had an average and SEM of 5.58 (± 0.01) ppbv NH_3. The average and SEM for the mixing ratios detected during rotary wing flights vertical profiling (Figure 2.8b) were 5.58 (± 0.04) ppbv NH_3. The dataset in Figure 2.8 demonstrates the ability of the MiCS-6814 sensor to accurately detect NH_3 at typical tropospheric levels.

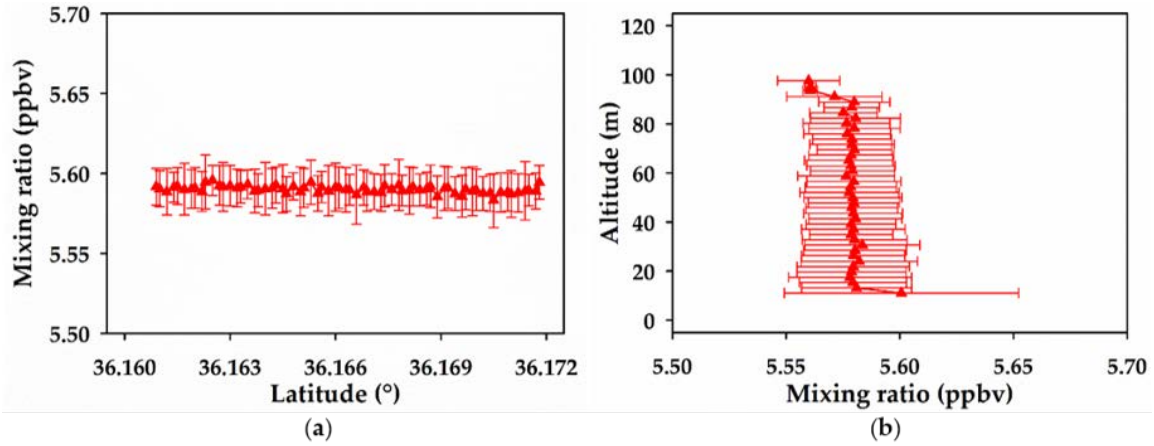

Figure 2.8 (a) The horizontal and (b) the vertical flight paths measuring the variable mixing ratio of (red triangle) NH_3 during the morning of 28 June, 2017 from 6:04 to 6:56 am (UTC–5 h).

2.3.2.2 Methane Profiles

Figure 2.9 demonstrates the ability of the MiCS-6814 sensor to detect methane, at atmospherically relevant mixing ratios. The example in Figure 2.9 displays the measured mixing ratios for CH_4 from the flights conducted on 28 June, 2017 from 7:06 to 7:57 am (UTC–5 h) using a different channel of the MiCS-6814 sensor. The average mixing ratios (and SEM) for the horizontal profile in Figure 2.9a were 1792.05 (± 1.49) ppbv CH_4, and the corresponding average temperature and relative humidity were 24.26 (± 0.05) °C and 77.51 (± 0.15) %, respectively. For the vertical profiles in Figure 2.9b, the average mixing ratios (and SEM) were 1792.93 (± 6.76) ppbv CH_4, during a flight that averaged a temperature and relative humidity of 24.36 (± 0.07) °C and 77.65 (± 0.25) %, respectively.

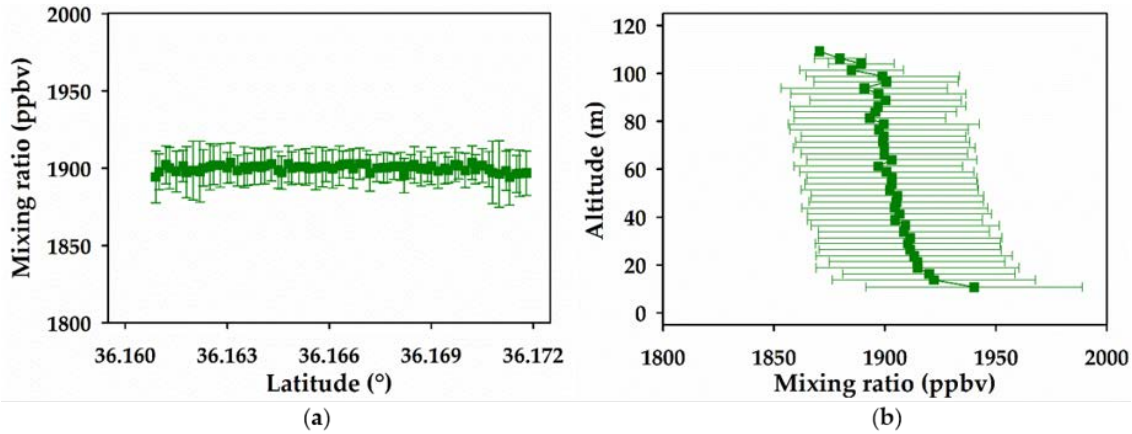

Figure 2.9 (a) The horizontal and (b) the vertical flight paths measuring the variable mixing ratio of (green square) CH_4 during the morning of 28 June, 2017 from 7:06 to 7:57 am (UTC–5 h).

2.3.2.3 Carbon Dioxide Profiles

Figure 2.10 shows how the MH-Z16 NDIR sensor can detect CO_2 at atmospherically relevant mixing ratios both during the horizontal and the vertical flights. For example, Figure 2.10a shows the average mixing ratio (and SEM) of CO_2, the temperature, and relative humidity were 411 (± 2), 27.36 (± 0.12) °C, and 59.97 (± 0.39) % for the horizontal profile, respectively. Similarly, the vertical profile in Figure 2.10b displays an average (and SEM) value of 420 (± 2) ppmv CO_2, associated to a mean temperature of 27.38 (± 0.07) °C and an average relative humidity of 59.98 (± 0.25) %.

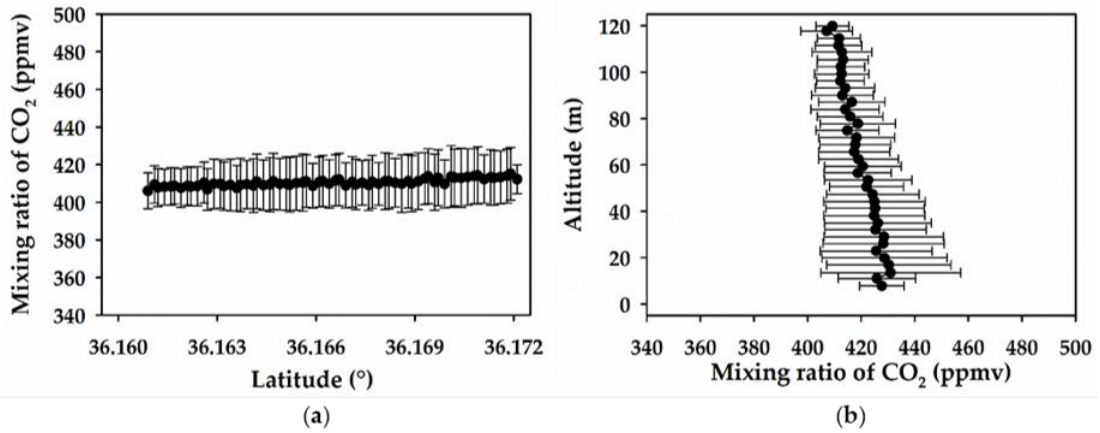

Figure 2.10 (a) The horizontal and (b) the vertical flight paths measuring the variable mixing ratio of CO_2 during the morning of 28 June, 2017 from 9:28 to 10:22 am (UTC–5 h).

Figure 2.11 displays the horizontal and the vertical profiles for the detection of CO_2 mixing ratios during several programmed gas releases to simulate leaks increasing the environmental background level. Indeed, the work in Figure 2.11 demonstrates that the detection of gas leaks, even as they dilute in the atmosphere, can be monitored employing the developed sensor technology with sUAS.

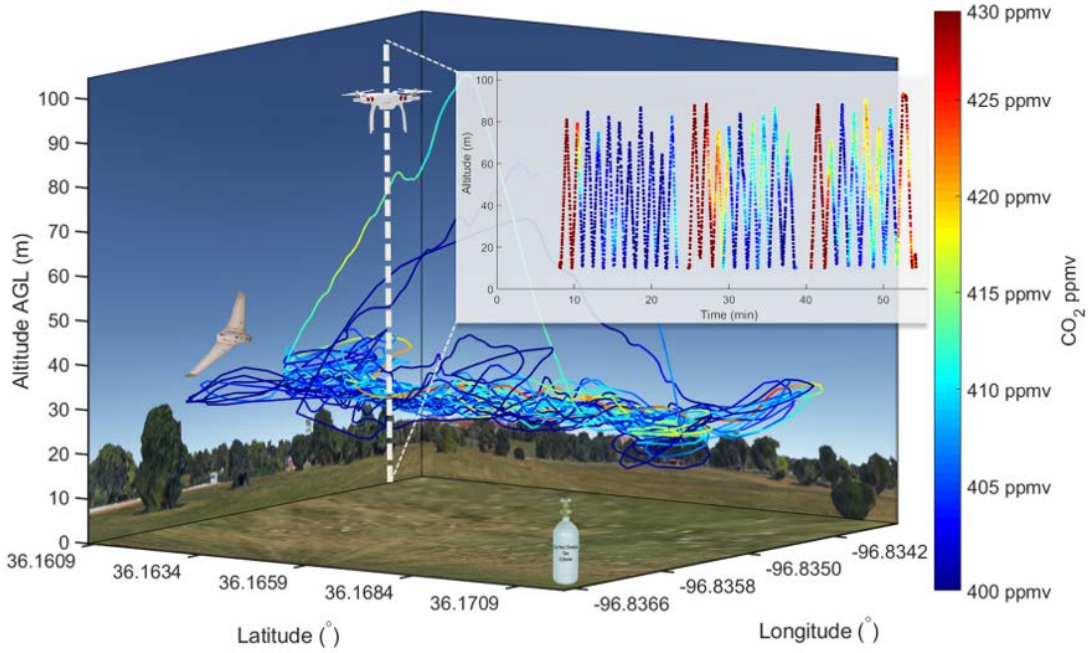

Figure 2.11 The horizontal and the vertical flights for the detection of induced leaks of CO_2 (released from the location of the cylinder) during 27 June, 2017 from 1:15 to 2:02 pm (UTC–5 h).

2.3.2.4 Environmental Implications of sUAS for Monitoring Trace Gases

Three trace gases (ammonia, methane, and carbon dioxide) were successfully quantified during the second CLOUDMAP flight campaign in Oklahoma. The location of the site and the topography where the flights took place were typical of a rural farmland, what resulted in an optimal combination to measure environmentally relevant mixing ratios of trace gases with the Skywalker X8 and the DJI P3. Remarkably, the similar mixing ratio values registered for each gas at the same altitude (50 m AGL) indicates both platforms are independently robust. For example, based on the data on the integration of repeated measurements presented in Table 2.1, the differences between the horizontal and the vertical mean mixing ratios at 50 m AGL are 0 ppbv for NH_3, 1.3 ppbv for CH_4, and 2 ppmv for CO_2. In addition, to demonstrate the capability for gas detection at variable

altitudes, the mean mixing ratios at 90 and 15 m AGL are provided together with the reference value (RV) determined at the nearby Mesonet. The agreement between the two platforms demonstrates that any effects from air speed and/or solar irradiance has been well understood and corrected to enable consistent measurements with the fixed and rotary wing sUAS. The work also serves as an example showing how this technology can be used to collect the vertical and horizontal profiles of gas levels needed to (1) create a two-dimensional box model covering a slide of 120 km^2 per flight and (2) to measure atmospheric composition along extensive gas ducts employing sUAS [83] to constrain the region of hydrocarbon leaking during transport.

Table 2.1 Reproducibility Analysis and Comparison to Reference Values (RV).

Total Exp.	**Gas**	**Mean Mixing Ratio (ppbv, except for CO_2 that is in ppmv)**				
		Skywalker X8		DJI P3		RV
		50 m AGL	50 m AGL	90 m AGL	15 m AGL	
2	CH_4	1899.8 (± 5.4)	1898.5 (± 52.6)	1855.2 (± 30.1)	1914.1 (± 59.7)	1898.4
2	NH_3	5.58 (± 0.01)	5.58 (± 0.04)	5.56 (± 0.04)	5.59 (± 0.05)	5.58
3	CO_2	409 (± 8)	407 (± 20)	405 (± 20)	409 (± 20)	407.71

In addition, the sensor packages provided mixing ratios that were also in excellent agreement with reported values for this region from the Environmental Protection Agency (EPA) and/or the National Oceanographic and Atmospheric Administration (NOAA) of the United States of America.[76] For example, the nearest Ammonia Monitoring Network (AMoN) station (36°55′19″ N, −94°50′20″ W) located approximately 209 km away detected 5.58 ppbv NH_3[84] on 28 June 2017. The NOAA Atmospheric Radiation Measurement (ARM) site (36°36′25″ N, −97°29′20″ W) about 64 km away from our field campaign site was used to compare CH_4 measurements. In addition, on 30 June 2016, the

methane levels at the ARM site were 1898.48 ppbv.[85] Lastly, the Mauna Loa weekly average for the week of 25 June 2017 was 407.71 ppmv CO_2.[86]

2.4 Conclusions from 2017 CLOUDMAP Campaign

A major challenge in quantifying trace gases at low altitudes is the lack of available sampling techniques capable of providing measurements with a spatiotemporal resolution on the order of meters and seconds. Currently, there are not many devices that can be readily incorporated into commercially available UAVs. This work reported the creation and use of trace gas sensor packages integrated into Skywalker X8 fixed wing, the DJI P3 rotary wing, and sUAS. The devices were calibrated for environmental conditions and flown at the second CLOUDMAP campaign. The results gathered through a series of example flights described the sensor package's ability to report temperature and relative humidity evolution throughout a single flight and over the course of several hours. Furthermore, the work analyzed datasets from typical flights and confirmed that the fixed wing and rotary wing platforms provide similar readings, and the trace gas quantifications agree well with relevant EPA and NOAA atmospheric mixing ratios. Therefore, this work has demonstrated that these sensor packages can accurately measure temperature, relative humidity, latitude, longitude, pressure (altitude), ammonia, methane, and carbon dioxide. This device can serve as a useful tool to determine weather conditions and quantify trace gas mixing ratios, particularly at sites of greenhouse and toxic gas pollution. Future applications of this device for environmental monitoring should help to constrain the uncertainty of low altitude (<100 m) trace gas measurements without serious safety concerns or extensive costs. Among the main advantages of the reported analytical platform are the short time needed from set up to deployment (just minutes), and the fact

that the analysis can last for up to 1 h covering areas of 120 km^2 with high spatiotemporal resolution.

2.5 Summary of Sensor Specifications

Table 2.2 Gas Sensor Specifications

Gases	Operating Range (ppbv)	Accuracy (% of Measured Value)	Precision (ppbv)	Resolution (ppbv)
Methane	1000–6000	±1.24%	180	10
Ammonia	500.0–9040	±0.20%	30	10
Carbon dioxide	80,000–1,622,000	<±1%	<2000	1000

Table 2.3 Meteorological Sensor Specifications

Meteorological Variable	Accuracy	Precision	Response Time
Temperature	±1.0 °C	±0.005 °C	0.5 s to 66% full signal
Pressure	±1.0 hPa	±0.002 hPa	-
Relative Humidity	±3%	±2%	1 s to 63% of full signal

2.6 Supplementary Information

The calibration curves 2.12, 2.13, and 2.14 for the methane (CH_4), carbon dioxide (CO_2), and ammonia (NH_3) gas sensors are provided below. Methane and carbon dioxide gas sensors were calibrated using primary certified gas and certified calibrated mass flow controllers. All concentrations are accurate within ± 1%. The gas sensors were calibrated in an environmental chamber where the gas composition, temperature and relative humidity were controlled.

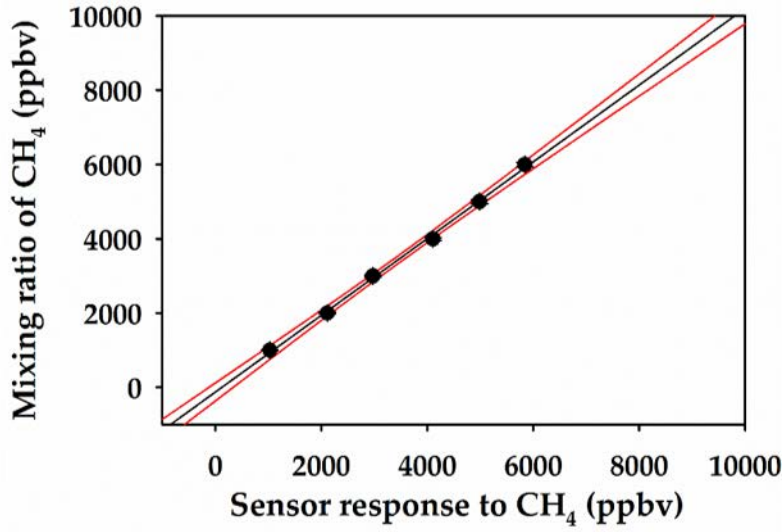

Figure 2.12 Methane calibration curve from 1000-6000 ppbv. y = 1.033(x) -122.0, where y represents the concentration of the gas of interest (in parts per billion by volume of air) and x the response of the sensor. The coefficient of determination for the straight line is $R^2 = 0.9981$.

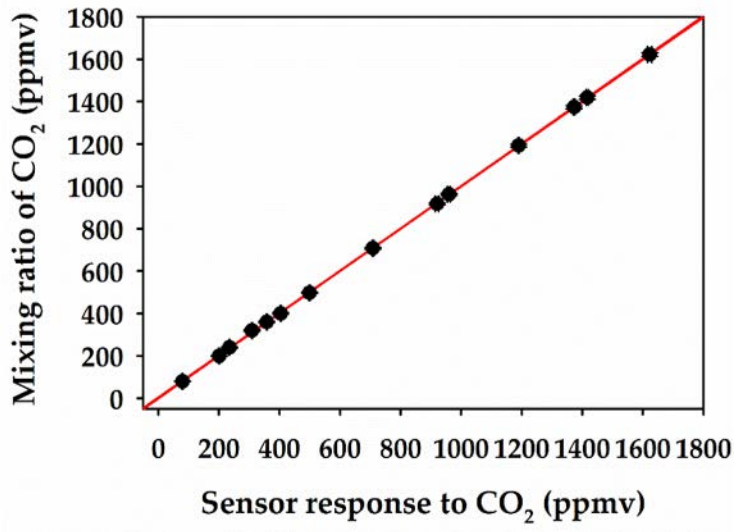

Figure 2.13 Carbon dioxide calibration curve from 80.00-1622 ppmv. y = 0.9993x – 1.682, where y represents the concentration of the gas of interest (in parts per billion by volume of air) and x the response of the sensor. The coefficient of determination for the straight line is $R^2 = 0.9999$.

The ammonia calibrations were achieved by using the custom environmental chamber. In brief, it is a sealed chamber that allows for total control of atmospheric composition. The ammonia vapor produced by ammonium hydroxide solutions of various

volumes were used to calculate the theoretical ppbv of ammonia gas in the chamber. The stock ammonium hydroxide solution was 29.28%, or 15.45 M. Ammonium hydroxide forms ammonia and water as described in the acid base reaction below. The K_b of the reaction is provided in Equation 2.1.

$$NH_3(g) + H_2O\,(l) \rightleftharpoons NH_4^+(aq) + OH^-(aq) \qquad Reaction\ 2.1$$

$$K_b = \frac{[NH_4^+][OH^-]}{[NH_3]} = 1.89 \times 10^{-5} \qquad Equation\ 2.1$$

The mole fraction of free NH_3 in solution was calculated using the pK_a and pH of the solution at 24 ˚C, and described in Equation 2.2.

$$NH_3(aq) = [10^{(pK_a - pH)} + 1]^{-1} \qquad Equation\ 2.2$$

Given that the pH of the 15.45 M stock solution was 11.60, 99.53% of the ammonium hydroxide was present as ammonia. Next, the partial pressures of ammonia and water were used to calculate the mass fraction of ammonia present as vapor above the solution. The fraction was multiplied by the mass of ammonium hydroxide in solution and converted in µg. The mass was converted to ppbv by dividing the µg of ammonia vapor by the volume of the chamber in L to get ppbv. The calibration curve for the ammonia sensor is shown in Figure 2.14.

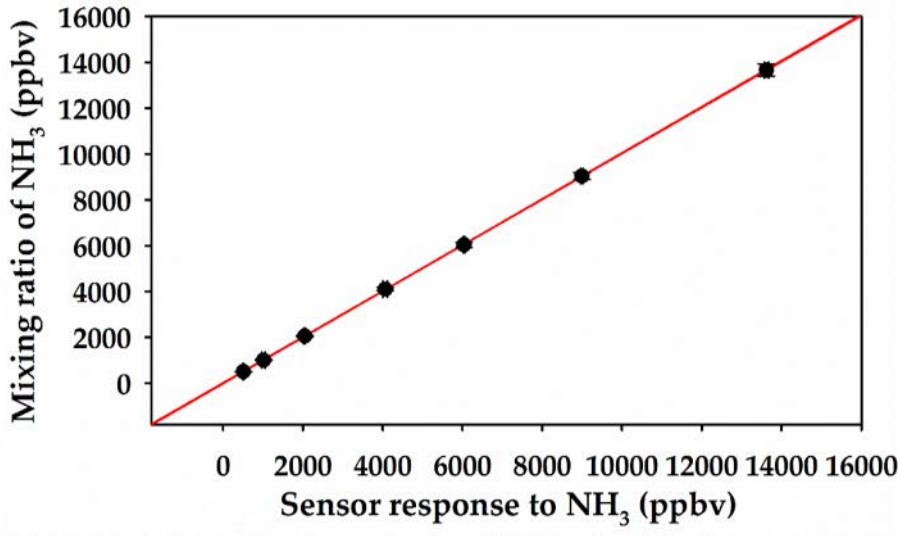

Figure 2.14 Ammonia calibration curve from 500.0-9040 ppbv. y = 1.003(x) – 0.0037, where y represents the concentration of the gas of interest (in parts per billion by volume of air) and x the response of the sensor. The coefficient of determination for the straight line is $R^2 = 0.9999$.

To test the effect of prop-wash on the sensor package, an experiment was designed to enable simultaneous boundary layer profiles (10-120 m) with a sUAS and tethered weather balloon equipped with the sensor packages. Figures 2.15-2.20 compare the temperature, relative humidity, methane, carbon dioxide, and ammonia concentration data collected on board the sUAS (black line) and tethered balloon (red line). It is important to note that during the 2018 ISARRA LAPSE-RATE campaign, it was learned that the BME280 sensor (for temperature, pressure, and relative humidity) needs proper aspiration to be accurate [87].

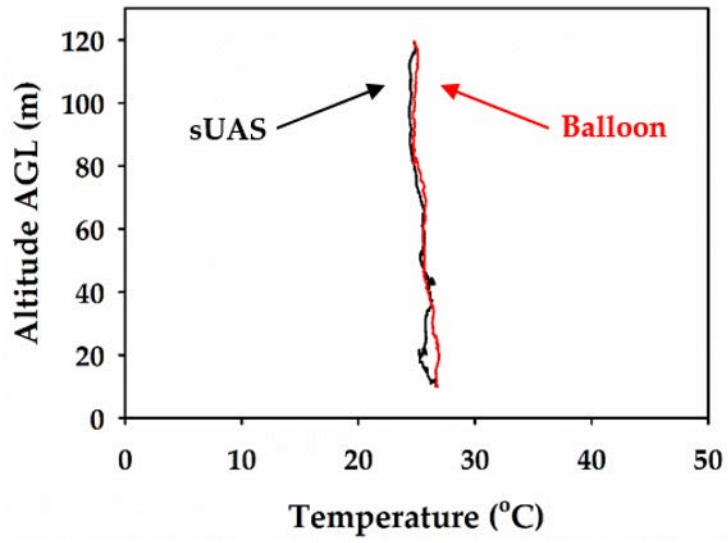

Figure 2.15 Temperature profiles above ground level (AGL) captured by a (black) DJI P3 quadcopter and (red) a balloon.

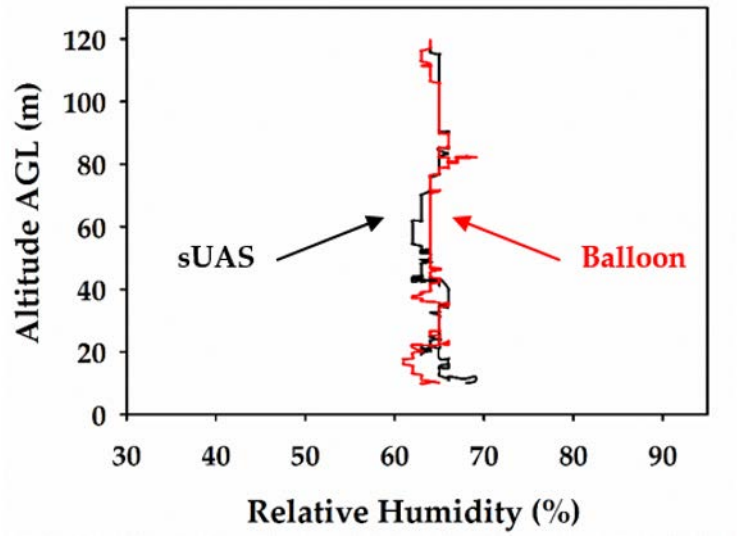

Figure 2.16 Relative humidity profiles AGL captured by a (black) DJI P3 quadcopter and (red) a balloon.

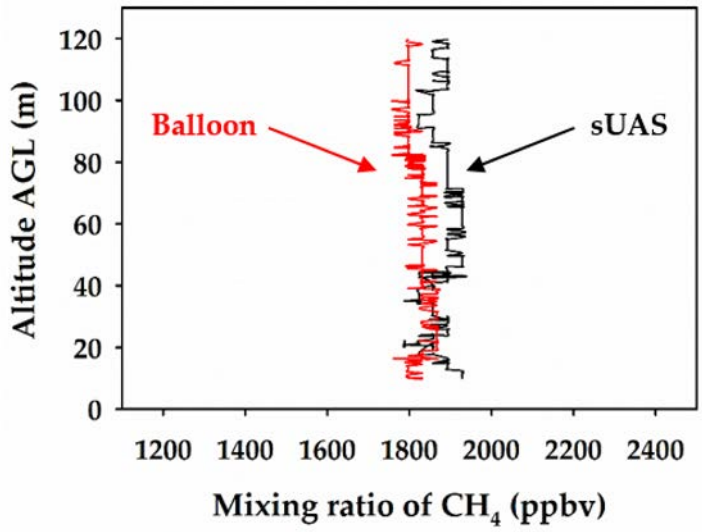

Figure 2.17 Methane profiles AGL captured by a (black) DJI P3 quadcopter and (red) a balloon.

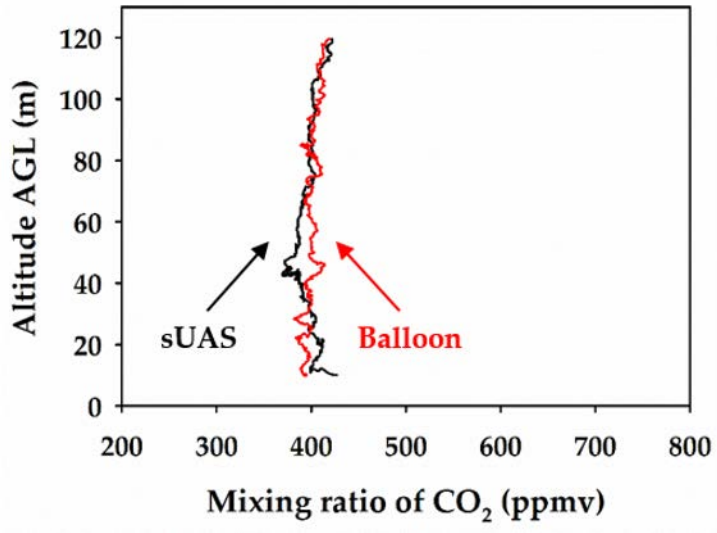

Figure 2.18 Carbon dioxide profiles AGL captured by a (black) DJI P3 quadcopter and (red) a balloon.

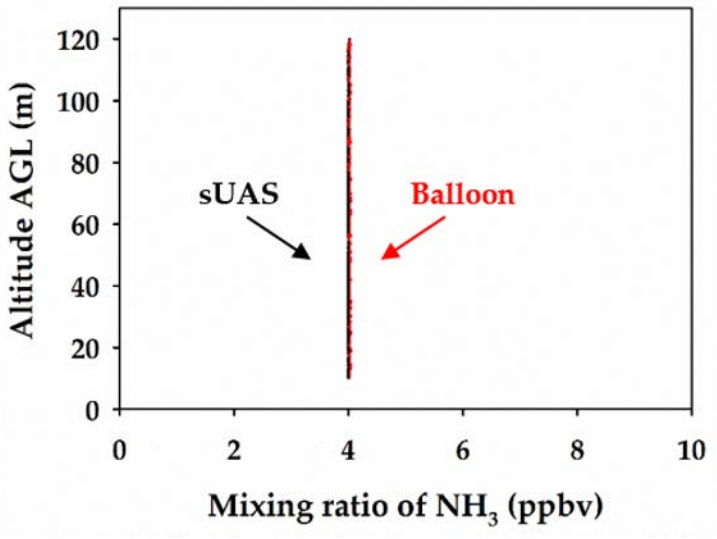

Figure 2.19 Ammonia profiles AGL captured by a (black) DJI P3 quadcopter and (red) a balloon.

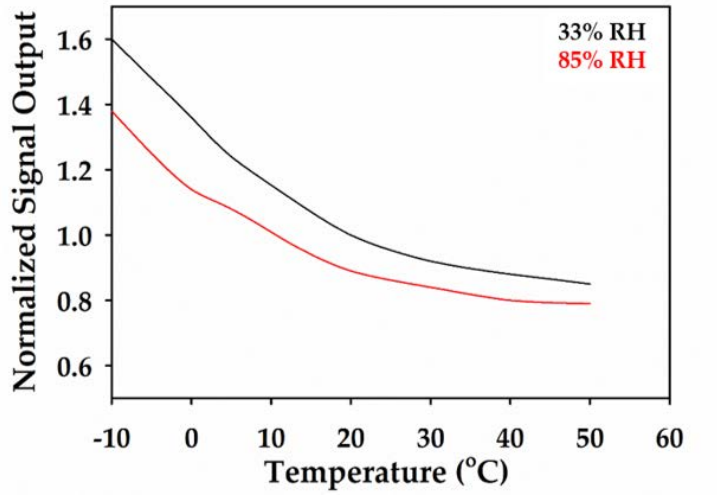

Figure 2.20 Calibration curve correcting the effects of temperature from -10 to 50 °C at low (33%) and high (85%) relative humidity [43].

This has been used as a starting place to successfully correct the sensor data for significant environmental changes. Corrections for the effects of extreme weather can be enabled in device software or could be corrected after if absolutely necessary.[43] However, corrections for weather conditions are not needed for all sensors. For example, the MH-Z16 sensor for carbon dioxide measures its own temperature and uses that temperature measurement to provide a self-calibrated measurement. It is also unaffected by water vapor, so it does not need to be corrected for different humidity's. Thus, there is no need for any corrections to the CO2 sensor due to varying meteorological conditions.

CHAPTER 3. APPLICATION OF A SMALL UNMANNED AERIAL SYSTEM TO MEASURE AMMONIA EMISSIONS FROM A PILOT AMINE-CO_2 CAPTURE SYSTEMS

Reproduced with Permission from:

Travis J. Schuyler, Bradley Irvin, Keemia Abad, Jesse G. Thompson, Kunlei Liu, and Marcelo I. Guzman. Application of a Small Unmanned Aerial System to Measure Ammonia Emissions from a Pilot Amine-CO_2 Capture System

Submitted to Earth and Space Chemistry

3.1 Introduction

The use of unmanned aerial systems (sUAS) has expanded significantly in the scientific community over the last few years. Recent studies have demonstrated the usefulness of sUAS for providing novel measurements in the boundary layer previously infeasible with existing methods (i.e. ground stations, towers, weather balloons, manned aircraft, satellites).[88-90] These studies illustrate several advantages that motivate the incorporation of sUAS for atmospheric measurements. The ability to provide nearly instant real-time emission estimates without the traditional lead times that accompany wet-lab analysis is desirable in industrial applications. Furthermore, the sUAS package is cheaper than traditional instrumentation and does not constantly consume reagents during the analysis.[76] The occasional replacement of batteries is the primary upkeep cost of the sUAS, therefore it is cost effective to purchase and maintain. The sUAS can also provide insight into the emission plume and how the emission levels change as they diffuse into the lower atmosphere, enabling further atmospheric studies enlightening the effects of pollution on

a larger scale. Because of the widespread pollution of anthropogenic carbon dioxide (CO_2), coal burning powerplants are a primary case study for industrial applications of sUAS for quantification of point source pollution.

Coal burning power plants emit 4.90×10^3 Tg of carbon dioxide (CO_2) a year, accounting for ~21% of all CO_2 emitted throughout the United States of America (U.S.A.) in the year 2017.[91] It is well-known that CO_2 gas absorbs infrared radiation and traps heat in the Earth's atmosphere, working as a greenhouse gas.[92] As a result, continued anthropogenic CO_2 pollution increases radiative forcing, leading to an increase in average global surface temperature.[92] Thus, practical technologies that counteract the projected increase in CO_2 emitted are needed, which should not significantly change the existing methods of energy production.[93] There are numerous strategies to mitigate the effect of fossil fuel burning power plants and counteract pollution due to the constantly amplifying demand for energy in the last decades.[93, 94] An effective way to reduce emissions in existing coal burning power plants is to retroactively fit (retrofit) them with carbon capture systems (CCS),[95, 96] which trap and remove CO_2 from the flue gas.[97] One successful solution employs a post-combustion treatment of the flue gas via absorption of the CO_2 with a circulating amine solvent, with a potential emission reduction of up to 90%.[98-104] Many of the 359 coal burning power plants that operate across the U.S.A.[105] can potentially be fitted with CCS technology. Currently, 65 large-scale projects have started retrofitting carbon capture technologies in the U.S.A.[106]

Ammonia (NH_3) gas can be produced from a variety of sources, and has been identified in low quantities as a byproduct from amine-based CCS as a result of oxidative degradation of the absorbing solvent.[107-111] NH_3 is a pollutant with undesirable chemical

effects in the atmosphere,[112] where large levels can promote interesting aerosol chemistry.[113] For example, the presence of NH_3 above background levels can change nitrate aerosol chemistry.[114] Therefore, accurately measuring the emissions of NH_3(g) from reported sources is of significant importance.

Herein, we quantify NH_3(*g*) emissions from a small pilot-scale CCS with a coal-fired flue gas generator using a 5 M (30.0 wt.%) monoethanolamine (MEA) solvent. For this study, we used the UKySonde, a small unmanned aerial system (sUAS)[88] equipped with a calibrated NH_3(*g*) sensor,[89] along with standard gas emission sampling methodology for comparison.

3.2 Experimental

3.2.1 CO_2 Capture System

UKy-CAER built and operates a bench scale 0.1-megawatt thermal (MWth) CO_2 capture system using a coal burning flue gas generator (FGG) to provide representative coal derived flue gas to the CCS (10-14% CO_2, 8-10% O_2, other trace gases, and balanced with N_2). The UKy-CAER CSS is typically operated during normal working hours in a manner to replicate extreme operation conditions (eg. high temperatures and contaminate levels) to accelerate solvent degradation and get meaningful data from a short operational number of hours. The produced flue gas is transported to the building housing the CCS in the left-hand side of Figure 3.1A, where a 30.0 wt. % MEA solvent (in water) is used in a typical aqueous amine-based CCS absorber/regeneration configuration (Figure 3.1B) to separate the CO_2 from the flue gas. Finally, the treated flue gas is released out of a stack (0.194 m diameter), which is in the center of the yellow circle in Figure 3.1A, which also shows that the surrounding roof is highly reflective. Overall, the high altitude reading does

not affect the number measured at the bottom of the flight that is the key to model the point source. The scrubbed flue gas typically contains > 2% CO_2, along with NH_3(g) from degradation of the amine solvent. The $NH_3(g)$ concentration is solvent and regeneration temperature dependent. The total emissions from this CCS are relatively small and well below thresholds considered insignificant from an air permitting perspective.[115] $NH_3(g)$ emissions in the scrubbed flue gas were quantified using an sUAS (Figure 3.1C), with comparison emission values collected using a standard methodology based on EPA CTM-027.[107, 115] The experiments with the sUAS took place between September 10 and 14, 2018, above the stack exhaust. Measurements of background $NH_3(g)$ mixing ratio (the molecular ratio of methane to air in a unit volume)[116] were completed at the ground level (away from the coal burning FGG and CCS) on September 10. $NH_3(g)$ profiles with altitude were registered from September 11 to 14, 2018. The bench facility was fully operational on September 10, 11, and 13, 2018. Typical daily averages of $NH_3(g)$ emissions are also reported based on emission sampling using a standard stack sampling method. The standard method was used to compare the sUAS measurements and demonstrate the ability of the sUAS to replace conventional measurement techniques.

Figure 3.1 (a) Aerial view of the facilities employed in the University of Kentucky Center for Applied Energy (UKy-CAER). The coal flue gas generator is located to the right- side and the gas flows through a PVC pipe (from right to left) to the building on the left-hand side for amine treatment in the carbon capture system (CCS) before the scrubbed flue gas emissions are released out the stack at the top (yellow dashed circle). (b) Image of the amine-based CCS at UKy-CAER. (c) Perspective view of the sUAS flying above the stack.

3.2.2 Quantification of $NH_3(g)$ with the UKySonde

The sUAS, called the UKySonde, integrated an analytical sensor (MICS-6814 sensor) to measure the mixing ratio of NH_3 with a 3DR Solo quadcopter used to fly vertical profiles above 1 m from the stack (from 20 to 140 m above ground level, AGL). The sensor was calibrated in a custom environmental chamber using standards from 5.00 ppbv to 90.00 ppmv as described previously.[89] Along with an expansive operating range, the sensor is accurate within ± 0.20% of the measured value with a precision of 30 ppbv. Programed flights with Mission Planner Autopilot software were used to monitor $NH_3(g)$ levels at a rate of 1 Hz during the continuous operation every ~1 h from 9 am to 4 pm (UTC-5). The flights were designed to measure $NH_3(g)$ directly above the exhaust from the stack, corresponding to the maximum mixing ratio in the flue gas after the CCS. In addition, profiles recorded $NH_3(g)$ levels up to 120 m above the stack. The Grubbs test

was conducted and determined no outliers at the 95% confidence level from the average mixing ratio reported for each flight from 1 to 2 m above the stack (Table 3.2, Section 3.1: Supporting Information).[117] The mixing ratios of NH_3 reported below correspond only to the ascent profiles corrected after subtracting the average background measured when the fired furnace (located ~60 m downwind) was not operating.

3.2.3 Conventional Ammonia Emission Sampling

Closely following U.S.A. EPA CTM-027 method, samples of flue gas were withdrawn from the CCS exit stack into a 0.05 M solution of sulfuric acid (VWR, Wayne, PA) in an impinger train. The collected samples were analyzed by Ion Chromatography and the concentration of ammonia in the flue gas was calculated in ppbv.[115]

3.2.4 Emission Estimates of $NH_3(g)$

The mixing ratio of NH_3, in ppbv units, measured immediately above the stack were integrated over time and combined with the flow rate of the treated flue gas at the exhaust of ~14.7 actual cubic feet per minute (acfm) to obtain the mass flow of emissions with the industry standard of pounds of NH_3 per day (lbs day^{-1}). The average mass flow measured for each flight from 1 to 2 m above the stack was fed into a Gaussian plume model to retrieve the mixing ratio inside the stack prior to diffusion. For this model, the atmospheric conditions were neutral, and the exit velocity and temperature of the flue gas were 0.232 m sec^{-1} and 40 °C, respectively (Table 3.2). Specific wind inputs for each flight were provided by the nearest weather station (KKYGEORG28) at Horse Country, ~3.2 km away.[118]

3.3 Results and Discussion

The UKySonde flew profiles every ~1 h during 8 h from September 11 to 14, 2018, measuring $NH_3(g)$ levels from the flue gas after treatment with MEA in the CCS on September 11 and 13, and background levels (with the furnace off) on September 12 and 14. The $NH_3(g)$ mixing ratio attributed to the UKy-CAER CCS can be retrieved from the average mixing ratio of NH_3 measured in close proximity to the stack throughout the day. The measurement of $NH_3(g)$ in the flue gas using the standard stack sampling method took place under generally the same CCS operating conditions, but not in parallel with sUAS sampling. Daily averages of $NH_3(g)$ emissions were quantified and used to compare with the sUAS measurements.

3.3.1 UKySonde Ammonia Measurements

The background mixing ratio determined between 12 and 4 pm on September 10th, was 7.26 (± 0.35) ppbv. Figure 3.2 shows the measurements of $NH_3(g)$ from ascent profiles on September 11, which took place every ~ 1 h. The average mixing ratio of NH_3 1 m above the stack was 2.89 (± 0.76) × 10^4 ppbv, which corresponds to 8.03 (± 1.01) × 10^4 ppbv in the stack as retrieved with the Gaussian plume model. Similarly, during September 13 (Figure 3.7, Section 3.4: Supporting Information), the average 2.67 (± 0.88) × 10^4 ppbv $NH_3(g)$ indicates there was 8.20 (± 1.33) × 10^4 ppbv in the stack. On September 12 and 14, the CCS was not operational, and measured a background mixing ratio 1 m above the stack was 6.93 (± 2.28) and 6.95 (± 1.57) ppbv $NH_3(g)$, respectively. Table 3.1 summarizes all UKySonde measurements throughout the week.

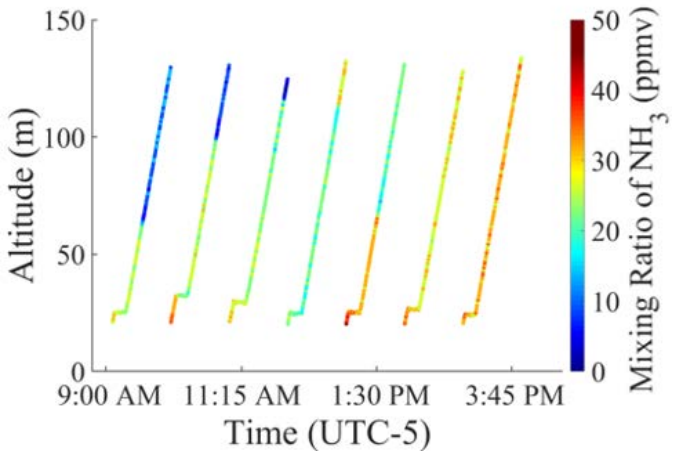

Figure 3.2 Vertical profiles flown by the UKySonde to measure the mixing ratio of $NH_3(g)$ in the exhaust (color-bar to the right) above the UKy-CAER stack from 20-140 m above ground level.

Table 3.1 Experiments and Controls for the Determination of NH_3(g) with the UKySonde

Date	**CCS Status**	**sUAS Flying**	**Mixing Ratio of NH_3 (ppbv)**	**$NH_3(g)$ Emission (lbs day^{-1})**
9/10/2018	On	No	7.26 (± 0.35)[a]	-
9/11/2018	On	Yes	8.03 (± 1.01) × 10^4	7.20 (± 0.93) × 10^{-3}
9/12/2018	Off	Yes	6.93 (± 2.28)[b]	-
9/13/2018	On	Yes	8.20 (± 1.33) × 10^4	7.55 (± 1.23) × 10^{-3}
9/14/2018	Off	Yes	6.95 (± 1.57)[b]	-

[a]ground level background during power generation, [b]background over the stack when the Carbon Capture System (CCS) is not operating

3.3.2 Conventional Ammonia Measurements

Typical $NH_3(g)$ content in the exhaust from the CCS was quantified by conventional emission sampling and ranged between 1.19 × 10^4 and 1.20 × 10^5 ppbv, with an average from 7 measurements of 8.44 (± 1.80) × 10^4 ppbv.

3.3.3 Comparison of $NH_3(g)$ Emissions Measurement Techniques

The mixing ratio of NH_3 was measured with two independent analytical methods, providing quality assurance of the similar $NH_3(g)$ emission reported by the UKySonde and

the standard stack sampling method during operation of the CCS. The combined sUAS method with the Gaussian plume model determined an average NH_3 mixing ratio of 8.12 ($\pm$ 4.03) $\times 10^4$ ppbv in the flue gas, while conventional gas sampling measured an average of 8.44 ($\pm$ 1.80) $\times 10^4$ ppbv. Both values agreed reasonably well within the experimental errors expected from two different analytical techniques. These measured values are also in the same ballpark as published ammonia emission values from MEA testing campaigns at other CCS units of variable size and flue gas composition.[115] The overlapping result of emission estimates from traditional sampling methods and the sUAS further validates their use in quantifying industrial point source pollution. The work demonstrates that the integration of sUAS into routine emission sampling can provide accurate, real-time results and are a valid replacement for wet-lab techniques.

Currently, the total annual $NH_3(g)$ emissions in the U.S.A. is 3.0 ($\times$ 0.2) Tg year^{-1}, with a 70-80% attributed to agriculture (e.g., fertilizer and manure), and the remaining 20-30% originating from industry and other anthropogenic sources.[119] Having the ability to quickly measure $NH_3(g)$ emission from a point source, such as this amine-based CCS, has broad implications and potential application of this technique. The ability to record essentially real time emission data is of significant interest to utility and industrial locations, in addition to regulatory agencies. To expand upon this work and determine the full environmental impact of the plume, a horizontal flight pattern complete with in-situ measurements should be employed. This enables the characterization of the plume as it traverses the boundary layer and atmospherically ages.

Overall, this work demonstrates that $NH_3(g)$ emissions can be estimated with confidence using sUAS and are a viable option to replace existing sampling methods and can also serve to validate and improve real-time weather models.2

3.4 Supporting Information

3.4.1 Additional Details of the Gaussian Plume

The average mixing ratio measured for each flight from 1 to 2 m above the stack was fed into a Gaussian plume model to retrieve the mixing ratio inside the stack prior to diffusion. The Gaussian Plume model was chosen to estimate the concentration inside the stack based on measurements taken by the sUAS 1-2 m above the stack.[120-123] The model was chosen due to its proven performance over small distances. This model has been used on small scales on many occasions and successfully modeled the dispersion of gas molecules.[124-126] The model has serious limitations for pollutants that undergo chemical transformations and depends heavily on the steady state meterological conditions. This means the model is typically not good for long term pollutant evaluations of $NH_3(g)$ over great distances or periods of time. Because the application of the model to the expriement is on such a small scale, many of the limitations associated with the model are mitigated. The amount of flue gas diffusion occurring between the stack and the sUAS $NH_3(g)$ sensor is dependent on many factors. The emission rate, distance from source, and atmospheric conditions influence plume characteristics. The most significant atmospheric conditions considered are wind speed, wind direction, and boundary layer stability. The Gaussian plume model incorporates these parameters to analytically solve the diffusion between the source and the measurement by the UKySonde. The uncertainty of the $NH_3(g)$ emission estimate is propagated through the sUAS measurements and carried into the inputs of the

model (where applicable). The total measurements error is conserved in the final output through typical error propagation methods and the final output of the model encompasses the total uncertainty of the combined method. The most significant source of uncertainty that is introduced through the plume model comes from the variance in wind speed, which obviously effects the behavior of the plume dispersion. Small changes in the wind speed parameter effected the model output more than any factor. However, several assumptions are made about the atmospheric conditions during the experiments that help mitigate this. The Gaussian plume model makes the following five assumptions: (1) Continuous emission, negligible background pollution; (2) chemical stability, mass conservation after surface contact, negligible deposition; (3) steady state conditions, negligible change in wind speed/direction with time and altitude; (4) dispersion parameters are a function of horizontal distance, negligible diffusion in direction of travel; and (5) geography does not alter plume. The Gaussian dispersion equation can be written as:

$$q_e = \frac{Fe}{2\pi\sigma_y\sigma_z} \exp\left(\frac{-(y)^2)}{2\sigma_y^2}\right) \exp\left(\frac{-(z-h)^2)}{2\sigma_z^2}\right) + \exp\left(\frac{-(z+h)^2)}{2\sigma_z^2}\right) \qquad Equation\ 3.1$$

The modeled flux estimate, q_e is the result of Equation 3.1. The flux estimate depends mainly on the initial flux estimates, Fe, derived from the sUAS measurements and CCS flow rates and the dispersion coefficients, σ (in the respective directions y and z), which define the spread of the plume. In this model, 67% of the plume falls within ±σ, as with any normal distribution. The magnitude of σ is dependent on atmospheric turbulence. Larger eddies yield unstable atmospheric conditions and will be represented with a larger σ. Stable atmospheric conditions are fit with smaller σ values. The horizontal diffusion coefficient, σy, is largely dependent on the wind speed and direction. Strong crosswinds

yield larger σy values. The vertical diffusion coefficient, σz, is largely dependent on temperature gradient of the boundary layer. Temperature inversions (stable atmospheric conditions) dampen diffusion and result in smaller σz values. The horizontal distance from the source, perpendicular to the wind direction, is represented in the y direction. The horizontal distance parallel to the wind direction, is represented in the x direction. The vertical distance from the source, relative to the source height, is represented in the z direction.

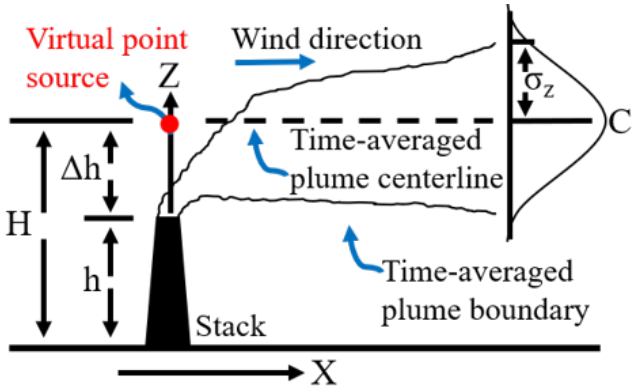

Figure 3.3 Visual description of the Gaussian plume model utilized in this manuscript to determine the mixing ratio of $NH_3(g)$ in the stack before diffusion.

Table 3.2 shows the parameters used in the model for each flight. As an example of the data treatment for the first flight, the model ran with atmospheric conditions that were neutral, and the exit velocity and temperature of the flue gas were 0.232 m sec^{-1} and 40 °C, respectively. The stack diameter was 0.194 m. Specific wind inputs and ambient air temperatures for each flight were provided by the nearest weather station (KKYGEORG28) at Horse Country, ~3.2 km away. The wind speed for the day was consistently at 7 mph NE, with temperatures between 20.0 and 21.7 °C (Table 3.2). From these inputs, the σ_y and σ_z were calculated. The Gaussian Plume model was run as a function of distance from the stack (0 to 120 m).

Table 3.2 Measured Model Inputs for the Determination of $NH_3(g)$ with the UKySonde

Date	CCS	Flight #	Input NH_3 (mg/s)	Stack Radius (m)	Exit Gas Velocity (m/s)	Exit Gas Temp (°C)	Air Temp (°C)	Wind Speed (m/s)
9/11/2018	On	1	0.667	0.097	0.232	40	20.0	3.1
		2	0.877				20.0	3.1
		3	0.746				20.6	3.1
		4	0.552				21.1	2.7
		5	0.884				21.7	3.1
		6	0.863				21.7	3.1
		7	0.796				20.6	3.1
9/13/2018	On	1	0.247	0.097	0.232	40	28.9	1.0
		2	0.878				30.0	1.0
		3	0.230				31.1	1.3
		4	0.552				31.1	3.6
		5	0.326				31.1	1.0
		6	0.132				31.1	2.7
		7	0.290				29.4	2.7
		8	0.118				26.7	2.2

The UKySonde collected 27 profiles measuring $NH_3(g)$ mixing ratios up to 120 m above the CCS. The flights were designed to measure $NH_3(g)$ 1-2 m above the exhaust from the stack, corresponding to the maximum mixing ratio in the flue gas after the CCS. The mixing ratios of NH_3 reported below (Table 3.3) correspond only to the ascent profiles.

The figures for the background measurements on the ground (3.4), and background profiles (3.5, 3.6), and the second data flight (3.7) are included below.

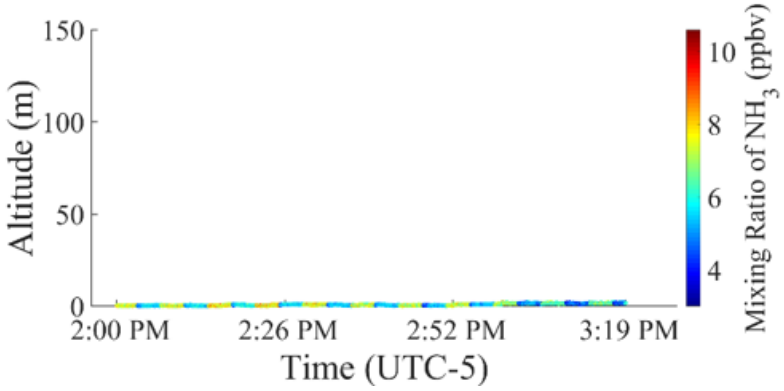

Figure 3.4 Ground level measurements collected on September 10, 2018 by the UKySonde to measure the mixing ratio of $NH_3(g)$ (color-bar to the right) 60 m upwind of UKy-CAER smokestack.

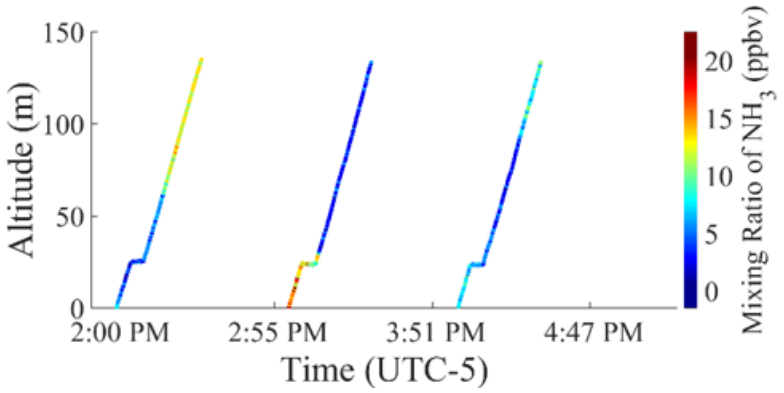

Figure 3.5 Vertical profiles flown on September 12, 2018 by the UKySonde to measure the mixing ratio of $NH_3(g)$ (color-bar to the right) above the UKy-CAER smokestack from 20-140 m above ground level while the stack was not operational.

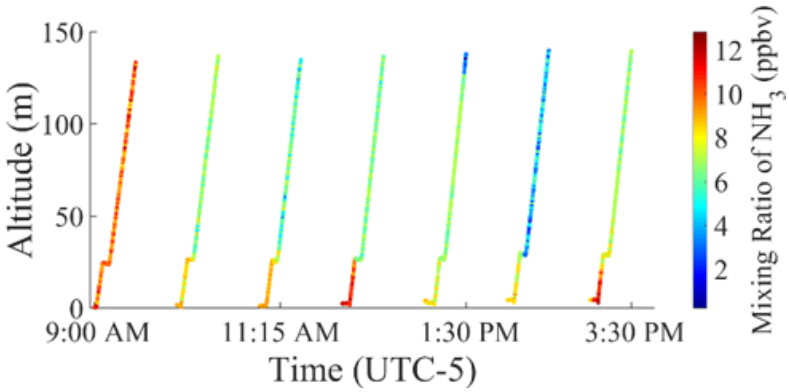

Figure 3.6 Vertical profiles flown on September 13, 2018 by the UKySonde to measure the mixing ratio of $NH_3(g)$ (color-bar to the right) above the UKy-CAER smokestack from 20-140 m above ground level while the stack was not operational.

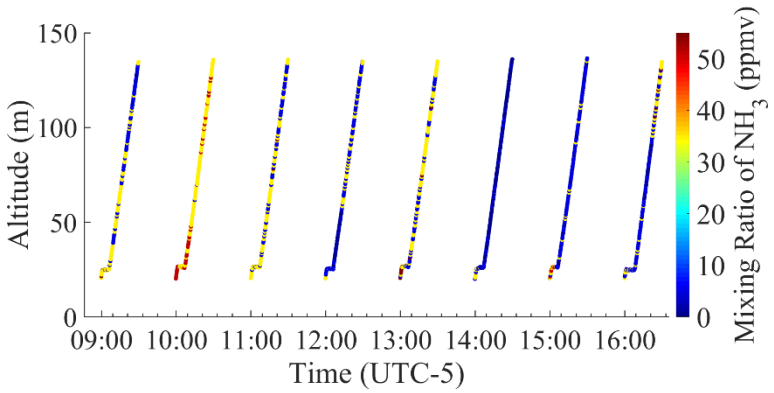

Figure 3.7 Vertical profiles flown on September 14, 2018 by the UKySonde to measure the mixing ratio of $NH_3(g)$ in the exhaust (color-bar to the right) above the UKy-CAER smokestack from 20-140 m above ground level.

Table 3.3 Measured and Modeled Mixing Ratios of $NH_3(g)$ for Emission Estimates

Date	CCS	Flight #	Mixing Ratio of $NH_3(g)$ (ppmv)	Model Output $NH_3(g)$ (ppmv)	$NH_3(g)$ Emission (lbs day^{-1})
9/11/2018	On	1	26.28 (± 2.40)	68	$6.27 (\pm 0.59) \times 10^{-3}$
		2	34.54 (± 1.43)	90	$8.29 (\pm 0.35) \times 10^{-3}$
		3	29.38 (± 2.81)	77	$7.10 (\pm 0.69) \times 10^{-3}$
		4	21.73 (± 2.58)	65	$5.99 (\pm 0.63) \times 10^{-3}$
		5	34.82 (± 4.07)	91	$8.39 (\pm 1.00) \times 10^{-3}$
		6	33.96 (± 1.81)	89	$8.20 (\pm 0.44) \times 10^{-3}$
		7	31.34 (± 3.97)	82	$7.56 (\pm 0.97) \times 10^{-3}$
9/12/2018	Off	1	$9.86 \pm (1.83) \times 10^{-3}$ [b]	-	-
		2	$3.41 \pm (1.18) \times 10^{-3}$ [b]	-	-
		3	$5.13 \pm (1.27) \times 10^{-3}$ [b]	-	-
9/13/2018	On	1	34.09 (± 5.50)	105	$9.66 (\pm 0.31) \times 10^{-3}$
		2	77.50 (± 6.94)	238	$2.19 (\pm 0.39) \times 10^{-3}$
		3	31.67 (± 5.00)	75	$6.90 (\pm 0.28) \times 10^{-3}$
		4	8.53 (± 4.91)	10	$0.92 (\pm 0.27) \times 10^{-3}$
		5	45.00 (± 9.57)	138	$12.69 (\pm 0.55) \times 10^{-3}$
		6	18.18 (± 7.89)	21	$1.93 (\pm 0.44) \times 10^{-3}$
		7	40.00 (± 12.08)	46	$4.23 (\pm 0.67) \times 10^{-3}$
		8	16.28 (± 7.71)	23	$2.12 (\pm 0.43) \times 10^{-3}$
9/14/2018	Off	1	9.83 ± (0.43) ×10-3 [b]	-	-
		2	$7.02 \pm (0.51) \times 10^{-3}$ [b]	-	-
		3	$6.07 \pm (0.52) \times 10^{-3}$ [b]	-	-
		4	$6.53 \pm (0.41) \times 10^{-3}$ [b]	-	-
		5	6.44 ± (0.55) × 10-3 [b]	-	-
		6	4.59 ± (0.73) × 10-3 [b]	-	-
		7	7.02 ± (0.35) × 10-3 [b]	-	-

CHAPTER 4. FLUX MEASUREMENTS AND EMISSION RATE ESTIMATES OF FUGITIVE TRACE GASES VIA SMALL UNMANNED AERIAL SYSTEMS AND DISPERSION MODELING

Reproduced with permission from:

Travis J. Schuyler, Sean C.C. Bailey, and Marcelo I. Guzman.

In Preparation

4.1 Introduction

Recent measurements of fugitive methane gas ($CH_4(g)$) emissions determined a leak rate of 2.3% (of the gross U.S. natural gas production).[127] The bottom up emission estimates of these measurements (13±2 Tg $CH_4(g)$ yr^{-1}) exceeded EPA greenhouse gas inventory estimates by ~60%.[127] Methane is one of four major compounds contributing to radiative forcing in the troposphere and is 84 times more potent than carbon dioxide (CO_2) over a 20 year period as a greenhouse gas (GHG).[128] $CH_4(g)$ facilitates the atmospheric transport of water vapor to the stratosphere and photochemically reacts with ozone (O_3) and nitrogen oxide (NO_x).[128] About 90% of the $CH_4(g)$ lost in the atmosphere is due to oxidation by hydroxyl radicals ($^{\cdot}OH$), resulting in complex atmospheric aging.[129-131] Volcanoes also change the composition, and radiative forcing, of the atmosphere via eruptions of trace gases and particulate matter. Volcanic eruptions (i.e. Hawaiian Volcano Kilauea, 2018)[132] release large quantities of toxic hydrogen sulfide ($H_2S(g)$) and sulfur

dioxide ($SO_2(g)$), creating an environmental and public health risk.[4, 133-137] Currently, in-situ measurements of volcanic plumes are a dangerous and difficult task that employ expensive instrumentation.[138] The development of methodologies to improve fugitive emission inventories is motivated by the limitations of current sampling techniques.[139]

Small unmanned aerial systems (sUAS) are useful scientific tools for measuring meteorological conditions and trace gas mixing ratios in the atmospheric boundary layer (ABL).[88] The ability for the sUAS to be transported easily and deployed quickly for various applications of atmospheric measurements makes them advantageous for impromptu field work. Furthermore, the sUAS platform provides spatiotemporal data on the order of meters and seconds, an information density that cannot be matched by current methods <100 m above ground level (AGL).[88] The argument that the sUAS is a useful analytical tool is strengthened by the recent and on-going work in the field. The calibration and validation of 23 temperature, pressure, and relative humidity (PTH) sensors onboard 38 sUAS elucidated the bias of solar radiation and sensor aspiration and improved sensor accuracy.[87] Meteorological measurements collected by sUAS have characterized boundary layer transitions,[140] detected turbulent anomalies induced by wind turbine blades,[141] and validated weather research and forecasting (WRF) models.[142] Deploying sUAS, in combination with ground-based weather instruments, has also successfully predicted Lagrangian coherent structures.[143] The previous work provides evidence that in-situ wind and PTH measurements with sUAS could facilitate the determination of in-situ turbulent diffusion statistics for improved dispersion modeling.[144] Advancing sUAS capabilities for the determination of turbulent statistics in the ABL expands its applications for trace gas measurements. Preliminary studies of methane plume detection with sUAS used an open

path mid-infrared sensor employing wavelength modulation spectroscopy.[145] However, the sUAS could not calculate turbulent statistics, or fluxes, from in-situ wind measurements for emission leak rate estimates via dispersion modeling. Another study integrated a custom methane spectrometer on board a fixed wing unmanned aerial vehicle (UAV) to measure biogenic methane emissions. However, the platform also did not measure wind velocity in-situ and could not realize the superior sampling patterns of rotary wing UAVs, therefore limiting the analysis of the results.[146] A remote methane leak detecting UAV was recently developed and measured small natural gas leaks, but discovered large errors (100%) due to noise in global positioning system (GPS) measurements.[147] The research also did not incorporate the sensors required to determine the turbulent statistics for dispersion modeling from in-situ measurements. The previous work demonstrates the limitations of the data analysis without in-situ wind measurements and motivates future studies of fugitive gases that deploy sUAS with ultrasonic anemometers for adequate measurements to determine turbulent diffusivity in-situ for dispersion modeling.

This research proposes new methods to supplement current sampling techniques with sUAS measurements of trace gas fluxes. The inclusion of sUAS measurements aims to provide unequivocal spatiotemporal resolution while mitigating sampling risk. The integration of sUAS measurements to improve fugitive gas emission estimations is accomplished through coincident, in-situ measurements of trace gas mixing ratios, PTH, and 3D wind velocity (U, V, W).

Herein, a sUAS integrated with ultrasonic anemometers, meteorological sensors, and two different methane instruments is used to detect, characterize, and quantify the fluxes of a small point source methane leak. The mixing ratios collected by the UKySonde $CH_4(g)$

sensor are validated with a commercially available $CH_4(g)$ mid-infrared laser spectrometer and the suitability of the UKySonde sensor for fugitive gas flux measurements is analyzed. A dispersion model, parameterized by turbulent statistics calculated from sUAS meteorological measurements, estimates the methane fluxes and leak rates. The modeled methane fluxes and leak rate estimates are compared to the measurement techniques and future improvements to the model are discussed. Furthermore, a similar trace gas sensor package demonstrates the potential of the sUAS measurements and dispersion modeling method to characterize $H_2S(g)$ and $SO_2(g)$ in volcanic plumes. The performances of the $H_2S(g)$ and $SO_2(g)$ sensors are evaluated in the context of the future application.

4.2 Experimental

4.2.1 Materials

The UAV deployed was a s1000 octocopter (DJI, Shenzhen, Guangdong, China). The s1000 was powered by a 6S 22 Ah battery (Tattu, Dublin, CA, USA) with a total takeoff weight of 12 kg and flight time of 10 min. A Pixhawk (3DRobotics, Berkeley, CA, USA) autopilot was programmed with the open source Mission Planner ground station software (ArduPilot) for precise flight plans. The autopilot was optimized to upload waypoints defined by latitude, longitude, and altitude. The Pixhawk was connected to Mission Planner via a 900 MHz telemetry radio link and the mission was uploaded to the sUAS before takeoff, ensuring the flight plan was completed even if connection was lost to the ground station. The autopilot records GPS and velocities that are extracted after each flight for data integration. The s1000 payload included an ultrasonic anemometer above the airframe, two ultrasonic anemometers extended horizontally from the airframe, the UKySonde $CH_4(g)$ sensor, a Pico $CH_4(g)$ laser spectrometer, and meteorological sensors

(Figure 4.1). The system collectively provided measurements of time, GPS, wind velocity, two independent methane gas mixing ratios, and PTH.

Figure 4.1 DJI s1000 sUAS equipped with three ultrasonic anemometers, two methane sensors, and PTH sensors.

4.2.1.1 Trace Gas Measurements

All measurements of trace gases were sampled from a pumped system using a Teflon tube fixed outside of the s1000 rotors via a carbon fiber rod (Figure 4.1). The pumped system created a measurement lag time of 4 seconds that was corrected in the data analysis. The sampling always took place into the wind to minimize the air disturbed.

4.2.1.1.1 UKySonde $CH_4(g)$ Sensor

The UKySonde is a custom sensor package developed at the University of Kentucky. The core of the package was comprised of a microcontroller (UNO, Arduino, Somerville, MA, USA) with a base shield (V2, SEEED Studio, Shenzhen, Guangdong, China), a wireless SD shield (Arduino), and a 16-bit analog to digital converter (ADC) shield (LTC1859, Mayhew Labs, Indianapolis, IN, USA). The UKySonde, previously described in detail, measured and logged PTH and mixing ratios of $CH_4(g)$ at 1 Hz.[148] The $CH_4(g)$

sensor had an accuracy of ±1.24% of the measured value, with a precision of ±180 ppbv and a resolution of 10 ppbv.

4.2.1.1.2 PICO $CH_4(G)$ SPECTROMETER

A Pico Mobile Leak Detection System (Aeris, Hayward, CA, USA) was mounted underneath the s1000. The mid-infrared laser absorption spectrometer was powered by an integrated battery and measured $CH_4(g)$ with a precision of ±0.5 ppb, and a resolution of <500 ppt. $CH_4(g)$ mixing ratios were transmitted at 1 Hz, via a WiFi connection, to a designated ground station tablet running custom software (Qt Creator, The Qt Company, Helsinki, FI). The data was stored locally to an SD card (Class 10, 32GB, SanDisk, Milpitas, CA, USA) for extraction after the flight. The system also had an independent GPS system (NEO-8M, ublox, Horgen, Zurich, Switzerland) that allowed for redundant sensor alignment.

4.2.1.1.3 $H_2S(G)$ AND $SO_2(G)$ SENSOR PACKAGE

An alternative application of this experimental design replaces the UKySonde $CH_4(g)$ sensor and Pico $CH_4(g)$ spectrometer with sensors for detecting volcanic emissions. A sensor package was assembled to measure atmospheric mixing ratios of $H_2S(g)$ and $SO_2(g)$ integrated with PTH and GPS. The H_2S-A4 and SO_2-A4 electrochemical gas sensors (Alpha Sense, Great Notley, Essex, UK) were integrated into the analog front end (AFE) sensor board (Alpha Sense) and sampled with 16-bit ADC (Mayhew Labs). The $H_2S(g)$ and $SO_2(g)$ sensors had an accuracy of ±5 and ±15 ppb, a resolution of 0.75 and 1.50 ppb, and effective linear ranges of 1 ppb – 50 ppm and 5 ppb – 100 ppm respectively. The GPS, PTH, $H_2S(g)$ and $SO_2(g)$ measurements were synchronized and streamed to custom ground station software (Qt Creator) with 2.4 GHz

radio telemetry (Xbee 3 Pro Zigbee 3.0, Digi, Hopkins, MN, USA). The data was logged at 5 Hz internally to an SD card (Class 10, 32GB, SanDisk), and at the ground station, to ensure measurements were collected for analysis.

4.2.1.2 sUAS Wind Velocity Measurements

Three ultrasonic anemometers, one above the airframe and two extending horizontally from the airframe measured U, V, W. All three ultrasonic anemometers used the flight battery (Tattu) for power and transmitted data via RS-232 to a Slerj box. The data was recovered from the SD card (Class 10, 32GB, SanDisk) after the flights. The anemometer data was aligned in time and confirmed with pressure correlation.

4.2.1.2.1 R.M. YOUNG MODEL 8100

An ultrasonic anemometer (Model 8100 R.M. Young, Traverse City, MI, USA) was mounted above the s1000 to provide in-situ measurements of wind velocity. The Model 8100 is a 3-axis sensor that provided U, V, W measurements up to 40 m sec^{-1} with an accuracy of ±0.05 m sec^{-1} and a resolution of 0.01 m sec^{-1}. The directional component was provided for 360° with an accuracy of ±2° and a resolution of 0.1°. The voltage outputs correspond to U, V, and W.

4.2.1.2.2 TRISONICA MINI WEATHER SENSORS

Two ultrasonic anemometers (TriSonica Mini Weather Sensors, Anemoment, Longmont, CO, USA) were attached in-plane with the s1000, but outside of the rotors. The TriSonica Mini Weather Sensor is also a 3-axis sensor that provided U, V, W up to 30 m sec^{-1}, with an accuracy of ±0.5 m sec^{-1} for low wind speeds, ±2% for high wind speeds,

and a resolution of 0.1 m sec^{-1}. The directional component was also 360° with an accuracy of ±1.0° and a resolution of 1.0°.

4.2.1.3 PTH Measurements

Triplicate meteorological sensors were integrated into the sUAS. All temperature and relative humidity (RH) sensors were secured underneath of, and one-quarter the propeller length from, the tip of the rotor to minimally impact the disturbance of the airflow.[149]

4.2.1.3.1 BME280

The integrated PTH measurements for the UKySonde sensor package were taken with the BME280 sensor (Bosch Sensortec, Sunnyvale, CA, USA). The BME280 temperature sensor had an accuracy of ±1.0 °C and a precision of 0.005 °C, with a response time of 0.5 s to 66% full signal. The RH sensor had an accuracy of ±3% RH, with a precision of ±2% RH and a response time of 1 s to 63% full signal.

4.2.1.3.2 iMET-XQ2

An iMET-XQ2 sensor (InterMet Systems Inc., Grand Rapids, MI, USA) measured the meteorological conditions. The stand-alone sensor provided measurements of PTH and GPS utilizing a built-in battery. The temperature sensors had an accuracy of ±0.3 °C with a resolution of 0.1 °C. The RH sensor had an accuracy of ±5% RH and a resolution of 0.7% RH. The sensor logged internally at 1 Hz and the data was recovered, via the InterMet Systems software after the flight, and aligned using correlations of GPS position, pressure, and time.

4.2.1.3.3 iMET-XF

For the $H_2S(g)$ and $SO_2(g)$ sensor package, integrated PTH measurements were collected with an iMET-XF (InterMet Systems Inc). The iMET-XF temperature sensors had an accuracy of ±0.15 °C and a resolution of 0.01 °C. The RH sensors had an accuracy of ±1.8% and a resolution of 0.03%. The PTH data was sampled at 5 Hz and stored locally to an SD card (Class 10, 32GB, SanDisk) and transmitted in real time to the custom ground station software (Qt Creator) via a 2.4 GHz radio telemetry signal (Xbee).

4.2.2 Methods

4.2.2.1 Detection of Fugitive $CH_4(g)$

The experiments that measured and modeled fluxes from a controlled $CH_4(g)$ release took place on February 3rd, 11th, and 27th, 2020 under Federal Aviation Authority (FAA) Part 107 regulations at the University of Kentucky Agronomy Farm in Lexington, KY (38° 07' N, 84° 30' W, 280 m above sea level, Figure 4.2a). $CH_4(g)$ was released from a compressed gas cylinder (99.99% analyzed ultra-high purity, Scott Gross, Lexington, KY, USA) at 6.17×10^{-5} m^3 sec^{-1} (at 16.0 PSI) 1.0 m AGL, simulating an anthropogenic methane gas leak (e.g. pipeline leak). The leak rate was controlled with a certified, calibrated mass flow controller (Model GM50A, 0-1000 sccm, MKS Instruments, Andover, MA, USA). The diameter of the leak orifice was 4.00 mm and the mass flow rate, calculated from the volumetric flow rate, was 41.16 mg sec^{-1} $CH_4(g)$ for all gas releases. The gas cylinder was positioned directly upwind of the perpendicular sUAS flight path (Figure 4.2b) for the reported measurements. A total of three experiments, and nine total coordinated flights/gas releases, were completed to validate the UKySonde methane

sensor with the Pico laser spectrometer and evaluate the dispersion model. Each flight consisted of 4 raster scan profiles (approximately 40 m in length), ascending by 2 m each scan from 2-6 m AGL. The flights were consecutive to minimize the change in meteorological conditions.

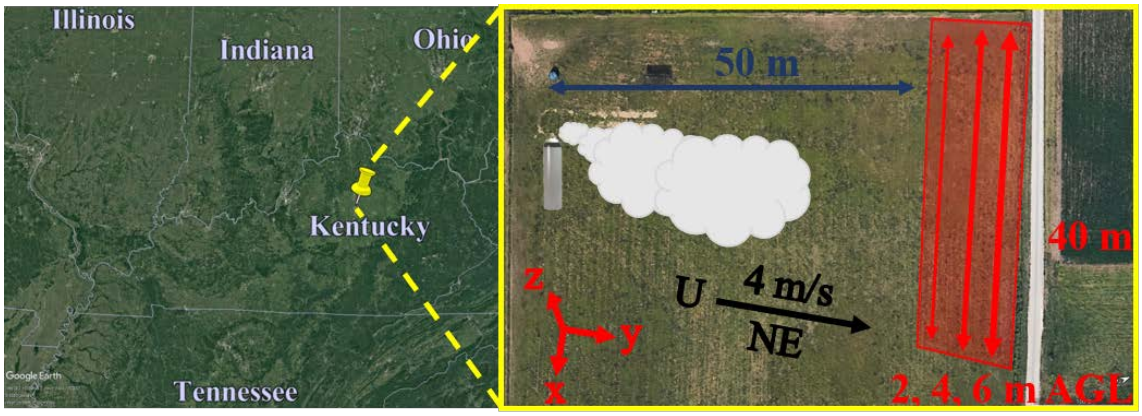

Figure 4.2 (**a**) A regional map indicating the flight location with a yellow pin. (**b**) Overview of $CH_4(g)$ releases illustrating the sUAS xz flight pattern 50 m downwind of, and perpendicular to, the source of the leak. For each flight, the sUAS repeated four, 40 m horizontal profiles at 2, 4, and 6 m above ground level.

4.2.2.2 $H_2S(g)$ and $SO_2(g)$ Proof-of-Concept Measurements

The proof-of-concept flights for volcanic plume measurements took place on March 5th, 2020 at the University of Kentucky Agronomy Farm in Lexington, KY under FAA Part 107 regulations. The flight pattern for the experiment was a series of stacked 100 m loiter circles, ascending by 10 m for each loiter. The origin of the loiter circle represented the crater of the volcano, allowing pollutant mixing ratios to be determined at a series of altitudes in and out of the plume.[150]

4.2.2.3 Dispersion Model for Flux and Leak Rate Estimates of Fugitive Gases

The scalar transport equation was used to model the plume and estimate the leak rate. Supported by the experimental design, a continuous, steady state, point source release of

methane gas was modeled with Equation 4.1.[151] The incorporation of in-situ wind and meteorological measurements enabled the calculations of the mean wind speed ($\bar{U}$), the standard deviation of U (σ_u), the variance of U (‹U›), the eddy orbital velocity (u_*), and boundary layer height (Z). These parameters were used to determine the Lagrangian integral timescale (T_L).[152-154]

$$C(x, y, z) = \frac{\dot{m}}{4\pi\gamma r} e^{\frac{-\bar{U}\,(r-y)}{2\gamma}} \qquad Equation\ 4.1$$

The result of Equation 4.1, C(*x*, *y*, *z*), was the concentration of methane (mg m^{-3}) at a specified 3D position. The product of ‹U› and T_L is the turbulent diffusivity, γ (m^2 sec^{-1}). γ described the degree of atmospheric transport for dispersion modeling and was determined by in-situ sUAS measurements.[151, 152, 155, 156] The mass flow rate of methane gas, ṁ (mg sec^{-1}), was calculated from the measured MFC flow rate. The distance from the release origin, *r*, was calculated based on the *x*, *y*, and *z* positions converted from GPS measurements of latitude, longitude, and altitude respectively. $\bar{U}$, *r*, and *y* measurements were aligned spatiotemporally for all C(*x*, *y*, *z*) values modeled for each gas release. C(*x*, *y*, *z*) was interpolated over the xz plane (Figure 4.2b, shaded red) for direct comparison to the measured values. Equation 4.1 was also solved for ṁ to determine how the model would estimate the leak rate provided the C(*x*, *y*, *z*) values from the CH_4(*g*) sensor and Pico laser spectrometer. The resulting emission estimates were compared against the calculated value. The suitability of the experimental design, the quality of the UKySonde sensor vs the Pico spectrometer measurements, and the accuracy of the dispersion model for leak rate estimates from sUAS measurements was analyzed.

4.3 Results and Discussion

4.3.1 Quantifications of Fugitive $CH_4(g)$

Three sets of experiments on February 7th, 11th, and 27th, 2020 measured the $CH_4(g)$ mixing ratio of a known, small $CH_4(g)$ leak ~50 m downwind. All three sets of experiments experienced the same calculated leak rate of 41.16 mg sec^{-1} $CH_4(g)$ for each of the three trials. In total, there were 9 coordinated gas releases/flights. The first experiment utilized a flight pattern that was not ideal for modeling the plume after dispersion downwind. The flight plan traversed a constant altitude (z), raster scanning the xy plane downwind of the plume. Upon analysis of the data, it was determined that the data collected did not sufficiently characterize or quantify the plume to provide near estimates of the $CH_4(g)$ leak rate. The flight pattern that provided the necessary data was a flight at a constant distance downwind, traversing the xz plane (Figure 4.2b). The next flights confirmed that the adjustment to the flight pattern described in Figure 4.2b was ideal for capturing methane fluxes as the plume dispersed through the boundary layer downwind of the source. The remaining experiments successfully captured the plume in all gas releases. The in-situ meteorological measurements and corresponding turbulent statistics that parameterized the dispersion model are reported first.

4.3.1.1 Measurements of Turbulent Statistics

$CH_4(g)$ releases were characterized by a $CH_4(g)$ sensor, a $CH_4(g)$ spectrometer, and a dispersion model (Equation 4.1). The dispersion model inputs measured in-situ by the sUAS were GPS position (x, y, z) and corresponding average wind speed measurements $\bar{U}$ (x, y, z). In-situ measurements of PTH and U calculated Z, u_*, $\bar{U}$, σ_u, $\langle U \rangle$, and T_L to

parameterize γ for all experiments. The dispersion model parameters and turbulent statistics measured for the gas releases on February 27th, 2020 are reported in Table 1.

Table 4.1 Measured and Calculated Turbulent Statistics for Dispersion Model Input Parameters on February 27th, 2020.

Gas Release #	**Z (m)**	**u_* (m sec^{-1})**	**$\bar{U}$ (m sec^{-1})**	**σ_u (m sec^{-1})**	**‹U›** **(m^2 sec^{-2})**	**T_L (sec)**	**γ (m^2 sec^{-1})**
1			3.65	1.72	2.95	32.1	94.7
2	400	1.00	4.80	1.29	1.66	27.1	45.1
3			5.17	1.33	1.77	24.4	43.3

4.3.1.2 $CH_4(g)$ Measurements and Model Estimates

Fugitive $CH_4(g)$ measured by the UKySonde $CH_4(g)$ sensor, the Pico $CH_4(g)$ spectrometer, and estimated by the dispersion model is presented next. The $CH_4(g)$ mixing ratios and fluxes measured by the UKySonde sensor are illustrated first in Figure 4.3a, 4.3b, and 4.3c, and Figure 4.4a, 4.4b, and 4.4c respectively. $CH_4(g)$ mixing ratios and fluxes measured simultaneously with the Pico spectrometer are provided next in Figure 4.3def, and Figure 4.4def. Finally, the dispersion model estimates of the coincident gas releases are presented in Figure 4.3ghi and Figure 4.4ghi.

4.3.1.2.1 UKYSONDE $CH_4(G)$ MEASUREMENTS

Measurements of GPS, U, and $CH_4(g)$ were spatiotemporally aligned and interpolated over the xz plane downwind of the methane leak (Figure 4.3abc and Figure 4.4abc). During these experiments, the $CH_4(g)$ sensor measured peak $CH_4(g)$ mixing ratios of 2.58, 2.43, and 2.61 ppmv. The fugitive $CH_4(g)$ fluxes were determined to be 1.58, 2.49, and 3.47 mg m^{-2} sec^{-1} respectively. In all three experiments, the $CH_4(g)$ sensor qualitatively

captured the plume and measured the peak mixing ratio to be ~0.5 ppmv, or ~2.5 mg m^{-2} sec^{-1}, above the typical background level.

4.3.1.2.2 PICO $CH_4(g)$ MEASUREMENTS

The Pico spectrometer $CH_4(g)$ measurements are illustrated in Figures 4.3 and 4.4 (middle column). The average plume measured for each experiment (Figure 4.3def and Figure 4.4def) determined peak $CH_4(g)$ mixing ratios of 2.58, 2.42, and 2.62 ppmv respectively. The maximum fugitive $CH_4(g)$ fluxes for each experiment were 3.17, 1.90 and 2.88 mg m^{-2} sec^{-1} respectively. Across the three experiments, the $CH_4(g)$ spectrometer qualitatively captured the plume and measured the peak mixing ratio to be ~0.5 ppmv, or ~2.6 mg m^{-2} sec^{-1}, above the typical background level.

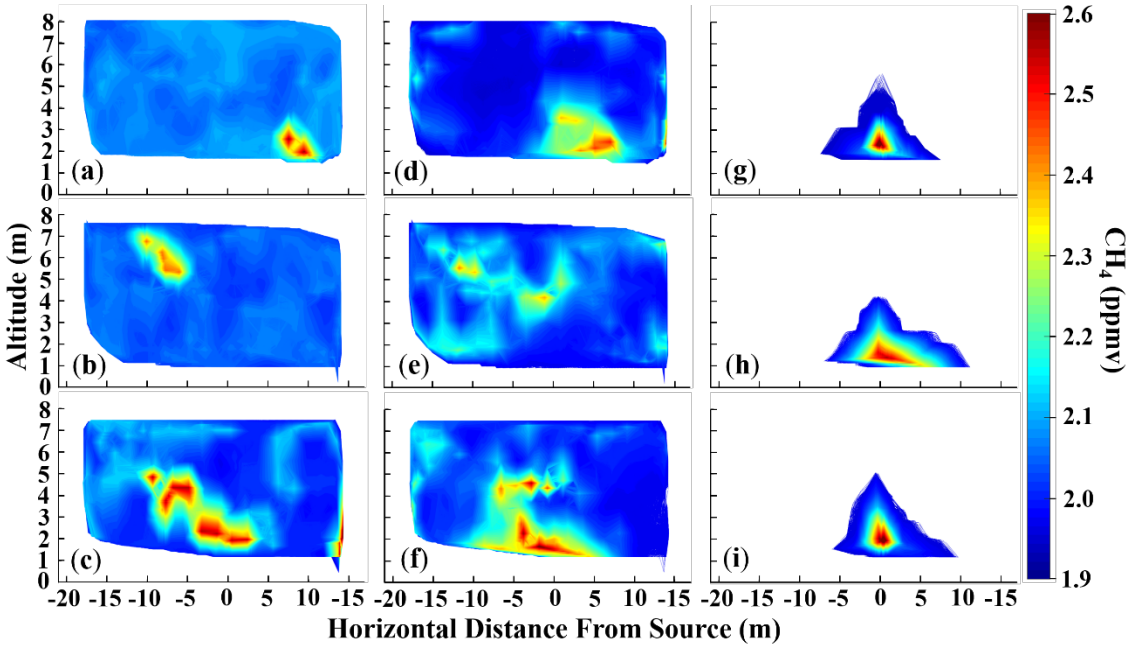

Figure 4.3 $CH_4(g)$ mixing ratios (in the plane of the sUAS, 50 m downwind of the source) determined by the UKySonde sensor, Pico spectrometer, and dispersion model on 27 February 2020 from 3:30 - 3:40 p.m. (UTC -5h) (top row), 3:45 - 3:55 p.m. (middle row), and 4:00 - 4:10 p.m. (bottom row). The UKySonde $CH_4(g)$ sensor measured peak mixing ratios of (**a**) 2.58 ppmv; (**b**) 2.43 ppmv; and (**c**) 2.61 ppmv; the Pico $CH_4(g)$ spectrometer measured peak mixing ratios of (**d**) 2.58 ppmv; (**e**) 2.42 ppmv; and (**f**) 2.62 ppmv; and the dispersion model estimated peak $CH_4(g)$ mixing ratios of (**g**) 2.74 ppmv; (**h**) 2.57 ppmv; and (**i**) 2.71 ppmv in the plume.

4.3.1.2.3 Dispersion Model Estimates

4.3.1.2.3.1 $CH_4(g)$ Flux Estimates

The dispersion model was provided $\dot{m}$, $\bar{U}$ (x, y, z), and γ to estimate the $CH_4(g)$ concentrations and fluxes over the same flight pattern as the sUAS (Table1). The modeled plume (on the xz axis, 50 m downwind) for the three experiments is provided in Figures 4.3ghi and Figure 4.4ghi. The model estimated peak $CH_4(g)$ mixing ratios of 2.74, 2.57, and 2.71 ppmv respectively. These concentration estimates determined maximum $CH_4(g)$ fluxes of 3.36, 2.82, and 2.96 mg m^{-2} sec^{-1} for the three experiments.

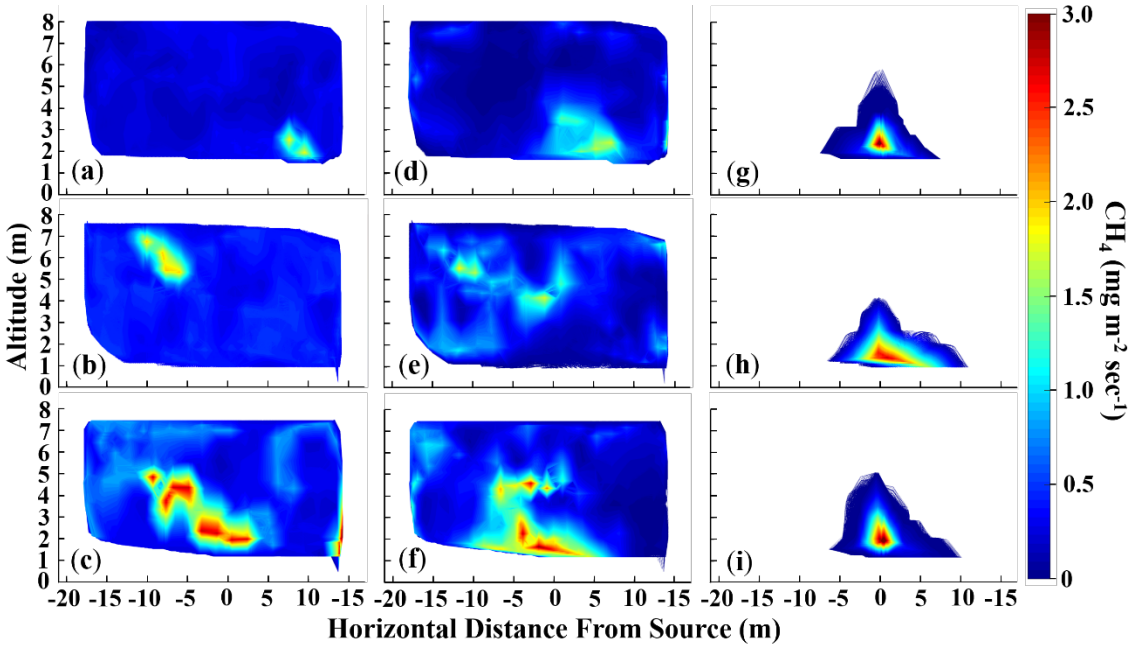

Figure 4.4 $CH_4(g)$ fluxes (in the plane of the sUAS, 50 m downwind of the source) determined by the UKySonde sensor, Pico spectrometer, and dispersion model on 27 February 2020 from 3:30 - 3:40 p.m. (UTC -5h) (top row), 3:45 - 3:55 p.m. (middle row), and 4:00 - 4:10 p.m. (bottom row). The UKySonde $CH_4(g)$ sensor measured peak mixing ratios of (**a**) 1.58 mg m^{-2} sec^{-1}; (**b**) 2.49 m^{-2} sec^{-1}; and (**c**) 3.47 m^{-2} sec^{-1}; the Pico $CH_4(g)$ spectrometer measured peak mixing ratios of (**d**) 3.17; (**e**) 1.90; and (**f**) 2.88 m^{-2} sec^{-1}; and the dispersion model estimated peak $CH_4(g)$ mixing ratios of (**g**) 3.36; (**h**) 2.82; and (**i**) 2.96 m^{-2} sec^{-1} in the plume.

4.3.1.2.3.2 Emission Rate Estimates from sUAS $CH_4(g)$ measurements

The ability of the dispersion model to predict the $CH_4(g)$ leak rate was evaluated by solving Equation 4.1 for $\dot{m}$. This derivation enabled leak rate estimates through inputs of $C(x, y, z)$ from the $CH_4(g)$ sensor/spectrometer and $\bar{U}(x, y, z)$ measurements. The leak rates estimates using the UKySonde $CH_4(g)$ sensor $C(x, y, z)$ measurements as inputs were 49.3 mg sec^{-1}, 45.1 mg sec^{-1}, and 47.7 mg sec^{-1} for the three experiments respectively. These estimates were 19.8%, 9.57%, and 15.9% lower than the true mass flow rate of 41.16 mg sec^{-1}. The leak rate estimates using the measurements collected by the $CH_4(g)$ spectrometer were 49.0, 44.7, and 43.1 mg sec^{-1} respectively. These estimates were 19.0%, 8.60%, and 4.71% lower than the true value.

The results from the three gas releases are summarized in Table 2. The $CH_4(g)$ sensor measured an average peak mixing ratio of 2.54 ± 0.10 ppmv, determined a peak flux of 2.51 ± 0.48 mg m^{-2} sec^{-1}, and (via dispersion modeling) an estimated leak rate of 47.4 ± 2.1 mg sec^{-1}. The $CH_4(g)$ spectrometer predicted a peak mixing ratio of 2.54 ± 0.11 ppmv, determined a flux of 2.65 ± 0.34 mg m^{-2} sec^{-1}, and an estimated leak rate of 45.6 ± 3.1 mg sec^{-1}.

Table 4.2 Summary of UKySonde sensor and Pico spectrometer $CH_4(g)$ plume measurements and leak rate estimates on February 27th, 2020.

	UKySonde			**Pico**			**Modeled**		
Gas Release #	**1**	**2**	**3**	**1**	**2**	**3**	**1**	**2**	**3**
$CH_4(g)$ (ppmv)	2.58	2.43	2.61	2.58	2.42	2.62	2.74	2.57	2.71
$\frac{\text{mg } CH_4(g)}{m^2 \text{ s}}$	1.58	2.49	3.47	3.17	1.90	2.88	3.36	2.82	2.96
	Dispersion Modeled Leak Rate Estimates								
C(*x*, *y*, *z*)	**UKySonde**			**Pico**					
Gas Release #	**1**	**2**	**3**	**1**	**2**	**3**			
$\frac{\text{mg } CH_4(g)}{s}$	49.3	45.1	47.7	49.0	44.7	43.1			
% error	19.8	9.57	15.9	19.0	8.60	4.71			

4.3.1.3 Discussion of Fugitive CH_4(g) Results

4.3.1.3.1 UKySonde Sensor vs Pico Spectrometer

Quantitatively, the measurements summarized in Table 2 validated the UKySonde $CH_4(g)$ measurements with the measurements collected by the Pico spectrometer. The $CH_4(g)$ ppmv measured, and flux calculated, agreed within measurement error for the sensor and the spectrometer. Qualitatively, the plume shape was not always identical for each experiment, but it did not affect the peak mixing ratio measured, the flux calculated, or significantly alter the leak rates estimated. The first plume measured was offset 7 m to the right of the source, indicating that the plume traveled approximately 0.15 m sec^{-1} to the right before passing through the xz plane measured by the sUAS. The $CH_4(g)$ sensor and spectrometer determined plume locations in agreement for the first experiment (Figure 4.3a, 4.3d respectively).

Unlike the first experiment, the plume measured was more diffuse and detected 0-15 m to the left of the source, suggesting a variable change in the crosswind between the first and second flight of about 0.6-0.8 m sec^{-1}. There were also more buoyant atmospheric forces present during this flight, lifting the plume 4-5 m AGL over 50 m. The change in plume characteristics is observed for both the sensor and spectrometer (Figure 4.4b, 4.4e respectively), indicating meteorological conditions caused the change.

The third plume measured was spread over a 10 m region centered slightly to the left of directly downwind. This suggests that the wind shifted slightly throughout the flight, and the plume was detected over a larger area, but remained closer to the ground. The sensor and the spectrometer both measured the plumes in approximately the same location during the third experiment (Figure 4.4c, 4.4f). These findings demonstrate that small

changes in the meteorological conditions experienced between gas release experiments do not affect the $CH_4(g)$ quantification.

The peak mixing ratios were similarly measured by the UKySonde sensor and Pico laser spectrometer for all three experiments. The results validate the ability of the UKySonde $CH_4(g)$ sensor to quantify fugitive methane fluxes through coincident measurements with the Pico laser spectrometer. The consistent findings between the $CH_4(g)$ sensor and spectrometer suggest that the sensor could provide plume quantifications $\geq$ 0.5 ppmv for flux determinations $\geq$ 3 mg $CH_4(g)$ m^{-2} sec^{-1}.

4.3.1.3.2 EVALUATION OF DISPERSION MODEL

The results, summarized from all experiments, revealed the model predicted peak mixing ratios and fluxes within the error of the $CH_4(g)$ measurement techniques. However, there were qualitative differences in the plume characterization. First, the dispersion model did not account for buoyant atmospheric forces. This was most evident in the second experiment, where the measurements detected the plume ~5 m AGL but the model predicted the plume passing through the plane at ground level. The exclusion of the vertical dispersion forces limited the amount of predicted dispersion and estimated a less diffuse plume than measured. The model also assumed the mean wind velocity was perfectly perpendicular to the sampling plane. In all experiments, the flight pattern was designed to mitigate this assumption. Unfortunately, the measured plume was not always perfectly centered at the origin and, as previously discussed, minor shifting crosswinds were observed. The consequences of the shifting meteorological conditions are illustrated in the discrepancy of the modeled and measured plume location and diffusivity. The inclusion of buoyant forces and multiple terms for wind velocity would enhance the diffusion and

improve the location of the plume predicted by the dispersion model. These additions would enhance the ability of the model to the predict measured values.

Although the demonstration of accurately quantified peak mixing ratios/fluxes validated the model output, more value is derived from the leak rate estimations provided by the model. The novelty of the research is the ability of the measurement techniques, combined with dispersion modeling, to accurately predict the leak rate of an unknown source. The model provided acceptable estimates within 19.8% of the true leak rate for all trials. The overestimation of the peak $CH_4(g)$ flux did not significantly affect the leak rate estimate for that trial, demonstrating that even in non-ideal atmospheric wind conditions, the model still characterizes the leak rate with a reasonable error. The evaluation of the model is weighted more on the accuracy of the leak rate estimate.

A key observation from Table 2 is the model consistently overestimated the true leak rate. It was determined that the dispersion model, using the sensor and spectrometer $CH_4(g)$ measurements, estimated an average leak rate 13.0% higher than the true value of 41.16 mg sec^{-1}. This translates to average estimates 5.34 mg sec^{-1} more than the true value, with ~30 min of sampling data. The prediction is impressive considering the accuracy and brevity of the estimate, but results demonstrate that crosswinds and buoyant forces are currently not accounted for. The leak rate estimations could be improved through inclusion of more sophisticated dispersion model parameterization that includes turbulent statistics to characterize all three dimensions of atmospheric forcing. The inclusion of more dispersion forces would reconcile the differences observed and improve future model estimates. This would be accomplished by using the sUAS measurements to determine parameters that characterize turbulent diffusivity for x, y, and z directions.

4.3.2 Proof-of-Concept Flights with $H_2S(g)$ and $SO_2(g)$ Sensors

The sensor package designed to measure H_2S and SO_2 was deployed on March 5th, 2020 for background measurements and proof-of-concept experiments demonstrating the sUAS' ability to characterize volcanic plumes. These experiments utilized a series of stacked 100 m loiter circles to characterize the immediate surrounding environment over the crater of a volcano. The origin was set to the center of the loiter circle to represent a typical plot generated during a field campaign. During these flights, the sUAS measured mixing ratios of typical volcanic gases (H_2S and SO_2) and meteorological conditions. The flight path and the corresponding concentrations of H_2S and SO_2 are provided in Figures 4.4 and 4.5 respectively.

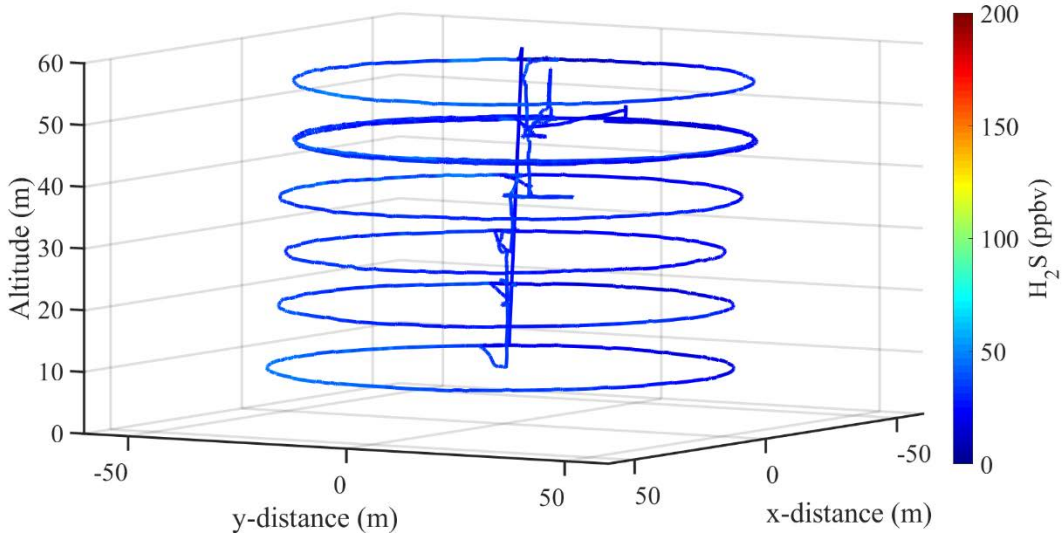

Figure 4.5 Stacked 100 m diameter loiter circles measuring H_2S from 1:43 - 2:10 p.m. (UTC -5h) on 5 March 2020. The loiter circles started at 10 m above ground level and ascended by 10 m to 60 m. The average background mixing ratio of H_2S measured was 29.90 ± 7.75 ppbv.

The H_2S sensor performed as expected on board the sUAS and measured a background mixing ratio of 29.90 ± 7.75 ppbv. The sensor did not experience any significant changes in behavior throughout the flight (i.e. environmental interference due

to the introduction of radio telemetry or interference from UAV motors, solar radiation, aspiration, etc.) and measured a background concentration of a few ppbv.[150] It is important to note that the H_2S concentrations expected within ~100 m of a volcanic plume are two orders of magnitude (100x) larger than the concentrations measured in this flight. The variance in the background concentration is negligible when measuring >1000 ppbv of H_2S in a volcanic plume.

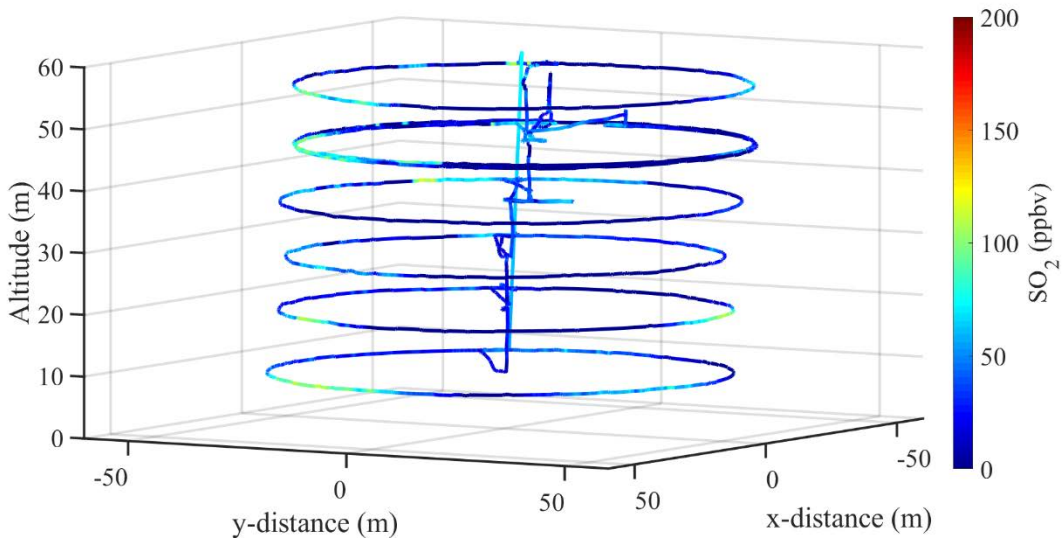

Figure 4.6 Stacked 100 m diameter loiter circles measuring SO_2 from 1:43 - 2:10 p.m. (UTC -5h) on 5 March 2020. The loiter circles started at 10 m above ground level and ascended by 10 m to 60 m. The average background mixing ratio of SO_2 measured was between 29.27 ± 26.37 ppbv.

The SO_2 sensor also performed as expected and measured a background mixing ratio of 29.27 ± 26.37 ppbv on board the sUAS. The sensor did not experience any significant changes in behavior due to environmental interference throughout the flight and measured a background concentration of a few ppbv.[150] The SO_2 circuitry is twice as sensitive to electrical noise as the partner H_2S circuit. This is evident in the variance of the SO_2 background concentration measured. The results found the SO_2 sensor does not perform as well in the low ppbv region as the H_2S sensor, but it must be acknowledged that the

concentrations expected within ~100 m of a plume are three orders of magnitude (1000x) larger than the concentrations measured in this flight, and an order of magnitude (10x) larger than the H_2S concentrations. The noise in the background concentration measurements is inconsequential considering SO_2 measurements in the volcanic plume will be >10,000 ppbv.

4.4 Conclusions

The $CH_4(g)$ release experiments demonstrate the application of an sUAS, flight pattern, and dispersion model to quantify plumes and enable leak rate estimates within 13.0% of the true leak rate. The low-cost, lightweight UKySonde $CH_4(g)$ sensor provided measurements consistent with the industry-leading portable $CH_4(g)$ spectrometer, validating the capability of the UKySonde $CH_4(g)$ for accurate plume detection and characterization. There was no obvious or significant advantage to using the spectrometer for these experiments; but, the ability of the Pico spectrometer to detect both methane and ethane simultaneously is useful for determining if the leak is biogenic or anthropogenic in origin. However, considering the performance vs cost analysis (the price of the two systems differs by tens of thousands of dollars), the UKySonde sensor was concluded to be the ideal sensor choice for $CH_4(g)$ because the two methods predicted leak rates within the 95% confidence interval, only differing by less than 3% of each other. The model also performed reliably, predicting leak rate estimates within 4.8-19.8% of the true value and reporting peak $CH_4(g)$ values within 3.4-6.2% for all trials. From these findings, it was concluded that the model does provide a reasonable estimate for the leak rate, especially considering the simplicity of the model and the assumptions made. For leak quantification within ~20%, or certainly for leak identification, this modeling method combined with the

sUAS sampling provided results that are accurate enough to characterize fugitive gas plumes. It is expected that the results will improve with more significant gas leaks. The leak studied herein was a small, low mass flow leak with elevated concentrations of only 0.5 ppmv at 50 m. For context, over 95% of the 283 methane leaks monitored in Ft. Worth, TX, USA recorded an average of two methane leaks per site of >500 ppmv.[157] This suggests the technique described herein is valid for most all industrial methane gas leaks and capable of distinguishing fugitive methane from background concentrations in real world applications of unknown leak rates.

The volcanic plume measurement system performed as expected during the proof-of-concept flights demonstrated herein. The H_2S and SO_2 sensors functioned reliably during the field experiment, demonstrating the sensor's ability to operate successfully during future sUAS missions. The flight pattern was representative of conditions expected during a field campaign and served as a successful demonstration of the sUAS application. Importantly, the radio telemetry providing the real time data operated flawlessly throughout the flight without interference from the UAV telemetry or nearby structures. Thus, there is confidence that the platform will perform during the deployment over an active volcano and will successfully characterize the plume with the method proposed.

Abbreviations

ABL, atmospheric boundary layer; AFE, analog front end; AGL, above ground level; $C(x, y, z)$, concentration of methane at a specified 3D position; CH_4, methane; CO_2, carbon dioxide; FAA, Federal Aviation Authority; GHG, greenhouse gas; GPS, global positioning system; γ, turbulent diffusivity; H_2S, hydrogen sulfide; IPCC, Intergovernmental Panel on Climate Change; $\dot{m}$, mass flow rate; NO_X, nitrogen oxide; O_3,

ozone; OH, hydroxyl radicals; PTH, pressure, temperature, and relative humidity; *r*, distance of the measurement from the location of the release; RH, relative humidity; SO_2, sulfur dioxide; sUAS, small unmanned aerial systems; σ_u, standard deviation of wind speed; $T_{L,}$ Lagrangian integral timescale; UAV, unmanned aerial vehicle; U, wind speed; $\bar{U}$, average wind speed; ‹U›, variance of the wind speed; u_*, eddy orbital velocity; WRF, weather research and forecasting; Z, boundary layer height;

CHAPTER 5. GREATER CONTRIBUTIONS TO SCIENCE THROUGH THE DEVELOPMENT AND APPLICATIONS OF SUAS

The research herein has contributed to the advancement of atmospheric, environmental, and analytical chemistry through the development, calibration, validation, and application of small unmanned aerial systems (sUAS). The experimental findings have been summarized into three major contributions: 1) the development of the sUAS as a platform for atmospheric measurements; 2) meteorological applications of sUAS; and 3) trace gas measurements with sUAS. The contributions are structured to follow the progression of the research as it evolved. Establishing the sUAS as a legitimate scientific tool for atmospheric measurements was the first research contribution. The second was deploying the sUAS to measure meteorological conditions and study the atmospheric boundary layer (ABL). The final contribution was using the calibrated and validated sUAS for measurements and dispersion modeling of fugitive trace gas fluxes. The research ultimately enabled novel studies that quantified and modeled the atmospheric transport of trace gases to better understand their impact on environmental and atmospheric chemistry.

5.1 sUAS as a Platform for Atmospheric Measurements

The small unmanned aerial system (sUAS) is a novel and useful analytical tool for collecting atmospheric measurements. The mobility of unmanned aerial vehicles (UAVs) facilitates measurement densities in time and space that cannot be rivaled by any other existing technique <100 m above ground level (AGL) . The research herein enabled a thorough summary of the emergence of sUAS in science, and their transition from military applications to platforms for atmospheric research.[76, 89] In this section, the research contributions that developed the sUAS into a scientific tool is explained through: 1) an

analysis of UAVs for atmospheric research; 2) characterizations of trace gas sensor packages for UAVs; and 3) the optimization of sensor integration, calibration, and validation for UAVs.

5.1.1 Analysis of UAVs for Atmospheric Research

Three different classifications of UAVs and their suitability for use in atmospheric research were discussed in detail: (1) micro aerial vehicles (MAVs); (2) vertical take-off and landing (VTOL); and (3) low-altitude short endurance (LASE) systems.[76] A payload of <5 kg with a flight time of 10-20 minutes was recommended for rotary wing (MAVs or VTOLs) UAVs.[76] For fixed wing (LASE) UAVs, a wingspan of < 3 m, a payload of < 5 kg, and flight time of 120 minutes was advised.[76] The development of sUAS legislation for operation in atmospheric research is complicated and rapidly evolving. Dissecting and comprehending the legislative jargon is time consuming and difficult to interpret. Herein, sUAS classifications and guidelines for ~20 countries (including Federal Aviation Authority (FAA) part 107 laws) were provided.[76] The information presented remains the only known summary of international sUAS laws for atmospheric measurements in the literature, and is an excellent resource for quickly identifying airspace regulations.

5.1.2 Characteristics of Trace Gas Sensor Packages for UAVs

Herein, The justification of sUAS as useful platforms for atmospheric research expanded further to discuss three different types of trace gas sensors available for UAV integration.[76] The operating principles of two types of metal-oxide semiconductor sensors, a modified catalytic sensor, and an infrared laser-absorption technique were explained with examples of integration for useful sUAS measurements.[76] Benchtop instruments are not suitable for sUAS integration due to the size, weight, and operating conditions required for

laboratory precision. Sensors for sUAS integration must operate at variable environmental temperatures and pressures, eliminating most traditional analytical techniques. Therefore, procedures for integrating analytical systems into UAVs was created and included the hardware, software/coding languages, and overall system constraints (weight, power, memory) required.[76] Additionally, the flow of a centralized system for time, position, and sensor data acquisition/logging was explained for streamlined data management.[76] Overall, an integrated system that recorded time, position, meteorological conditions, and relevant trace gas mixing ratios was described.[76] A cost analysis of UAVs and trace gas sensors relevant for atmospheric measurements was also included.[76] The cost of the UAV, autopilot systems, and sensors can vary widely. Detailed examples of several different sUAS (from <$1000 to >$10,000) provided the necessary information to budget for future grants.[76] The analysis concluded by acknowledging initial development efforts and critiquing the limitations of current/prior sUAS. A literature review, backed by preliminary experiments, revealed that initial sUAS deployments resulted in unacceptable measurement errors due to variations in environmental conditions, sensor aspiration, sensor exposure to solar irradiation, and electronic interference. It was determined that developing protocols for sensor calibration and validation on board sUAS was critical to sensor accuracy and data reproducibility.[89]

5.1.3 Optimization of Sensor Integration, Calibration, and Validation for UAVs

Through the work provided in this dissertation, four novel calibration/mitigation techniques have been designed to characterize meteorological and trace gas measurements for two LASE and four VTOL sUAS. Specifically, sensor responses to: 1) variable environmental conditions (i.e. temperature and relative humidity); 2) exposure to solar

irradiation; 3) sensor aspiration; and 4) electronic noise were characterized thoroughly and mitigated through the development of calibration/validation procedures.

5.1.3.1 Calibrations for Temperature and Relative Humidity

To enable full control of atmospheric composition and meteorological conditions for sensor calibrations of variable temperature and relative humidity, an environmental chamber was custom-made using three mass flow controllers (MFC), an inline gas heater, and a sparger.[89] The MFCs were programmed for dynamic chamber changes permitting systematic and efficient calibrations over the range of environmental conditions expected. A matrix of calibration coefficients were determined and integrated into device software for in-situ measurement corrections.[89] Although the development of environmental chambers is not new, the application to characterize sensors for sUAS measurements was not reported. These experiments optimized a calibration technique that enabled the use of sUAS for reliable measurements in the variable weather conditions experienced during data flights.[89] Sensor calibrations for variable temperature and relative humidity were previously undocumented in this context and were necessary to improve sUAS measurements.

5.1.3.2 Calibrations for Solar Irradiation

A solar irradiance spectrometer was mounted to a sUAS via a custom 3D printed mount and was deployed to determine variations in sunlight power with altitude and time of day. Using these measurements, a xenon mercury lamp was properly attenuated and filtered to replicate the power and spectrum of sunlight, and used as the model light source to correct for measurement errors attributed to solar irradiation.[89] These experiments

concluded that direct sunlight decreased sensor lifetime and a >5 mm thick 3D printed polylactic acid shield attenuated the solar irradiation, prolonged sensor lifetime, and prevented sensor drift.[89] This is the only known experiment that deployed a solar irradiance spectrometer on a sUAS to characterize sensor behavior under variable sunlight intensities.

5.1.3.3 Calibrations for Sensor Aspiration

Aspiration is critical for sensor performance and key to a successful sUAS design. Sensor placement and aspiration are correlated; poor sensor placement generates undesirable and irregular sensor aspiration, leading to irreproducible measurements. An extensive series of experiments demonstrated the complexity, and lack of uniformity, of air flow between different sUAS.[89] The fuselage of the LASE sUAS was placed in a wind tunnel to characterize the effects of variable wind speeds on sensor signals.[89] These experiments inspired a specially designed inlet (*U.S. Patent App. Ser. No. 16/454,495*) that was integrated into the fuselage and facilitated the steady flow of air over the sensors.[89] However, a pumped system with a sampling port extending outside of the prop wash and facing the direction of travel (and/or the wind direction) was optimal for VTOL sUAS.[89] For naturally aspirated sensors on VTOL sUAS, the signal accuracy depends on the vertical velocity. Validation measurements with a tethered balloon concluded accurate profile data was collected on the ascent.[89] Through the development of the novel sUAS designs presented herein, examples of proper sensor placement were illustrated for other researchers in the field to observe and replicate.

5.1.3.4 Mitigation of Electrical Interference

Circuits for trace gas sensors must be extremely sensitive to small voltage variations to resolve the minute concentration differences of the target analyte. Therefore, integrating the sensor packages into the electrical environment of an sUAS introduced a significant technical challenge. The sUAS relies heavily on the accuracy of the global positioning system (GPS), inertial measurement units (IMUs), and magnetometers for orientation feedback and flight control. These critical UAV systems, along with the radio telemetry signal, must remain unaffected by the introduction of new electronic circuits for reliable flight performance. This remained true for the data collected by the integrated trace gas sensor packages. The sensitive trace gas circuits were far more susceptible to electrical interference than the sUAS instrumentation, and depending on the sensitivity of the circuit, 2-3 mV of electrical noise introduced ~5-10 ppbv of signal noise. A study determined the radio signal was the most common source of sensor noise. A Fourier transform of the sensors' analog signals generated periodograms (power density spectrums) that revealed low frequency noise, eliminating lowpass filtering as a post-processing treatment. The necessary high pass filter eliminated the lowest frequency of the data (the mean) and completely removed the signal altogether. The radio telemetry could not be removed, so the sensors were carefully oriented, shielded, and grounded. The dissemination of novel calibration and validation techniques is imperative to the advancement of this research field. A prominent scientific challenge is demonstrating sensor accuracy/precision through sensor validation on board sUAS. The research field has benefitted greatly through the presentation of new knowledge and techniques that characterized the effects of the four most common sources of measurement error introduced by the sUAS.

The research herein has advanced the sUAS as a platform for atmospheric measurements. This was accomplished through a deeper understanding of the history and classification of UAVs (including current laws and regulations); a detailed explanation and cost analysis of trace gas and meteorological sensors suitable for UAV integration; and addressing the analytical challenges of UAV sensor integration through novel calibration and validation methods that characterized or diminished sensor biases initiated by variable meteorological conditions, solar irradiation, sensor aspiration, and electronic noise. Acknowledging the recent and rapid progress of sUAS development, the future of the platform for atmospheric measurements is promising. The research has demonstrated proof-of-concept experiments aimed to validate the sUAS against existing methods, and has made progress in expanding the sUAS' role as a legitimate analytical instrument.[76, 89] As the sUAS platform continues to advance and become established in the literature, the research applications become more impactful. The scientific contributions derived from applications of meteorological and trace gas measurements via calibrated/validated sUAS are discussed next.

5.2 Meteorological Applications of sUAS

The research accomplished herein has demonstrated several applications of sUAS to enhance the quality of meteorological measurements. The four major contributions of sUAS for meteorological applications are: 1) measurements of pressure, temperature and relative humidity (PTH); 2) the determination of turbulent statistics; 3) advanced atmospheric boundary layer (ABL) meteorology; and 4) the validation of real-time mesoscale weather research and forecasting (WRF) models. Meteorological measurements

with sUAS was a necessary step to determine the turbulent statistics required for fugitive gas flux measurements and dispersion models.

5.2.1 Measurements of PTH

From elementary measurements of PTH, advanced atmospheric characteristics can be derived. Simultaneous measurements of temperature and pressure yield potential temperature. Potential temperature is an altitude-independent value of atmospheric temperature that better measures the adiabatic lapse rate and vertical atmospheric stability. The vertical stability of the atmosphere was characterized by the altitude profile of potential temperature in the ABL. Coincident measurements of temperature and relative humidity obtained absolute humidity, or the specific water content in the atmosphere, a value independent of temperature changes. Aloft measurements of absolute humidity are important for meteorologists to assess the precipitable water content in a geographic area. This provided insight into why storm cells produced heavier rainfalls than the predicted precipitable water under certain atmospheric conditions. The addition of sUAS absolute humidity measurements in the ABL provided evidence of their ability to increase the accuracy of precipitation forecasts. Together, measurements of meteorological parameters (PTH, 3D wind velocities) were extremely useful in determining atmospheric boundary layer stability through characterizations of the vertical and horizontal forces that drive atmospheric transport. In addition to providing meteorological measurements, the research progressed to more significant implications. The determination of turbulent statistics from PTH and 3D wind measurements (U, V, W) is discussed next.

5.2.2 Determination of Turbulent Statistics

Meteorological measurements (i.e. PTH, U, V, W) were necessary to understand the current state of the atmosphere and served as input parameters for dispersion and advanced weather models. sUAS were ideal platforms for meteorological measurements because they were deployed quickly, inexpensively, and safely with spatiotemporal resolutions far better than current methods utilizing weather stations/towers, satellites, and weather balloons. The density of the atmospheric data collected is important because model outputs rely significantly on the concentration and accuracy of the input parameters. The fine-scale measurements collected by sUAS provided new opportunities for detailed studies of the ABL. Advantageously, the vertical and horizontal structures of the ABL were better defined through the inclusion of sUAS data. U, V, W measurements in the lower boundary layer allow mapping of the vertical and horizontal wind vectors. The inclusion of in-situ wind measurements enabled the calculation of turbulent statistics from measured values (not estimates). The application of sUAS to calculate turbulent diffusivity for dispersion modeling is an important and novel contribution to the field. Gas dispersion and weather forecasts depend on the vertical/horizontal motions of the ABL. Through sUAS meteorological measurements that characterized the atmospheric forces and turbulent statistics, flux measurements were enabled, and dispersion model performance was improved.

5.2.3 ABL Meteorology

The ABL is the region of the atmosphere effected by diurnal heat cycles and governs atmospheric transport near the surface. The boundary layer height was delineated by a shift

in atmospheric stability defined by the change in measured adiabatic lapse rate. Typical boundary layer heights ranged from tens of meters in extremely stable conditions to several kilometers over highly convective environments. The ABL transition coincided with the change in radiative energy accompanied by sunrise and sunset (the diurnal cycle). After sunset, and overnight, the radiative cooling of the Earth's surface cooled the surrounding air and produced a temperature profile that decreased with altitude. In the stable boundary layer described, the temperature inversion suppressed vertical motions and prevented mixing between the boundary layer and the rest of the troposphere. When the sun rose, the Earth's surface absorbed and radiated the energy back into the surface layer. As the air warmed at the surface, the temperature inversion disappeared and the boundary layer trapping dissipated, enabling mixing of the boundary layer and facilitating atmospheric transport. An exaggerated example of a boundary layer transition was studied in San Luis Valley, Colorado. The San Luis Valley is a high-altitude basin surrounded by tall mountain ranges. Overnight, the colder, denser air flowed down from the mountain tops and filled the basin, creating a cold air drainage that formed a distinct boundary layer of colder air over the basin. The location was unique because it enabled a case study of a turbulent boundary layer transition resulting in erratic weather patterns. The topography provided an environment contusive to studying the vertical turbulent motions that propagated into sudden and unpredictable thunderstorms.

The PTH measurements aided in determining the timeline and nature of the cold air drainage/ABL transition and in the future could serve as indicators of thunderstorm formation by measuring precipitable water. Characterizing the boundary layer through profiles of PTH enabled researchers to illustrate the current stability of the atmosphere for

improved weather forecasts. Furthermore, because the atmospheric stability also reflects the degree of atmospheric transport, these meteorological measurements were also useful for supplementing atmospheric pollutant measurements (i.e. anthropogenically generated trace gas fluxes). Measuring ABL meteorology was expanded further to validate weather predictions. A more global application of this research was demonstrated through an experiment that successfully validated a WRF model with coincident sUAS measurements.[90]

5.2.4 Validation of Real-Time Mesoscale WRF models

The validation of real-time, meso-scale weather forecasts was realized through an overnight experiment where a balloon launched unmanned glider completed a 25 km atmospheric profile.[90] This was the first reported experiment of its kind in the literature and pioneered a future of incorporating sUAS measurements to evaluate and improve WRF modeling. The sUAS traversed 35 km (horizontally) throughout the 6-hour flight campaign, providing unequivocal measurement densities of PTH from the surface to the stratosphere for comparison to a meso-scale real-time WRF model.[90] The research discovered WRF model predictions for temperature overlapped with sUAS measurements from the surface to the tropopause.[90] From the tropopause to approximately 20 km, the trend of the temperature profiles matched, but the values differed by a maximum of 3-4 degrees Celsius.[90] However, as the profile continued from 20 to 25 km, the prediction diverged from the measured value, reflecting the sparsity of the model input data available at higher altitudes.[90] The measured and modeled relative humidity and pressure profiles agreed throughout the 25 km profile.[90] These findings provided confidence that sUAS could be used reliably as supplemental sources of information to validate WRF models.

The scientific community has benefitted from the technological breakthroughs that pioneered the beyond visual line of sight (BVLOS) and nighttime research flights, two significant technical challenges of sUAS research. The risk of mission failures due to unforeseen weather conditions drastically increases as sUAS are incorporated for automated, periodic research flights. An unexpected wind shear or rainfall can be catastrophic for BVLOS or nighttime sUAS missions and improving meso-scale weather forecasts increases the probability of uneventful and reliable UAV missions. The enhanced detection and prediction of localized wind turbulence also helps UAVs safely perform flight operations in high traffic areas. As research advances, WRF models will use sUAS meteorological measurements as input parameters to improve the quality of real-time forecasts.[90] This has implications beyond typical research flights and benefits society, businesses, and the general public; whose health or economics often suffer due to inaccuracies in weather projections.[90]

The research herein has applied sUAS meteorological studies to determine ABL stability through measurements of PTH; calculate turbulent statistics from in-situ wind velocity measurements; characterize cold air drainage/ABL convection initiation; and validate real-time mesoscale WRF models. The methodologies and techniques learned from ABL meteorology facilitated predictive studies of the long-term effects of fugitive gases through sUAS flux measurements and dispersion modeling methods for advanced research in atmospheric and environmental chemistry.

5.3 Trace Gas Measurements with sUAS

The most advanced scientific impacts were realized by using the calibrated and validated sUAS to determine turbulent statistics for dispersion modeling and flux measurements of fugitive trace gases. The final contribution of the research was achieved through 1) analytical evaluations of trace gas sensors on sUAS; 2) proof-of-concept trace gas measurements with sUAS; 3) quantifications of fugitive gas from carbon capture systems; 4) trace gas flux measurements and leak rate estimates with sUAS; and 5) the demonstration of methodologies for future applications of sUAS measurements.

5.3.1 Analytical Evaluations of Trace Gas Sensors on sUAS

Evaluating trace gas sensors for the suitability of UAV integration is an important responsibility for accurate field measurements. As previously mentioned, extensive calibration and validation experiments were necessary to characterize the sensors for variable flight conditions (e.g. temperature, humidity, sunlight, aspiration, electrical noise). The research contributed further to the advancement of sUAS for trace gas measurements through a detailed analysis of the limit of detection (LOD), limit of quantification (LOQ), accuracy, precision, resolution, and time response for a variety of trace gas sensors.[89] In many cases, it was discovered that the sensors did not possess the specifications provided through the manufacturer.[89] Each trace gas sensor was analytically evaluated under conditions experienced during typical flight campaigns to ensure the sensor would perform in the field. At minimum, mild changes to the electrical circuit were introduced to provide a better signal to noise ratio for analog sensors. The power to the sensor was strictly regulated, and the analog to digital converter was changed to 16-bit.[89] These two electrical modifications improved sensor resolution, raised the signal to noise

ratio, and effectively lowered sensor LOD/LOQ. The research community benefited greatly through the evaluation of trace gas sensors for sUAS deployment as it is difficult to find sensors with specifications suitable for sUAS measurements.

Another important consideration is the time response of the trace gas sensors. A pumped system was easily characterized if the mass flow of the system was well calibrated. However, experiments found that many non-pumped systems suffered from a slowed time response, often related to incomplete or irregular sensor aspiration. As previously mentioned, the sensor aspiration of a non-pumped system on board a VTOL sUAS differed on ascent/descent. This dynamically changed the sensor response time and erratically shifted measurements in time and space. To counteract this, the optimal sensor response time was characterized in a laboratory environment and compared against the response time on the sUAS to demonstrate the sensor does not lag during field measurements.[89] These characterizations were difficult, time consuming, and did not transfer between different UAVs.[89] This reinforced the valuable suggestion that the systems should ideally be pumped or extremely well characterized for field measurements.

5.3.2 Proof-of-Concept Trace Gas Measurements with sUAS

The research herein has produced the first lightweight, low power consuming, operational trace gas and meteorological sensor package (UKySonde) that was integrated into LASE and VTOL UAVs through bespoke designs (*Patent Pending, App. No. 16/454,495*).[89] The package logged time, GPS (latitude, longitude, altitude), temperature, pressure, relative humidity and trace gas mixing ratios of methane, ammonia, and carbon dioxide. The sensor system has since demonstrated several applications on board four different UAVs. The first, and simplest, application was a proof-of-concept experiment

measuring environmentally relevant mixing ratios of methane, ammonia, and carbon dioxide. The UKySonde was simultaneously deployed on VTOL and LASE UAVs for 2D measurements of background trace gas mixing ratios. The result was a 2D plane of trace gas measurements spanning 1,200 m in length, and 120 m in height. Through this preliminary research, the sensor system logged over 50 flight hours of data and proved reliable for future field studies. Interestingly, the sensor system was also involved in a series of (preliminary) gas releases to demonstrate the usefulness of detecting fugitive gases with sUAS. Carbon dioxide was released up wind of the two sUAS while they flew in the distinct 2D flight pattern. The results indicated both sUAS passed through the carbon dioxide plume on several occasions, denoted by the elevated mixing ratios detected. This experiment provided new literature contributing a new flight pattern and a breakthrough lightweight, low power consuming sensor package for integration into two different UAVs.

5.3.3 Quantifications of Fugitive Gas from Carbon Capture Systems

To further demonstrate the capabilities of the UKySonde, another sUAS experiment measured elevated ammonia levels from the oxidative degradation of a monoethanolamine solvent. The monoethanolamine solvent was known to degrade and produce ammonia during the recirculation process that sequestered carbon dioxide from flue gas in carbon capture systems. The research successfully quantified the ammonia emissions and validated the UKySonde measurements against the traditional ion chromatography method. The research also incorporated a Gaussian plume dispersion model that provided the necessary requirements to translate the mixing ratios measured at the sUAS, to the actual mixing ratios of ammonia inside the smokestack, before diffusion

took place. To enable such systematic and replicable sampling, the sUAS platform was upgraded to incorporate a fully autonomous navigation system. Through this configuration, the pilot is no longer responsible for commanding the position, velocity, or acceleration of the sUAS. Instead, the autopilot received pre-determined waypoint missions and completed them with specified vertical/horizontal velocities. The autopilot provided the necessary position precision to facilitate systematic and repeatable flight patterns for higher quality data collection. The flight pattern chosen for these experiments was a single vertical profile over the stack. The measurements collected nearest the stack were the input concentrations for the gaussian model, and the measurements away from the stack were background measurements. The research successfully measured and accurately modeled the ammonia mixing ratio emitted in the flue gas of the carbon capture system.

However, it was learned through these experiments that more valuable information could be derived if the flight plan was more complex and incorporated in-situ wind velocity measurements. Thus, it was concluded that raster scan measurements of a plane downwind of the source was a more ideal flight pattern, and the incorporation of ultrasonic anemometers provided the wind measurements capable of determining the turbulent statistics required for flux measurements and advanced dispersion modeling.

5.3.4 Trace Gas Flux Measurements and Leak Rate Estimates with sUAS

To complete the study of the UKySonde's ability to measure trace gases, a methane gas release was coordinated to demonstrate the advancements in the characterization methodologies and the suitability of the methane sensor for flux measurements. To further validate the UKySonde methane measurements, a commercially available laser

spectrometer was also included in the sUAS payload. This spectrometer leads the industry in portable methane measurements and was adapted for integration into the sUAS. Three sonic anemometers were strategically placed (one above, two horizontally extended outside the prop wash) on the sUAS for the desired wind velocity measurements to calculate turbulent statistics. To accomplish the flights with the additional payload, a heavy-duty octocopter was utilized. As mentioned earlier, it is crucial to understand the classification of UAVs and to determine which UAV is best suited for the research application. Because the payload has increased to nearly 10 times the initial weight of the UKySonde sensor system, a new sUAS with adequate thrust was selected. In a series of gas release experiments, the sUAS measured the mixing ratio of several plumes, successfully capturing the methane flux through the xz-axis down wind of the point source leak. The UKySonde methane measurements determined fluxes consistent with the laser spectrometer. Through dispersion modeling, the leak rate was estimated within 2-25% of the true value. This study encapsulates and demonstrates the ability of an sUAS to characterize fluxes of point source gas leaks. The assimilation of time, position, methane mixing ratios, and wind velocity measurements provided the required data for accurate flux measurements and leak rate detection. Together, these measurements characterized the conditions that governed the concentration, size, shape, and transport of the fugitive methane plume. Improving fugitive trace gas inventories is imperative to determining the impact of how the gases chemically age in the atmosphere. Through this study, the scientific community has benefitted greatly through the dissemination of sensor systems and flight patterns robust enough to capture and characterize fluxes of trace gases.

5.3.5 Future Applications of sUAS Trace Gas Measurements

The future of the research aims to measure fluxes of point pollution sources with an unknown leak rate and use the developed sUAS methodology to constrain the errors of current estimations. For example, volcanoes are a well-known contributor of biogenic air pollution and are interesting because they suddenly release large magnitudes of trace gases into the atmosphere. They are known for their variable emissions of sulfur dioxide and hydrogen sulfide, but there are no dynamic methodologies developed that periodically, and autonomously, measure the surrounding boundary layer for any unexpected venting. Therefore, a new sUAS was established for this application that incorporated electrochemical sensors for sulfur dioxide and hydrogen sulfide and fast-response sensors for temperature, relative humidity, and wind velocity. Flying over a volcano not only introduced legal complications, it also presented new challenges for the logistics of sUAS flight operations. Sudden columns of hot gases, or highly corrosive environments, are detrimental to sUAS performance and in extreme situations, could lead to mission failure. The volcanic application required the development of a stand-alone radio telemetry system with custom ground station software that streamed data in real-time. This technological advancement only increased the payload by a few grams but provided immediate feedback on the local environment of the sUAS. This was helpful for plume detection, but real-time temperature measurements were imperative for managing safe flight operations. The research herein demonstrated the ability of the sensor system to operate in an experiment designed to replicate the flight pattern expected for volcanic measurements. The next step is obtaining permission from the National Park Services to legally complete these flights;

a non-scientific challenge that limits many of the applications of sUAS trace gas measurements.

Current regulations for sUAS research are clouded, the communication is limited, and the legislation needs improvement to keep up with the scientific development. For future studies aiming to integrate sUAS into everyday operations (BVLOS, nighttime missions, etc), significant changes are needed. Researchers must continue to work closely with government officials to ensure the development of UAV flight rules are timely and in the best interest of science. With the cooperation of both parties, the scientific applications of sUAS platforms can be utilized to its potential.

In conclusion, the research herein has advanced the sUAS as an analytical instrument for atmospheric trace gas measurements. The work has justified the sUAS as a legitimate scientific tool, presented unequivocally dense information about the atmosphere, and enabled new and exciting studies of fugitive gases. This was accomplished through extensive characterizations, calibrations, and validations of the sensors on board the sUAS. The research has developed sUAS and methodologies to accomplish many innovative measurements, deployed these techniques for applications in weather modeling and trace gas flux measurements/dispersion modeling, and disseminated the findings in the literature. Moving forward, the sUAS techniques presented herein will be used to solve new technical and scientific challenges. By continuing the research presented, measurement uncertainties of trace gas sources/sinks will be constrained, and the consequences of fugitive trace gases can be concisely identified through atmospheric chemistry. Ultimately, the research can inspire legislation that will adequately regulate

industrial activities and mitigate changes to atmospheric composition that drive anthropogenic climate change.

APPENDIX

Biomass Burning Particulate Collection with Unmanned Aerial Vehicle

A SOLO (3DR Robotics, Berkeley CA, USA) unmanned aerial vehicle (UAV) was designed to autonomously and systematically sample a biomass burning plume. The sUAS had a flight time of ~10 min and could operate semi-continuously with 1-minute battery changes. The SOLO was equipped with an external 4S LIPO battery (ZOP Power, Shenzhen, Guangdong, China) with a 12V battery eliminator circuit (D24V22F12, Pololu, Las Vegas, NV, USA) powering a vacuum pump (SP625 EC-LC-DU-VD, 12VDC, Schwarzer Precision, Huntersville, NC, USA) at a constant flow rate of 12.0 L/min. To collect the particles, a pre-massed glass fiber filter (A/E glass fiber 47mm, Pall Corporation, Port Washington, NY, USA) was fixed in a stainless-steel filter holder (model 1220, Pall Corporation) and attached to the vacuum pump via a 50.0 cm Teflon tube slid through a rigid carbon fiber rod to extend the filter beyond the point of rotor disturbance (Figure A1).[158, 159]

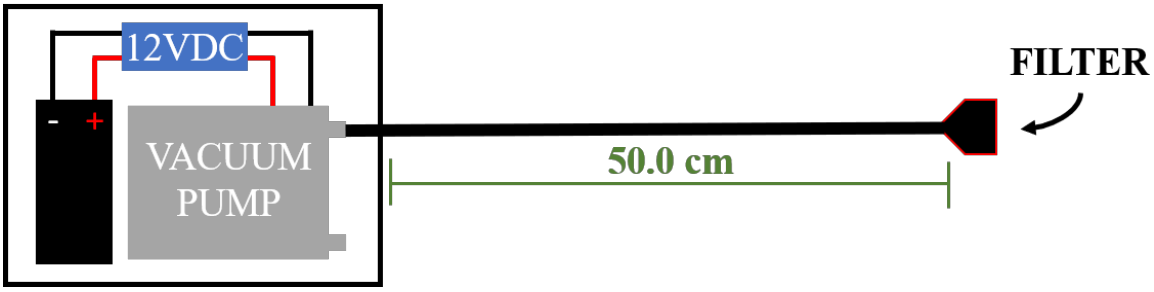

Figure A1 Schematic of particulate collection device integrated into SOLO UAV.

The biomass burning particles were collected on March 5th, 2020 during a controlled burn at the Shaker Village of Pleasant Hill located in Harrodsburg, KY. The SOLO was deployed at the safest location nearest to the prescribed burns (37.83462,-84.75665, 232

m above sea level), and hovered ~10 m above ground level next to the controlled burn of a switchgrass (*Panicum Virgatum*) pasture (blue star, Figure A2b).

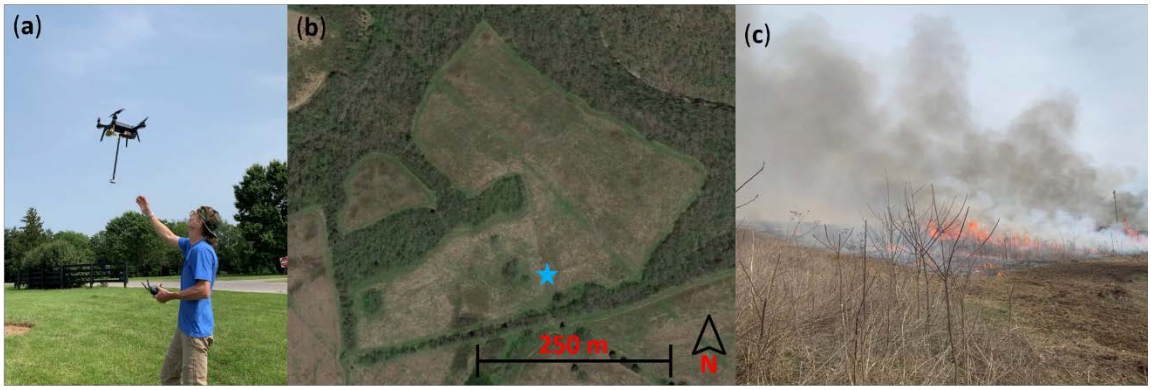

Figure A2 (a) Image of the biomass particulate collection sUAS deployed at Shaker Village. (b) Google Earth image of the sawgrass field with blue start depicting the home location of the sUAS during the prescribed burn. (c) An image of the prescribed burn from the home location.

The SOLO hovered in the plume for ~30 minutes per filter, sampling approximately 360 L of air. The filters were collected in triplicate and immediately stored in a dark cooler temperature controlled with an ice pack (Caldera International Inc., Canby, OR, USA). The filters were weighed before and after sample collection by triplicate in an analytical balance (MS204S-03 Mettler Toledo, Columbus, OH, USA) to ensure a constant mass to a decimal of a mg and refrigerated in darkness until extraction for wet-lab analysis. The net mass of the material collected in each filter was 12.4 mg, 9.5 mg, and 11.2 mg.

REFERENCES

1. Seinfeld, J. H.; Pandis, S. N., *Atmospheric chemistry and physics: from air pollution to climate change*. 3rd ed.; Wiley: Hoboken, New Jersey, 2016; p 1152.
2. Fowler, D.; Pilegaard, K.; Sutton, M.; Ambus, P.; Raivonen, M.; Duyzer, J.; Simpson, D.; Fagerli, H.; Fuzzi, S.; Schjørring, J. K., Atmospheric composition change: ecosystems–atmosphere interactions. *Atmos. Environ.* **2009,** *43*, (33), 5193-5267.
3. Xi, X.; Johnson, M. S.; Jeong, S.; Fladeland, M.; Pieri, D.; Diaz, J. A.; Bland, G. L., Constraining the sulfur dioxide degassing flux from Turrialba volcano, Costa Rica using unmanned aerial system measurements. *J. Volcano. Geoth. Res.* **2016,** *325*, 110-118.
4. Robock, A., Volcanic eruptions and climate. *Rev. Geophys.* **2000,** *38*, (2), 191-219.
5. Rowland, F.; Molina, M. J., Chlorofluoromethanes in the environment. *Rev. Geophys.* **1975,** *13*, (1), 1-35.
6. NASA Ozone Hole Watch. https://ozonewatch.gsfc.nasa.gov/ (12 January 2017),
7. Illingworth, S.; Allen, G.; Percival, C.; Hollingsworth, P.; Gallagher, M.; Ricketts, H.; Hayes, H.; Ładosz, P.; Crawley, D.; Roberts, G., Measurement of boundary layer ozone concentrations on-board a Skywalker unmanned aerial vehicle. *Atmos. Sci. Lett.* **2014,** *15*, (4), 252-258.
8. World Health Organization Preventing Disease Through Healthy Environments. http://www.who.int/ipcs/features/air_pollution.pdf (4 July 2017),
9. World Health Organization Ambient (outdoor) air quality and health. http://www.who.int/mediacentre/factsheets/fs313/en/ (4 July 2017),
10. Chahine, M. T.; Pagano, T. S.; Aumann, H. H.; Atlas, R.; Barnet, C.; Blaisdell, J.; Chen, L.; Divakarla, M.; Fetzer, E. J.; Goldberg, M., AIRS: Improving weather forecasting and providing new data on greenhouse gases. *Bull. Am. Meteorol. Soc.* **2006,** *87*, (7), 911-926.
11. Clow, J.; Smith, J. C. Using Unmanned Air Systems to Monitor Methane in the Atmosphere. https://ntrs.nasa.gov/search.jsp?R=20160003620 (12 January 2017),
12. Wainner, R. T.; Frish, M. B.; Green, B. D.; Laderer, M. C.; Allen, M. G.; Morency, J. R. High Altitude Aerial Natural Gas Leak Detection System. https://www.osti.gov/scitech/biblio/921001 (14 January 2017),
13. Heard, D., *Analytical techniques for atmospheric measurement*. Blackwell Publishing Ltd: Oxford, U.K., 2006; p 528.
14. Crosson, E., A cavity ring-down analyzer for measuring atmospheric levels of methane, carbon dioxide, and water vapor. *Appl. Phys. B-Lasers O.* **2008,** *92*, (3), 403-408.
15. Brady, J. M.; Stokes, M. D.; Bonnardel, J.; Bertram, T. H., Characterization of a Quadrotor Unmanned Aircraft System for Aerosol-Particle-Concentration Measurements. *Environ. Sci. Technol.* **2016,** *50*, (3), 1376-1383.
16. Renard, J.-B.; Dulac, F.; Berthet, G.; Lurton, T.; Vignelles, D.; Jégou, F.; Tonnelier, T.; Jeannot, M.; Couté, B.; Akiki, R., LOAC: a small aerosol optical counter/sizer for ground-based and balloon measurements of the size distribution and nature of atmospheric particles–Part 1: Principle of measurements and instrument evaluation. *Atmos. Meas. Tech.* **2016,** *9*, (4), 1721-1742.
17. Renard, J.-B.; Dulac, F.; Berthet, G.; Lurton, T.; Vignelle, D.; Jégou, F.; Tonnelier, T.; Thaury, C.; Jeannot, M.; Couté, B., LOAC: a small aerosol optical counter/sizer for ground-based and balloon measurements of the size distribution and nature of atmospheric

particles–Part 2: First results from balloon and unmanned aerial vehicle flights. *Atmos. Meas. Tech. Discuss.* **2015,** *8*, (1), 1261-1299.
18. Leoni, C.; Hovorka, J.; Dočekalová, V.; Cajthaml, T. s.; Marvanová, S. a., Source Impact Determination using Airborne and Ground Measurements of Industrial Plumes. *Environ. Sci. Technol.* **2016,** *50*, (18), 9881-9888.
19. Axisa, D.; DeFelice, T. P., Modern and prospective technologies for weather modification activities: A look at integrating unmanned aircraft systems. *Atmos. Res.* **2016,** *178*, 114-124.
20. Rango, A.; Laliberte, A.; Herrick, J. E.; Winters, C.; Havstad, K.; Steele, C.; Browning, D., Unmanned aerial vehicle-based remote sensing for rangeland assessment, monitoring, and management. *J. Appl. Remote Sens.* **2009,** *3*, (1), 33515-33542.
21. National Purchase Diary Year-Over-Year Drone Revenue Soars, According to NPD. https://www.npd.com/wps/portal/npd/us/news/press-releases/2016/year-over-year-drone-revenue-soars-according-to-npd/ (20 January 2017),
22. Bretschneider, T. R.; Shetti, K. In *UAV-based gas pipeline leak detection*, Proc. Asian Conf. Remote Sens., Nay Pyi Taw, Myanmar, October, 2014; Nay Pyi Taw, Myanmar, 2014.
23. Federal Aviation Administration Operation and Certification of Small Unmanned Aerial Vehicles. https://www.federalregister.gov/documents/2016/06/28/2016-15079/operation-and-certification-of-small-unmanned-aircraft-systems (2 June 2017),
24. Villa, T. F.; Gonzalez, F.; Miljievic, B.; Ristovski, Z. D.; Morawska, L., An Overview of Small Unmanned Aerial Vehicles for Air Quality Measurements: Present Applications and Future Prospectives. *Sensors* **2016,** *16*, (7), 1072-1101.
25. Watts, A. C.; Ambrosia, V. G.; Hinkley, E. A., Unmanned aircraft systems in remote sensing and scientific research: Classification and considerations of use. *Remote Sens.* **2012,** *4*, (6), 1671-1692.
26. Rossi, M.; Brunelli, D.; Adami, A.; Lorenzelli, L.; Menna, F.; Remondino, F. In *Gas-Drone: Portable gas sensing system on UAVs for gas leakage localization*, IEEE SENSORS 2014 Proceedings, Valencia, Spain, 2-5 November, 2014; IEEE: Valencia, Spain, 2014; pp 1431-1434.
27. UAS Task Force Unmanned Aircraft System Airspace Integration Plan. http://www.acq.osd.mil/sts/docs/DoD_UAS_Airspace_Integ_Plan_v2_(signed).pdf (13 June 2017),
28. Environmental Protection Agency Air Sensor Guidebook. https://cfpub.epa.gov/si/si_public_file_download.cfm?p_download_id=519616 (20 September 2017),
29. Thibault, S. E.; Holman, D.; Trapani, G.; Garcia, S. In *CFD Simulation of a Quad-Rotor UAV with Rotors in Motion Explicitly Modeled Using an LBM Approach with Adaptive Refinement*, 55th AIAA Aerospace Sciences Meeting, 2017; 2017; p 0583.
30. Yoon, S.; Lee, H. C.; Pulliam, T. H., Computational Analysis of Multi-Rotor Flows. **2016**.
31. Poyi, G. T.; Wu, M. H.; Bousbaine, A., Computational fluid dynamics model of a quad-rotor helicopter for dynamic analysis. *IJREAT International Journal of Research in Engineering & Advanced Technology* **2016**.

32. Roldán, J.; Joossen, G.; Sanz, D.; del Cerro, J.; Barrientos, A., Mini-UAV Based Sensory System for Measuring Environmental Variables in Greenhouses. *Sensors* **2015,** *15*, (2), 3334.
33. Rajeshwar, K.; Ibanez, J. G., *Enivronmental Electrochemistry: Fundamentals and Applications in Pollution Abatement*. Academic Press, INC.: San Diego, CA, USA, 1997; p 776.
34. Cross, E. S.; Lewis, D. K.; Williams, L. R.; Magoon, G. R.; Kaminsky, M. L.; Worsnop, D. R.; Jayne, J. T., Use of electrochemical sensors for measurement of air pollution: correcting interference response and validating measurements. *Atmos. Meas. Tech. Discuss.* **2017,** *2017*, 1-17.
35. Spinelle, L.; Gerboles, M.; Kok, G.; Persijn, S.; Sauerwald, T., Review of Portable and Low-Cost Sensors for the Ambient Air Monitoring of Benzene and Other Volatile Organic Compounds. *Sensors* **2017,** *17*, (7), 1520-1550.
36. Werle, P.; Slemr, F.; Maurer, K.; Kormann, R.; Mücke, R.; Jänker, B., Near-and mid-infrared laser-optical sensors for gas analysis. In *Proceedings of SPIE - Diode Lasers and Applications in Atmospheric Sensing*, Seattle, WA, USA, 2002; Vol. 37, pp 101-114.
37. Fanchenko, S.; Baranov, A.; Savkin, A.; Sleptsov, V. In *LED-based NDIR natural gas analyzer*, IOP Conference Series: Materials Science and Engineering, Mykonos, Greece, 27-30 September, 2015; IOP Publishing: Mykonos, Greece, 2015.
38. Moseley, P. T., Progress in the development of semiconducting metal oxide gas sensors: a review. *Meas. Sci. Tech.* **2017,** *28*, (8), 82001-82016.
39. Karpov, E. E.; Karpov, E. F.; Suchkov, A.; Mironov, S.; Baranov, A.; Sleptsov, V.; Calliari, L., Energy efficient planar catalytic sensor for methane measurement. *Sens. Actuators A Phys.* **2013,** *194*, 176-180.
40. Khan, A.; Schaefer, D.; Tao, L.; Miller, D. J.; Sun, K.; Zondlo, M. A.; Harrison, W. A.; Roscoe, B.; Lary, D. J., Low power greenhouse gas sensors for unmanned aerial vehicles. *Remote Sens.* **2012,** *4*, (5), 1355-1368.
41. So, S.; Sani, A. A.; Zhong, L.; Tittel, F.; Wysocki, G. In *Laser spectroscopic trace-gas sensor networks for atmospheric monitoring applications*, ESSA Workshop, San Francisco, CA, USA, 16 April, 2009; ESSA: San Francisco, CA, USA, 2009.
42. Chen, M.-C.; Chen, C.-H.; Huang, M.-S.; Ciou, J.-Y.; Zhang, G.-T., Design of unmanned vehicle system for disaster detection. *INT J DISTRIB SENS N* **2015**, 784298-784306.
43. Hanwei Electronics Specification Document for MQ-4 Gas Sensor. https://www.sparkfun.com/datasheets/Sensors/Biometric/MQ-4.pdf (12 December 2016),
44. Allen, G.; Gallagher, M.; Hollingsworth, P.; Illingworth, S.; Kabbabe, K.; Percival, C. Feasibility of aerial measurements of methane emissions from landfills. https://www.gov.uk/government/publications/aerial-measurements-of-methane-emissions-from-landfills (12 January 2017),
45. Bartholmai, M.; Neumann, P., Micro-Drone for Gas Measurement in Hazardous Scenarios. In *Selected Topics in Power Systems and Remote Sensing*, WSEAS Press: Tazikawa, Japan, 2010; pp 149-152.
46. Alvear, O.; Zema, N. R.; Natalizio, E.; Calafate, C. T., Using UAV-Based Systems to Monitor Air Pollution in Areas with Poor Accessibility. *Journal of Advanced Transportation* **2017,** *2017*, 14.

47. Berman, E. S. F.; Fladeland, M.; Liem, J.; Kolyer, R.; Gupta, M., Greenhouse gas analyzer for measurements of carbon dioxide, methane, and water vapor aboard an unmanned aerial vehicle. *Sensors and Actuators B: Chemical* **2012,** *169*, (Supplement C), 128-135.
48. Davenport, M. E., S., How drones help us study our climate, forecast weather. *C&EN* 2016.
49. Davenport, M. E., S., Rise of the machines. *C&EN* 2016.
50. Everts, S., Drones detect threats such as chemical weapons, volcanic eruptions. *C&EN* 2016.
51. Malaver, A.; Motta, N.; Corke, P.; Gonzalez, F., Development and Integration of a Solar Powered Unmanned Aerial Vehicle and a Wireless Sensor Network to Monitor Greenhouse Gases. *Sensors* **2015,** *15*, (2), 4072.
52. Nathan, B. J.; Golston, L. M.; O'Brien, A. S.; Ross, K.; Harrison, W. A.; Tao, L.; Lary, D. J.; Johnson, D. R.; Covington, A. N.; Clark, N. N.; Zondlo, M. A., Near-Field Characterization of Methane Emission Variability from a Compressor Station Using a Model Aircraft. *Environmental Science & Technology* **2015,** *49*, (13), 7896-7903.
53. Selker, J.; Tyler, S.; Higgins, C.; Wing, M., *Drone Squadron to Take Earth Monitoring to New Heights*. 2015; Vol. 96.
54. Hurley, B. Report from SPIE 2017: Drones Spot Gas Leaks from the Sky. http://www.techbriefs.com/component/content/article/1198-ntb/news/news/26735-from-spie-laserbased-sensors-uavs-spot-methane-leaks (4 October 2017),
55. Knörig, A.; Wettach, R.; Cohen, J. In *Fritzing: a tool for advancing electronic prototyping for designers*, Proceedings of the 3rd International Conference on Tangible and Embedded Interaction, 2009; ACM: 2009; pp 351-358.
56. Federal Aviation Administration Operation and Certification of Small Unmanned Aircraft Systems. https://www.faa.gov/uas/media/RIN_2120-AJ60_Clean_Signed.pdf (12 September 2017),
57. Federal Aviation Administration List of Commerical Testing Centers in Compliance with Part 107. https://www.faa.gov/training_testing/testing/media/test_centers.pdf (12 September 2017),
58. Federal Aviation Administration sUAS Registration with FAA. https://registermyuas.faa.gov/ (12 September 2017),
59. European Aviation Safety Agency Introduction of a regulatory framework for the operation of drones (A). https://www.easa.europa.eu/system/files/dfu/NPA%202017-05%20%28A%29_0.pdf (14 September 2017),
60. European Aviation Safety Agency Introduction of a regulatory framework for the operation of drones (B). https://www.easa.europa.eu/system/files/dfu/NPA%202017-05%20%28B%29.pdf (14 September 2017),
61. International Civil Aviation Organization Current State Regulations of Unmanned Aircraft. https://www4.icao.int/uastoolkit/Home/BestPractices (14 September 2017),
62. International Civil Aviation Organization Civil Aviation Authorites Worldwide. https://www.icao.int/Pages/Links.aspx (14 September 2017),
63. Gimeno, L., Grand challenges in atmospheric science. *Front Earth Sci* **2013,** *1*, 1-5.

64. Watson, A. Y.; Bates, R. R.; Kennedy, D., *Mathematical Modeling of the Effect of Emission Sources on Atmospheric Pollutant Concentrations*. National Academy of Science: Washington, D.C., 1988; Vol. 1, p 704.
65. Witte, B. M.; Singler, R. F.; Bailey, S. C., Development of an unmanned aerial vehicle for the measurement of turbulence in the atmospheric boundary layer. *Atmosphere* **2017,** *8*, (10), 195.
66. Rigby, M.; Prinn, R. G.; O'Doherty, S.; Miller, B. R.; Ivy, D.; Mühle, J.; Harth, C. M.; Salameh, P. K.; Arnold, T.; Weiss, R. F.; Krummel, P. B.; Steele, L. P.; Fraser, P. J.; Young, D.; Simmonds, P. G., Recent and future trends in synthetic greenhouse gas radiative forcing. *Geophys Res Lett* **2014,** *41*, (7), 2623-2630.
67. Köhler, P.; Nehrbass-Ahles, C.; Schmitt, J.; Stocker, T. F.; Fischer, H., A 156 kyr smoothed history of the atmospheric greenhouse gases CO_2, CH_4, and N_2O and their radiative forcing. *Earth Syst. Sci. Data* **2017,** *9*, (1), 363-387.
68. Pachauri, R. K.; Allen, M. R.; Barros, V. R.; Broome, J.; Cramer, W.; Christ, R.; Church, J. A.; Clarke, L.; Dahe, Q.; Dasgupta, P.; Dubash, N. K.; Edenhofer, O.; Elgizouli, I.; Field, C. B.; Forster, P.; Friedlingstein, P.; Fuglestvedt, J.; Gomez-Echeverri, L.; Hallegatte, S.; Hegerl, G.; Howden, M.; Jiang, K.; Jimenez Cisneroz, B.; Kattsov, V.; Lee, H.; Mach, K. J.; Marotzke, J.; Mastrandrea, M. D.; Meyer, L.; Minx, J.; Mulugetta, Y.; O'Brien, K.; Oppenheimer, M.; Pereira, J. J.; Pichs-Madruga, R.; Plattner, G. K.; Pörtner, H. O.; Power, S. B.; Preston, B.; Ravindranath, N. H.; Reisinger, A.; Riahi, K.; Rusticucci, M.; Scholes, R.; Seyboth, K.; Sokona, Y.; Stavins, R.; Stocker, T. F.; Tschakert, P.; van Vuuren, D.; van Ypserle, J. P. *Climate Change 2014: Synthesis Report. Contribution of Working Groups I, II and III to the Fifth Assessment Report of the Intergovernmental Panel on Climate Change*; IPCC: Geneva, 2014; p 151.
69. Snyder, C. W., Evolution of global temperature over the past two million years. *Nature* **2016,** *538*, 226-228.
70. Liu, P.; Wang, X.; Fan, J.; Xiao, W.; Wang, Y., Effects of air pollution on hospital emergency room visits for respiratory diseases: Urban-suburban differences in Eastern China. *Int. J. Environ. Res. Public Health* **2016,** *13*, (3), 341.
71. Dominici, F.; Peng, R. D.; Barr, C. D.; Bell, M. L., Protecting human health from air pollution: Shifting from a single-pollutant to a multi-pollutant approach. *Epidemiology* **2010,** *21*, (2), 187-194.
72. Nhung, N. T. T.; Schindler, C.; Dien, T. M.; Probst-Hensch, N.; Perez, L.; Künzli, N., Acute effects of ambient air pollution on lower respiratory infections in Hanoi children: An eight-year time series study. *Environ. Int.* **2018,** *110*, (Supplement C), 139-148.
73. Fischer, M., Airborne methane emission measurements for selected oil and gas facilities across California. *Environ. Sci. Technol.* **2017,** *51*, (21), 12981-12987
74. Lavoie, T. N.; Shepson, P. B.; Gore, C. A.; Stirm, B. H.; Kaeser, R.; Wulle, B.; Lyon, D.; Rudek, J., Correction to assessing the methane emissions from natural gas-fired power plants and oil refineries. *Environ. Sci. Technol.* **2017,** *51*, (10), 5856-5857.
75. Lee, S.; Choi, Y.; Woo, J.; Kang, W.; Jung, J., Estimating and comparing greenhouse gas emissions with their uncertainties using different methods: A case study for an energy supply utility. *J. Air Waste Manage.* **2014,** *64*, (10), 1164-1173.
76. Schuyler, T.; Guzman, M., Unmanned Aerial Systems for Monitoring Trace Tropospheric Gases. *Atmosphere* **2017,** *8*, (10), 206.

77. CLOUDMAP Collaboration Leading Operational Unmanned Aerial System Development for Meteorology and Atmospheric Physics. http://www.cloud-map.org/ (March 1, 2018),
78. Google Maps Stillwater, OK. (30 August 2017),
79. Mesonet Stillwater, OK Mesonet Daily Averages. http://www.mesonet.org/index.php/weather/daily_data_retrieval (30 August 2017),
80. Zhou, R.; Guzman, M. I., Photocatalytic reduction of fumarate to succinate on ZnS mineral surfaces. *J. Phys. Chem. C* **2016,** *120*, (13), 7349-7357.
81. Eugene, A. J.; Guzman, M. I., Reactivity of ketyl and acetyl radicals from direct solar actinic photolysis of aqueous pyruvic acid. *J. Phys. Chem. A* **2017,** *121*, (15), 2924-2935.
82. Hemingway, B.; Frazier, A.; Elbing, B.; Jacob, J., Vertical sampling scales for atmospheric boundary layer measurements from small unmanned aircraft systems (sUAS). *Atmosphere* **2017,** *8*, (9), 176.
83. Barchyn, T. E.; Hugenholtz, C. H.; Myshak, S.; Bauer, J., A UAV-based system for detecting natural gas leaks. *J. Unmanned Veh. Syst.* **2018,** *6*, (1), 18-30.
84. National Atmospheric Deposition Program, Ammonia Monitoring Network. In 2016.
85. Dlugokencky, E. J., P.M. Lang, A.M. Crotwell, J.W. Mund, M.J. Crotwell, and K.W. Thoning, Atmospheric Methane Dry Air Mole Fractions from the NOAA ESRL Carbon Cycle Cooperative Global Air Sampling Network, 1983-2016. In 2017.
86. Tans, P., Keeling, R., Earth System Research Laboratory - Trends in Atmospheric Carbon Dioxide at Mauna Loa. In 2016.
87. Barbieri, L.; Kral, S. T.; Bailey, S. C. C.; Frazier, A. E.; Jacob, J. D.; Reuder, J.; Brus, D.; Chilson, P. B.; Crick, C.; Detweiler, C.; Doddi, A.; Elston, J.; Foroutan, H.; Gonzalez-Rocha, J.; Greene, B. R.; Guzman, M. I.; Houston, A. L.; Islam, A.; Kemppinen, O.; Lawrence, D.; Pillar-Little, E. A.; Ross, S. D.; Sama, M. P.; Schmale, D. G.; Schuyler, T. J.; Shankar, A.; Smith, S. W.; Waugh, S.; Dixon, C.; Borenstein, S.; de Boer, G., Intercomparison of small unmanned aircraft system (sUAS) measurements for atmospheric science during the LAPSE-RATE campaign. *Sensors* **2019,** *19*, (9), 2179.
88. Schuyler, T. J.; Guzman, M. I., Unmanned aerial systems for monitoring trace tropospheric gases. *Atmosphere* **2017,** *8*, (10), 206.
89. Schuyler, T. J.; Bailey, S. C.; Guzman, M. I., Monitoring Tropospheric Gases with Small Unmanned Aerial Systems (sUAS) during the Second CLOUDMAP Flight Campaign. *Atmosphere* **2019,** *10*, (8), 434.
90. Schuyler, T. J.; Gohari, S.; Pundsack, G.; Berchoff, D.; Guzman, M. I., Using a Balloon-Launched Unmanned Glider to Validate Real-Time WRF Modeling. *Sensors* **2019,** *19*, (8), 1914.
91. Environmental Protection Agency *Inventory of U.S. Greenhouse Gas Sinks*; 2019; pp 71-86.
92. Environmental Protection Agency *Climate Change Indicators In The United States (Fourth Edition)*; 2016; pp 12-20.
93. Environmental Protection Agency *Energy Efficienty as a Low-Cost Resource for Achieving Carbon Emissions Reductions*; 2009.

94. Davies, K.; Malik, A.; Li, J.; Aung, T. N., A meta-study on the feasibility of the implementation of new clean coal technologies to existing coal-fired power plants in an effort to decrease carbon emissions. *Energ. Sci. Technol.* **2017,** *4*, 30-45.
95. Zhao, M.; Minett, A. I.; Harris, A. T., A review of techno-economic models for the retrofitting of conventional pulverised-coal power plants for post-combustion capture (PCC) of CO_2. *Energ. Environ. Sci.* **2013,** *6*, (1), 25-40.
96. Chung, T. S.; Patiño-Echeverri, D.; Johnson, T. L., Expert assessments of retrofitting coal-fired power plants with carbon dioxide capture technologies. *Energ. Policy* **2011,** *39*, (9), 5609-5620.
97. Mondal, M. K.; Balsora, H. K.; Varshney, P., Progress and trends in CO_2 capture/separation technologies: a review. *Energy* **2012,** *46*, (1), 431-441.
98. Wang, M.; Lawal, A.; Stephenson, P.; Sidders, J.; Ramshaw, C., Post-combustion CO_2 capture with chemical absorption: A state-of-the-art review. *Chem. Eng. Res. Des.* **2011,** *89*, (9), 1609-1624.
99. Singh, B.; Strømman, A. H.; Hertwich, E., Life cycle assessment of natural gas combined cycle power plant with post-combustion carbon capture, transport and storage. *Int. J. of Greenh. Gas Cont.* **2011,** *5*, (3), 457-466.
100. Conway, W.; Wang, X.; Fernandes, D.; Burns, R.; Lawrance, G.; Puxty, G.; Maeder, M., Comprehensive kinetic and thermodynamic study of the reactions of CO_2 (aq) and HCO_3^- with monoethanolamine (MEA) in aqueous solution. *J. Phys. Chem. A* **2011,** *115*, (50), 14340-14349.
101. Lv, B.; Guo, B.; Zhou, Z.; Jing, G., Mechanisms of CO_2 capture into monoethanolamine solution with different CO_2 loading during the absorption/desorption processes. *Environ. Sci. Technol.* **2015,** *49*, (17), 10728-10735.
102. Puxty, G.; Rowland, R.; Attalla, M., Comparison of the rate of CO_2 absorption into aqueous ammonia and monoethanolamine. *Chem. Eng. Sci.* **2010,** *65*, (2), 915-922.
103. Qin, F.; Wang, S.; Hartono, A.; Svendsen, H. F.; Chen, C., Kinetics of CO_2 absorption in aqueous ammonia solution. *Int. J. Greenh. Gas Con.* **2010,** *4*, (5), 729-738.
104. Rao, A. B.; Rubin, E. S., A technical, economic, and environmental assessment of amine-based CO_2 capture technology for power plant greenhouse gas control. *Environ. Sci. Technol.* **2002,** *36*, (20), 4467-4475.
105. U.S. Energy Information Administration *Electric Power Annual 2017*; 2019.
106. Scott, V.; Gilfillan, S.; Markusson, N.; Chalmers, H.; Haszeldine, R. S., Last chance for carbon capture and storage. *Nat. Clim. Change* **2013,** *3*, (2), 105.
107. Thompson, J. G.; Bhatnagar, S.; Combs, M.; Abad, K.; Onneweer, F.; Pelgen, J.; Link, D.; Figueroa, J.; Nikolic, H.; Liu, K., Pilot testing of a heat integrated 0.7 MWe CO_2 capture system with two-stage air-stripping: Amine degradation and metal accumulation. *Int. J. Greenh. Gas Con.* **2017,** *64*, 23-33.
108. Chi, S.; Rochelle, G. T., Oxidative degradation of monoethanolamine. *Ind. Eng. Chem. Res.* **2002,** *41*, (17), 4178-4186.
109. da Silva, E. F.; Lepaumier, H. l. n.; Grimstvedt, A.; Vevelstad, S. J.; Einbu, A.; Vernstad, K.; Svendsen, H. F.; Zahlsen, K., Understanding 2-ethanolamine degradation in postcombustion CO_2 capture. *Ind. Eng. Chem. Res.* **2012,** *51*, (41), 13329-13338.
110. Goff, G. S.; Rochelle, G. T., Monoethanolamine degradation: O_2 mass transfer effects under CO_2 capture conditions. *Ind. Eng. Chem. Res.* **2004,** *43*, (20), 6400-6408.

111. Ma, S.; Song, H.; Wang, M.; Yang, J.; Zang, B., Research on mechanism of ammonia escaping and control in the process of CO_2 capture using ammonia solution. *Chem. Eng. Res. Des.* **2013,** *91*, (7), 1327-1334.
112. Kirkby, J.; Curtius, J.; Almeida, J.; Dunne, E.; Duplissy, J.; Ehrhart, S.; Franchin, A.; Gagné, S.; Ickes, L.; Kürten, A., Role of sulphuric acid, ammonia and galactic cosmic rays in atmospheric aerosol nucleation. *Nature* **2011,** *476*, (7361), 429.
113. Luo, C.; Zender, C. S.; Bian, H.; Metzger, S., Role of ammonia chemistry and coarse mode aerosols in global climatological inorganic aerosol distributions. *Atmos. Environ.* **2007,** *41*, (12), 2510-2533.
114. Paulot, F.; Ginoux, P.; Cooke, W.; Donner, L.; Fan, S.; Lin, M.-Y.; Mao, J.; Naik, V.; Horowitz, L., Sensitivity of nitrate aerosols to ammonia emissions and to nitrate chemistry: implications for present and future nitrate optical depth. *Atmos. Chem. Phys.* **2016,** *16*, (3), 1459-1477.
115. Thompson, J. G.; Combs, M.; Abad, K.; Bhatnagar, S.; Pelgen, J.; Beaudry, M.; Rochelle, G.; Hume, S.; Link, D.; Figueroa, J., Pilot testing of a heat integrated 0.7 MWe CO_2 capture system with two-stage air-stripping: Emission. *Int. J. Greenh. Gas Con.* **2017,** *64*, 267-275.
116. Jacob, D. J., *Introduction to Atmospheric Chemistry*. Princeton University Press: Princeton, NJ, 1999.
117. Ghosh, D.; Vogt, A. In *Outliers: An Evaluation of Methodologies*, Joint Statistical Meetings, San Diego, CA, 2012; San Diego, CA, 2012; pp 3455-3460.
118. Weather Underground Inc Horse Country Weather Station (KKyLEXIN183). https://www.wunderground.com/dashboard/pws/KKYGEORG28/graph/2018-09-16/2018-09-16/weekly (September 20, 2018),
119. Paulot, F.; Jacob, D. J.; Pinder, R. W.; Bash, J. O.; Travis, K.; Henze, D. K., Ammonia emissions in the United States, European Union, and China derived by high-resolution inversion of ammonium wet deposition data: Interpretation with a new agricultural emissions inventory (MASAGE_NH_3). *J. Geophys. Res-Atmos.* **2014,** *119*, (7), 4343-4364.
120. Brusca, S.; Famoso, F.; Lanzafame, R.; Mauro, S.; Garrano, A. M. C.; Monforte, P., Theoretical and Experimental Study of Gaussian Plume Model in Small Scale System. *Energy Procedia* **2016,** *101*, 58-65.
121. De Nevers, N., *Air Pollution Control Engineering*. Second ed.; Waveland Press Inc.: Long Grove, IL, 2010.
122. Stockie, J. M., The Mathematics of Atmospheric Dispersion Modeling. *Siam Rev.* **2011,** *53*, (2), 349-372.
123. Turner, B. D., *Workbook of Atmospheric Dispersion Estimates: an Introduction to Dispersion Modeling*. CRC press: Boca Raton, FL, 1994.
124. Marjovi, A.; Marques, L. In *Multi-Robot Odor Distribution Mapping in Realistic Time-Variant Conditions*, 2014 IEEE International Conference on Robotics and Automation, 2014; IEEE: 2014; pp 3720-3727.
125. Murlis, J.; Elkinton, J. S.; Carde, R. T., Odor Plumes and How Insects Use Them. *Rev. Entomol.* **1992,** *37*, (1), 505-532.
126. Sánchez-Sosa, J. E.; Castillo-Mixcóatl, J.; Beltrán-Pérez, G.; Muñoz-Aguirre, S., An Application of the Gaussian Plume Model to Localization of an Indoor Gas Source with a Mobile Robot. *Sensors* **2018,** *18*, (12), 4375.

127. Alvarez, R. A.; Zavala-Araiza, D.; Lyon, D. R.; Allen, D. T.; Barkley, Z. R.; Brandt, A. R.; Davis, K. J.; Herndon, S. C.; Jacob, D. J.; Karion, A., Assessment of Methane Emissions from the US Oil and Gas Supply Chain. *Science* **2018,** *361*, (6398), 186-188.
128. Stocker, T. F.; D. Qin; G.-K. Plattner; M. Tignor; S.K. Allen; J. Boschung; A. Nauels; Y. Xia; V. Bex *IPCC Chapter 8: Anthropogenic and Natural Radiative Forcing*; 2013.
129. Bousquet, P.; Ciais, P.; Miller, J. B.; Dlugokencky, E. J.; Hauglustaine, D. A.; Prigent, C.; Van der Werf, G. R.; Peylin, P.; Brunke, E. G.; Carouge, C., Contribution of Anthropogenic and Natural Sources to Atmospheric Methane Variability. *Nature* **2006,** *443*, (7110), 439-443.
130. Kirschke, S.; Bousquet, P.; Ciais, P.; Saunois, M.; Canadell, J. G.; Dlugokencky, E. J.; Bergamaschi, P.; Bergmann, D.; Blake, D. R.; Bruhwiler, L., Three Decades of Global Methane Sources and Sinks. *Nat. Geosci.* **2013,** *6*, (10), 813-823.
131. Holmes, C. D., Methane Feedback on Atmospheric Chemistry: Methods, Models, and Mechanisms. *J Adv. Model Earth Sy.* **2018,** *10*, (4), 1087-1099.
132. Reardon, S., Hawaii Volcano Eruption Holds Clues To Predicting Similar Events Elsewhere. *Nature* **2018,** *557*, (7706), 477.
133. Rypdal, K., Global Temperature Response To Radiative Forcing: Solar Cycle Versus Volcanic Eruptions. *J. Geophys. Res-Atmos.* **2012,** *117*, (D6).
134. Baxter, P. J.; Horwell, C. J., Impacts of Eruptions on Human Health. In *The Encyclopedia of Volcanoes*, Elsevier: 2015; pp 1035-1047.
135. Horwell, C. J.; Baxter, P. J., The Respiratory Health Hazards Of Volcanic Ash: A Review For Volcanic Risk Mitigation. *Bull. Volcanol.* **2006,** *69*, (1), 1-24.
136. O'Dwyer, M.; Padgett, M.; McGonigle, A.; Oppenheimer, C.; Inguaggiato, S., Real-Time Measurement of Volcanic H_2S and SO_2 Concentrations by UV Spectroscopy. *Geophysical Research Letters* **2003,** *30*, (12).
137. Hansell, A.; Oppenheimer, C., Health Hazards From Volcanic Gases: A Systematic Literature Review. *Arch. Environ. Occup. Health* **2004,** *59*, (12), 628-639.
138. Rauthe-Schöch, A.; Weigelt, A.; Hermann, M.; Martinsson, B.; Baker, A.; Heue, K.-P.; Brenninkmeijer, C.; Zahn, A.; Scharffe, D.; Eckhardt, S., CARIBIC Aircraft Measurements of Eyjafjallajökull Volcanic Clouds in April/May 2010. *Atmos. Chem. Phys.* **2012,** *12*, 879-902.
139. Alvarez, R. A.; Pacala, S. W.; Winebrake, J. J.; Chameides, W. L.; Hamburg, S. P., Greater Focus Needed on Methane Leakage From Natural Gas Infrastructure. *PNAS* **2012,** *109*, (17), 6435-6440.
140. Witte, B. M.; Singler, R. F.; Bailey, S. C. C., Development of an Unmanned Aerial Vehicle for the Measurement of Turbulence in the Atmospheric Boundary Layer. *Atmosphere* **2017,** *8*, (10), 195.
141. Fuertes, F. C.; Wilhelm, L.; Porté-Agel, F., Multirotor UAV-based platform for the measurement of atmospheric turbulence: Validation and signature detection of tip vortices of wind turbine blades. *J. Atmos. Ocean. Technol.* **2019,** *36*, (6), 941-955.
142. Schuyler, T. J.; Gohari, S. M.; Pundsack, G.; Berchoff, D.; Guzman, M. I., Using a Balloon-Launched Unmanned Glider to Validate Real-Time WRF Modeling. *Sensors* **2019,** *19*, (8), 1914.
143. Nolan, P. J.; Pinto, J.; González-Rocha, J.; Jensen, A.; Vezzi, C. N.; Bailey, S. C. C.; De Boer, G.; Diehl, C.; Laurence, R.; Powers, C. W., Coordinated Unmanned Aircraft

System (UAS) and Ground-Based Weather Measurements to Predict Lagrangian Coherent Structures (LCSs). *Sensors* **2018,** *18*, (12), 4448.
144. Moreira, V. S.; Degrazia, G. A.; Roberti, D. R.; Timm, A. U.; da Costa Carvalho, J., Employing A Lagrangian Stochastic Dispersion Model And Classical Diffusion Experiments To Evaluate Two Turbulence Parameterization Schemes. *Atmos. Pollut. Res.* **2011,** *2*, (3), 384-393.
145. Golston, L. M.; Tao, L.; Brosy, C.; Schäfer, K.; Wolf, B.; McSpiritt, J.; Buchholz, B.; Caulton, D. R.; Pan, D.; Zondlo, M. A., Lightweight Mid-Infrared Methane Sensor for Unmanned Aerial Systems. *Appl. Phys. B* **2017,** *123*, (6), 170.
146. Barchyn, T. E.; Hugenholtz, C. H.; Myshak, S.; Bauer, J., A UAV-based System for Detecting Natural Gas Leaks. *J. Unmanned Veh. Syst.* **2017,** *6*, (1), 18-30.
147. Yang, S.; Talbot, R. W.; Frish, M. B.; Golston, L. M.; Aubut, N. F.; Zondlo, M. A.; Gretencord, C.; McSpiritt, J., Natural Gas Fugitive Leak Detection Using an Unmanned Aerial Vehicle: Measurement System Description and Mass Balance Approach. *Atmosphere* **2018,** *9*, (10), 383.
148. Schuyler, T. J.; Bailey, S. C. C.; Guzman, M. I., Monitoring Tropospheric Gases with Small Unmanned Aerial Systems (sUAS) during the Second CLOUDMAP Flight Campaign. *Atmosphere* **2019,** *10*, (8), 434.
149. Greene, B. R.; Segales, A. R.; Waugh, S.; Duthoit, S.; Chilson, P. B., Considerations for Temperature Sensor Placement on Rotary-Wing Unmanned Aircraft Systems. *Atmos. Meas. Tech.* **2018,** *11*, (10), 5519.
150. Aiuppa, A.; Franco, A.; Von Glasow, R.; Allen, A.; d'Alessandro, W.; Mather, T.; Pyle, D.; Valenza, M., The Tropospheric Processing Of Acidic Gases And Hydrogen Sulphide In Volcanic Gas Plumes As Inferred From Field And Model Investigations. *Atmos. Chem. Phys.* **2007,** *7*, 1441-1450.
151. Tavoularis, S., *Theory of Turbulence*. Cambridge University Press: 2016; Vol. 2, p 171-212.
152. Hanna, S. R., Lagrangian and Eulerian Time-Scale Relations in the Daytime Boundary Layer. *J. Appl. Meteorol.* **1981,** *20*, (3), 242-249.
153. Dosio, A.; Guerau de Arellano, J. V.; Holtslag, A. A.; Builtjes, P. J., Relating Eulerian And Lagrangian Statistics For The Turbulent Dispersion In The Atmospheric Convective Boundary Layer. *J. Atmos. Sci.* **2005,** *62*, (4), 1175-1191.
154. Dosio, A.; Vilà-Guerau de Arellano, J.; Holtslag, A. A.; Builtjes, P. J., Dispersion of a passive tracer in buoyancy-and shear-driven boundary layers. *J. Appl. Meteorol.* **2003,** *42*, (8), 1116-1130.
155. Majda, A. J.; Kramer, P. R., Simplified Models For Turbulent Diffusion: Theory, Numerical Modelling, And Physical Phenomena. *Phys. Rep.* **1999,** *314*, (4-5), 237-574.
156. Moreira, D.; Vilhena, M., *Air Pollution and Turbulence: Modeling and Applications*. CRC Press: 2009.
157. U.S. Environmental Protection Agency Office of Air Quality Planning and Solutions. *Oil and Natural Gas Sector Leaks*; 2014.
158. Russell, C. R.; Jung, J.; Willink, G.; Glasner, B. Wind Tunnel and Hover Performance Test Results for Multicopter UAS Vehicles. https://ntrs.nasa.gov/archive/nasa/casi.ntrs.nasa.gov/20180001325.pdf
159. Kuantama, E.; Craciun, D.; Tarca, R., Quadcopter Body Frame Model and Analysis. *Ann. Univ. Oradea* **2016**, 71-74.

VITA

Travis J. Schuyler

Education

Northern Kentucky University (NKU), Highland Heights, KY 2012 – 2016

Major: Chemistry, ACS and Biochemistry tracks

Minor: Physics

Graduation date: May 2016

Experience

Department of Chemistry, UK

Research Assistant, Dr. Marcelo Guzman's research group January 2017 – May 2020

Teaching Assistant, General Chemistry August – December 2016

Chemistry Tutor August 2016 – May 2020

Department of Chemistry, NKU

Research Assistant, Dr. Isabelle Lagadic's research group May 2013 – May 2016

Teaching Assistant, Analytical Chemistry Lab August – December 2015

Department of Physics, NKU

Research Assistant, Dr. Nathan De Lee's research group September 2015 – May 2016

Physics Tutor, Athletics Department, Northern Kentucky University May – July 2015

Institut Universitaire de Technologie (IUT) Lannion, France

Research Assistant, Dr. Sébastien Gauthier's research group May – July 2014

Publications

1. "Monitoring Tropospheric Gases with Small Unmanned Aerial Systems (sUAS) during the Second CLOUDMAP Flight Campaign" Schuyler, T.J., Bailey, S.C.C., and **Guzman*, M. I.** *Atmosphere* **2019**, *10*(8), 434.
2. "Using a Balloon-Launched Unmanned Glider to Validate Real-Time WRF Modeling". Schuyler, T.J., Gohari, S.M.I., Pundsack, G., Berchoff, D., and **Guzman*, M.I.** *Sensors* **2019**, *19*(8), 1914.

3. "Intercomparison of Small Unmanned Aircraft System (sUAS) Measurements for Atmospheric Science during the LAPSE-RATE Campaign" Lindsey, B., Schuyler, T.J., et al. *Sensors* **2019**, *19*(9), 2179.
4. "Unmanned Aerial Systems for Monitoring Trace Tropospheric Gases". Schuyler, T.J. and **Guzman*, M. I.** *Atmosphere* **2017**, *8(10)*, 206.

Awards and Honors

- **NASA KY Space Grant:** For air quality measurements with small unmanned aerial systems.
- **Provisional Patent:** For the invention of a trace gas quantification device for unmanned vehicles.
- **Outstanding Oral Qualifier Award (UK):** Awarded by the graduate program committee for standout achievements and plan of study during qualifying examination for PhD candidacy.
- **Fast Start Award (UK):** A graduate school award given to one pre-qualifying student for their exceptional research progress, plus the completion of cumulative exams and success in the classroom**.**
- **ISARRA Travel Award:** Awarded on scientific merit for sponsored travel to ISARRA conference and LAPSERATE flight campaign.